ABSTRACT

AN INVESTIGATION OF THE (p,d) REACTION
ON N=Z NUCLEI IN THE 2s-1d SHELL

by

Raymond L. Kozub

An investigation of the (p,d) reaction on N=Z nuclei in the 2s-1d shell has been made to obtain spectroscopic information and to study the ℓ_n=2 J-dependence for the (p,d) reaction. The experiments were performed with ^{24}Mg, ^{28}Si, ^{32}S, ^{36}Ar and ^{40}Ca as target nuclei. An enriched (>99%) ^{24}Mg target was used to study the ^{24}Mg(p,d)^{23}Mg reaction, and a natural SiO foil was used as a ^{28}Si target. Hydrogen sulfide and enriched (>99%) ^{36}Ar gas targets were used for the ^{32}S(p,d)^{31}S and ^{36}Ar(p,d)^{35}Ar experiments, respectively. The ^{40}Ca(p,d)^{39}Ca experiments were performed with evaporated foils of natural calcium. The 33.6 MeV protons were accelerated by the Michigan State University sector-focused cyclotron, and the deuterons were observed with (dE/dx)-E counter telescopes. The overall deuteron energy resolution ranged from 95 keV for the ^{28}Si(p,d)^{27}Si reaction to 130 keV for the ^{36}Ar(p,d)^{35}Ar reaction. Virtually all of the 2s-1d shell hole strength was observed for each target studied.

Raymond L. Kozub

Deuteron angular distributions for strongly excited levels in ^{23}Mg, ^{27}Si, ^{31}S, ^{35}Ar and ^{39}Ca were measured for laboratory angles from 10° to 155°. Excitation energies were also measured. The J-dependence for the pick-up of an $\ell_n=2$ neutron appears mostly in the forward angles of the angular distributions and seems to follow a systematic trend through the 2s-1d shell. Unique spin assignments are suggested for levels in ^{31}S, ^{35}Ar and ^{39}Ca on this basis. There is some evidence for a correlation between the effects of J-dependence and the nature of the nuclear deformation. An attempt is made to reproduce J-dependence effects with calculations in the distorted-wave Born approximation.

Configuration mixing is found to exist in the ground state wave functions of all nuclei, and DWBA spectroscopic factors are extracted for the strongly excited levels. Of particular interest are the $\ell_n=1$ levels excited in the $^{24}Mg(p,d)^{23}Mg$ and $^{28}Si(p,d)^{27}Si$ reactions, which could arise from either 1p or 2p pick-ups. The ground states of ^{36}Ar and ^{40}Ca are observed to contain appreciable mixing with the $f_{7/2}$ shell, and evidence exists for a small $[2p]^2$ admixture in the ^{40}Ca ground state.

The level orders of the residual nuclei and the DWBA spectroscopic factors are compared to the strong

coupling rotational model and to Nilsson model wave functions. Evidence for rotational band mixing is apparent in many cases.

AN INVESTIGATION OF THE (p,d) REACTION ON N=Z NUCLEI IN THE 2s-1d SHELL

by

Raymond L. Kozub

A THESIS

Submitted to
Michigan State University
in partial fulfillment of the requirements
for the degree of

DOCTOR OF PHILOSOPHY

Department of Physics

1967

ACKNOWLEDGMENTS

I wish to express my sincere appreciation to my thesis advisor, Dr. Edwin Kashy, for his guidance and helpful discussions concerning this work. The support and assistance of the entire staff of the Michigan State University Cyclotron Laboratory is gratefully acknowledged. Special thanks go to Mr. Lorenz Kull and Mr. Phillip Plauger for their help in taking the data, and to Dr. William P. Johnson for his assistance in operating the cyclotron.

I acknowledge the financial support of the National Science Foundation for the experimental program. For three years of my graduate work, I was supported by a National Defense Education Act Fellowship.

Very special thanks go to my wife, Sandra, for her encouragement and understanding during the past two years, and for cheerfully typing both the rough and final copies of this thesis.

TABLE OF CONTENTS

LIST OF TABLES

LIST OF FIGURES

Chapter 1

Introduction

Since its original observation by Standing in 1954 (St54)*, the (p,d) reaction has proven to be a valuable tool for the experimental investigation of nuclear properties. This has proven to be particularly true at higher bombarding energies, where the direct reaction theory is most successful (To61). This model of the reaction is characterized by the assumption that the incident proton interacts only with a single neutron in the target nucleus, thereby forming a deuteron and leaving the residual nucleus in some excited state. As was shown by the plane wave stripping theory of Butler (Bu51) for the inverse (d,p) stripping reaction, the shape of the angular distribution of the emitted particles is determined by the orbital angular momentum (ℓ_n) of the transferred neutron. Thus the parity (π) and possible values for the total angular momentum of the final nuclear state (J) can be deduced directly from the experimental data.

The widely used theory of direct reaction processes is the distorted-wave Born approximation (DWBA)

---

* References are denoted by the first two letters of the first author's name and the year of the publication.

(To61, Sa64) and, to the extent that one can trust the DWBA calculations, the (p,d) reaction provides a direct measure of the overlap of the target wave function with the wave functions of the excited states of the residual nucleus. These overlaps represent the coefficients of fractional parentage (c.f.p.) for the ground state wave function, and therefore contain information about the nuclear structure. Configuration admixtures in the target nucleus are thus easily detectable by this reaction. Also, the excitation of levels in the residual nucleus is quite selective, since the coefficients of fractional parentage will be small if the final state is not a hole state.

In 1964, it was observed by Lee and Schiffer (Le64) that the angular distributions for ℓ_n=1 levels excited in the (d,p) reaction showed a dependence on the total angular momentum of the final nuclear state (J), even though the ℓ_n values were the same. Similar effects have also been observed in the (p,d) reaction (Sh64, Gl65 (a), Wh66, Ko67). At present, there still is not a satisfactory theoretical explanation for J-dependence in the (p,d) reaction.

Most of the previous investigations with the (p,d) reaction have been with nuclei in the 1p and $1f_{7/2}$ shells. However, relatively few (p,d) experiments have been performed on the N=Z targets in the 2s-1d shell. This probably reflects the very negative reaction Q-values

(-13 to -15 MeV) and the close level spacing involved, which require both a high bombarding energy and good resolution in order to observe the level structure over a reasonable region of excitation in the residual nucleus.

The subject of this thesis is the investigation of the (p,d) reaction on ^{24}Mg, ^{28}Si, ^{32}S, ^{36}Ar and ^{40}Ca. The primary objectives were to study the configuration mixing in the ground state wave functions of the target nuclei and the ℓ_n=2 J-dependence in the deuteron angular distributions. In addition, information concerning the level structure of the residual nuclei (^{23}Mg, ^{27}Si, ^{31}S, ^{35}Ar and ^{39}Ca) was obtained.

These experiments were performed with 33.6 MeV protons accelerated by the Michigan State University cyclotron. This bombarding energy was low enough to be compatible with the use of commercially available high resolution semiconductor detectors; at the same time it was high enough to expose 10 - 12 MeV of excitation in the residual nuclei, which was sufficient to achieve the goals of this work.

Chapter 2

Nuclear Models

A number of models have been constructed to explain the results of experiments in nuclear physics. Many of these have been introduced because of their success in other branches of physics. For example, the formalisms of the shell, Hartree-Fock and rotational models are used in atomic and molecular physics. Also, the superfluidity model results from techniques developed in superconductivity theory. Each model accounts for some of the observed nuclear properties but no one description successfully explains everything.

This chapter concerns some of the models that are commonly used to explain internal nuclear structure. A brief discussion of the shell models for spherical nuclei is given, and the single particle and collective models for non-spherical nuclei are described in more detail. The prediction of these models for the (p,d) reaction are discussed, and are later compared to the results of the present experiments (Chapters 5 and 6).

2.1 The Shell or Independent Particle Model

The shell model assumes that each nucleon is bound in a spherically symmetric potential and moves independently of other nucleons. A commonly used form for this potential is the isotropic harmonic oscillator

$$V(\vec{r}) = -V_0 + \tfrac{1}{2} m\omega^2 r^2 = -V_0 + \tfrac{1}{2} m\omega^2 (x^2+y^2+z^2)$$

Eq. 2.1

where V_0 is the depth of the well. The Schroedinger equation

$$\left[-\frac{\hbar^2}{2m}\nabla^2 + V(\vec{r})\right]\psi = E\psi$$

Eq. 2.2

is then solved for the potential of Eq. 2.1. Equation 2.2 is separable in both spherical and rectangular coordinates. The rectangular solution is

$$\psi_{n_1 n_2 n_3} = H_{n_1}(\sqrt{\alpha}\,x)\, H_{n_2}(\sqrt{\alpha}\,y)\, H_{n_3}(\sqrt{\alpha}\,z)\, \exp\left[-\frac{\alpha}{2}(x^2+y^2+z^2)\right]$$

Eq. 2.3

where the H_{n_i} are Hermite polynomials and

$$\alpha \equiv \frac{m\omega}{\hbar}$$

Eq. 2.4

The energy eigenvalues are

$$E_N = (n_1+\tfrac{1}{2})\hbar\omega + (n_2+\tfrac{1}{2})\hbar\omega + (n_3+\tfrac{1}{2})\hbar\omega$$
$$= (N+\tfrac{3}{2})\hbar\omega$$

Eq. 2.5

where $N=n_1+n_2+n_3$. The degeneracy of each energy level is $(N+1)\cdot(N+2)/2$, and the parity is given by $(-1)^N$.

In terms of spherical coordinates, the solution of Eq. 2.2 is

$$\psi_{N\ell m_\ell} = K_{N\ell}(r)\, Y_\ell^m(\theta,\phi)$$

Eq. 2.6

where N is the number of radial nodes minus ℓ. The spherical solution can be expanded in terms of the rectangular eigenfunctions (Eq. 2.3)

$$\psi_{N\ell m_\ell} = \sum_{n_1 n_2 n_3} a_{n_1 n_2 n_3} \psi_{n_1 n_2 n_3}$$

Eq. 2.7

with the following restrictions:

$$(-1)^\ell = (-1)^N$$

Eq. 2.8

$$\frac{(N+1)(N+2)}{2} = \sum_i (2\ell_i + 1)$$

Eq. 2.9

and $N=n_1+n_2+n_3$. The ℓ_i are the ℓ values allowed by Eq. 2.8 and the sum is from $\ell_i=0$ or 1 until Eq. 2.9 is satisfied for a given value of N. This is equivalent to saying that all states having the same $2N+\ell$ have the same energy, i.e., they are highly degenerate (Pr62). As can be seen from Eq. 2.5, they are also evenly spaced, which is contrary to the results of nuclear structure experiments. Other central potentials (e.g., the infinite square well) will split the ℓ-degeneracy so that levels having different (N,ℓ) quantum numbers have different energies. Since two identical nucleons can occupy a given $(N\ell m_\ell)$ state, Eq. 2.9 predicts the magic numbers 2, 8, 20, 40, 70, 112, ... for N=0, 1, 2, ... Only the first three of these

correspond to the experimental data on nuclear binding energies.

Some of these predictions were improved by the addition of a spin-orbit term to the central potential. This was first introduced by Mayer and Jensen in 1948 (Ma 55) to explain the magic numbers. In this case, Eq. 2.1 is replaced by

$$V(\vec{r}) = V_c(r) + V_{so}(r)\vec{l}\cdot\vec{s}$$

Eq. 2.10

where $V_c(r)$ and $V_{so}(r)$ are spherically symmetric and $\vec{l}$ and $\vec{s}$ are the orbital and spin angular momenta of a single nucleon. The "good" quantum numbers now become N, ℓ, j and m_j, where $\vec{j}=\vec{l}+\vec{s}$, and the degeneracies mentioned above are split such that the single particle energy depends on N, ℓ and j. Each level is still degenerate in the magnetic substates m_j, i.e., $2j+1$ identical particles can occupy an $(N\ell_j)$ state.

Although the effect of the spin-orbit term is rather large, it can be treated as a perturbation for purposes of illustration. The $\vec{l}\cdot\vec{s}$ operator can be written

$$\vec{l}\cdot\vec{s} = \tfrac{1}{2}\left[j^2 - l^2 - s^2\right]$$

Eq. 2.11

so that

$$\langle \vec{l}\cdot\vec{s} \rangle = \tfrac{1}{2}\left[j(j+1) - l(l+1) - s(s+1)\right]$$

Eq. 2.12

Since $j=\ell\pm 1/2$, we have

$$\langle \vec{\ell}\cdot\vec{s}\rangle = \begin{cases} \ell, & j=\ell+1/2 \\ -(\ell+1), & j=\ell-1/2 \end{cases}$$

Eq. 2.13

Since $V_{so}(r)$ in Eq. 2.10 is less than zero, the spin-orbit force is attractive for $j=\ell+1/2$ and repulsive for $j=\ell-1/2$. The $j=\ell+1/2$ level thus lies lower in energy than the $j=\ell-1/2$ level, which is generally consistent with the observed level order of spherical nuclei. The spin-orbit theory also correctly predicts the magic numbers: N or Z=2, 8, 20, 28, 50, 82 and N=126. Also, the level spacings are no longer equal.

This simple model still assumes that a nucleon moves in a potential $V(\vec{r})$ without being affected by the presence of other nucleons. Also, when there are two or more nucleons outside a closed shell, the j-j coupling of these nucleons leads to states of different total J, all of which are degenerate in the above model. Such is not the case in reality however, so various perturbations have been introduced to split these degeneracies. This perturbation is often some form of a two particle residual interaction. Also, the intermediate coupling model, which involves mixtures of the j-j and L-S coupling schemes, is used to predict the structure of light nuclei (Ku56, Co65). Both of these approaches result in wave functions which are super-

positions of (j-j coupled) shell model states. This is referred to as "configuration mixing", and the weighting factors in the expansion are called coefficients of fractional parentage (c.f.p.).

The spherical shell model fails to account for the large quadrupole moments and extensive configuration mixing observed in deformed nuclei. The treatment of such cases is described in the next section.

2.2 Collective Models and Deformed Nuclei

The formal description of collective nuclear models and single particle motions in deformed nuclei has been presented by several authors (Ni55, Bo53, Br64, Pr62, Ga64, He64). The treatment of Preston (Pr62), in conjunction with notes from the lectures of Gordon (Go65) is given in Sections 2.2.1 - 2.2.3. The first section concerns collective motions in general, and the contributions of particle motion are discussed in Sections 2.2.2 - 2.2.4.

2.2.1 Collective Motion

A number of nuclei in various mass regions are found to have unusually large quadrupole moments. These large moments cannot be accounted for by assuming the nucleons are bound in a spherical potential, and therefore must arise from the coordinated motion of many nucleons. For example, a spherical shell model predicts

that the quadrupole moment for odd A nuclei is due only to the effect of the last odd nucleon, which implies that the moment for odd Z nuclei is much greater than for those with odd N. These two moments are found to be comparable in the above mass regions however, and much larger than the spherical prediction. It is therefore assumed that these nuclei are non-spherical.

The surface of a deformed nucleus is described by an equation of the form

$$r(\theta', \phi') = R_0 \left[1 + \sum_{\lambda,\mu} \alpha_{\lambda\mu}^{(t)} Y_\lambda^\mu(\theta', \phi') \right]$$

Eq. 2.14

where θ' and ϕ' are variables of a space-fixed coordinate system and R_0 is constant. If $\lambda = 0$, the nuclear volume is allowed to change; we assume the nucleus is incompressible. Center of mass motion is implied by the $\lambda = 1$ terms, and this does not correspond to internal degrees of freedom. We are therefore interested only in terms involving $\lambda = 2, 3, \ldots$, which correspond to quadrupole, octupole, ..., distortions respectively. It will be assumed here that $\lambda = 2$ only. Then, transforming to the body fixed, principal axes (1,2,3) of the nucleus, Eq. 2.14 becomes

$$r(\theta, \phi) = R_0 \left[1 + \sum_{\nu=-2}^{+2} a_{2\nu}^{(t)} Y_2^\nu(\theta, \phi) \right]$$

Eq. 2.15

where the two coordinate systems are related by a rotation:

$$Y_2^{\mu}(\theta',\phi') = \sum_{\rho} Y_2^{\rho}(\theta,\phi)\,\mathcal{D}^{2}_{\mu\rho}(\Theta,\Phi,\Psi)$$

Eq. 2.16

In this system, the inertia tensor is diagonal so that $a_{21}=a_{2,-1}=0$. This leaves just two coefficients, which are defined in terms of the parameters β and γ:

$$a_{20} \equiv \beta \cos\gamma$$
$$a_{22} = a_{2-2} \equiv \frac{1}{\sqrt{2}}\beta\sin\gamma$$

Eq. 2.17

The five $(2\lambda+1)$ coordinates needed to specify the system are chosen as β, γ and the three Euler angles (Θ,Φ,Ψ) which define the transformation to the body fixed system. The parameter γ specifies the degree of symmetry of the system; if γ is a multiple of $\pi/3$ a symmetry axis exists. For example, if $\gamma=0$ or π the axis of symmetry is the 3-axis and $a_{22}=0$. β is a measure of the "amplitude" of the deformation and, assuming $\gamma=0$, is positive for a prolate (football) shape and negative for a oblate (pumpkin) shape. If β or γ is not constant in time, vibrational modes of motion exist. These are referred to as "β-vibrations" and "γ-vibrations" respectively.

If the collective motion is assumed to be similar to an irrotational flow of nuclear "liquid", the total energy is written as (Pré2)

$$E = \tfrac{1}{2} B \sum_{\mu} |\dot{\alpha}_{2\mu}|^2 + \tfrac{1}{2} C \sum_{\mu} |\alpha_{2\mu}|^2$$
$$= \tfrac{1}{2} B \dot{\beta}^2 + \tfrac{1}{2} C \beta^2 + \tfrac{1}{2} \sum_{k=1}^{3} \mathcal{I}_k \omega_k^2$$

Eq. 2.18

for $\gamma = 0$. The $\dot{\beta}^2$ and β^2 terms correspond to the kinetic and potential energies of a vibrational mode of frequency $\sqrt{C/B}$, where the potential term arises from the Coulomb and surface energies of the nucleus. The $\mathcal{I}_k$ in the last term of Eq. 2.18 are not moments of inertia in the usual sense, but arise from surface waves that make the nucleus <u>look</u> like it's rotating with angular velocity $\vec{\omega}$ in the space-fixed system. For example, if β is small, a small amount of nuclear matter is involved in the "rotation" and $\mathcal{I}$ will be small. Since $\gamma = 0$ here, there is no contribution to the rotational motion from rotations about the 3-axis (axis of symmetry), so $\mathcal{I}_3 = 0$. Also, since there is a symmetry axis, $\mathcal{I}_1 = \mathcal{I}_2$, and it can be shown that (Pro2)

$$\mathcal{I} = \mathcal{I}_1 = \mathcal{I}_2 = 3 B \beta^2$$

Eq. 2.19

The irrotational flow argument is quantized by writing the Hamiltonian for the total energy (Eq. 2.18) in the form

$$H = H_{vib}(\beta) + H_{rot}$$
$$= H_{vib} + \sum_{k=1}^{3} \frac{R_k^2}{2\mathcal{I}_k}$$

Eq. 2.20

where the R_K are the angular momentum components in the body fixed system. If β is nearly constant (i.e., a static deformation) H_{rot} will dominate in Eq. 2.20 and R^2, R_z and R_3 will be good quantum numbers:

$$\langle R^2 \rangle = J_R(J_R+1)\hbar^2$$
$$\langle R_z \rangle = M_R \hbar$$
$$\langle R_3 \rangle = K_R \hbar$$

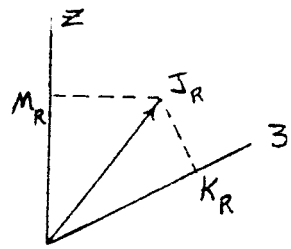

Eq. 2.21

Since axial symmetry was assumed, $\mathcal{I}_3=0$, and thus $R_3=K_R=0$. This implies that J_R must be integral. Setting $\mathcal{I}_1=\mathcal{I}_2=\mathcal{I}$, the rotational part of Eq. 2.20 is

$$H_{rot} = \frac{1}{2\mathcal{I}}(R_1^2+R_2^2) = \frac{1}{2\mathcal{I}}(R^2-R_3^2) = \frac{R^2}{2\mathcal{I}}$$

Eq. 2.22

which results in the energy eigenvalues

$$E_{J_R}(rot.) = \frac{\hbar^2}{2\mathcal{I}} J_R(J_R+1)$$

Eq. 2.23

Because of the symmetries of the nuclear shape, only states of even parity and even J_R can exist, i.e., $J_R^\pi=0^+$, 2^+, 4^+, etc., and the model applies only to even-even nuclei. If the nucleus is asymmetric ($\delta\neq 0$), $J_R^\pi=0^+$, 2^+, 3^+, 4^+, 5^+, etc. and K_R is restricted to even values for quadrupole distortions, except that $K_R=0$ is not allowed for odd values of J_R. Calculations involving asymmetric nuclei have been made by Davidov and Filippov (Da58). The parity is $(-)^\lambda$ in general, so octupole ($\lambda=3$) distortions must be introduced to obtain odd parity levels

in a rotational model.

In the above description it was assumed that β and γ were constants so that the rotational part of the Hamiltonian could be treated separately. Such a division is also justified when β- and γ-vibrations exist, if the rotational level spacing (Eq. 2.23) is much less than that of the vibrational levels. An equivalent assumption is that the frequency of the rotational motion is much less than the vibrational frequency. The addition of vibrational modes gives rise to rotational bands based on vibrational levels. For example, in the case of a β-vibration where $\gamma=0$, a $K_R=0$ rotational band is based on each vibrational state.

The results of the collective model are found to be in reasonable agreement with the low-lying level structure of heavy, deformed nuclei. The model describes light nuclei somewhat less successfully. Collective modes by themselves can be applied only to even-even nuclei however, since they predict only integral spins; even the vibrational quanta are bosons. The descriptions of deformed odd-A nuclei can also be included if the single particle motions are considered in addition to the collective properties. This coupling is discussed in the next section.

2.2.2 General Development of the Unified Model

In the unified model the motions of individual particles are coupled to the collective modes of motion:

$$H = H_p + H_{coll.}$$

Eq. 2.24

These ideas were first developed mathematically by Bohr and Mottelson (B052, B053), who assumed a particle Hamiltonian of the form

$$H_p = \sum_i \left(T_i + V(\beta, \gamma; \vec{r}_i, \vec{l}_i, \vec{s}_i) \right)$$

Eq. 2.25

where the summation is over the nucleons outside of some specified core. The potential V is taken to be

$$V = V_0 \left(\frac{r}{f(\beta, \gamma; \theta, \phi)} ; \vec{l}, \vec{s} \right)$$

Eq. 2.26

where $V_0(r; \vec{l}, \vec{s})$ is just a spherical shell model potential and f is a form factor which becomes unity for spherical nuclei ($\beta = \gamma = 0$). For axial symmetry and quadrupole distortions

$$f(\beta, 0; \theta\phi) = 1 + \beta Y_2^0(\theta, \phi)$$

Eq. 2.27

i.e., it is just the radial form factor used in the preceding section (Eq. 2.15). The coordinates (r, θ, ϕ) refer to the body-fixed system. Since H_p contains the

parameters β and γ, the Hamiltonian (Eq. 2.24) clearly contains coupling of the collective and single particle motions.

There are two extreme cases for which the problem can be solved. One of these is the so-called "weak coupling" case, where β is a small perturbation and the collective modes are small vibrations about a spherical shape. This solution is given in Ref. Pr62. The other extreme is the "strong coupling" case, which assumes a large permanent deformation and results in rotational bands based on single particle levels. This solution is outlined below for axially symmetric cases.

Assuming β and γ to be nearly constant, the collective part of the Hamiltonian (Eq. 2.24) is purely rotational:

$$H_{coll.} = H_{rot.} = \sum_{k=1}^{3} \frac{R_k^2}{2\mathcal{I}_k}$$

Eq. 2.28

This is identical to the H_{rot} in Eq. 2.20. Using Eqs. 2.25 and 2.28 in Eq. 2.24, the Schroedinger equation for the nucleus can be written as

$$\left[H_{rot.} + \sum_i \left(T_i + V(\beta, \gamma; \vec{r}_i, \vec{t}_i, \vec{s}_i)\right)\right] \Psi = E \Psi$$

Eq. 2.29

Defining $\vec{j}$, $\vec{R}$ and $\vec{J}$ as the particle, rotational and total angular momenta respectfully, we have

$$\vec{J} = \vec{R} + \vec{j}$$

$$\vec{j} = \sum_i \vec{j}_i$$

Eq. 2.30

The solutions to Eq. 2.29 are the $\Psi^{o}_{\alpha}(JMK\Omega)$ where $\hbar M=\langle Jz\rangle$, $\hbar K=\langle J_3\rangle$, $\hbar\Omega=\langle j_3\rangle$ and α corresponds to other quantum numbers for the particles. $K_R=0$ in the axially symmetric case, so $K=\Omega+K_R=\Omega$. A diagram showing the coupling of the angular momenta is shown in Fig. 2.1. Since the potential is not spherically symmetric, j^2 is not a constant of motion. It then follows that R^2 is not a good quantum number either.

Assuming axial symmetry ($\mathcal{I}_1=\mathcal{I}_2=\mathcal{I}$), Eq. 2.28 can be written

$$H_{rot.}=\frac{\vec{R}^2}{2\mathcal{I}}=\frac{1}{2\mathcal{I}}\left[(\vec{J}-\vec{j})^2-(J_3-j_3)^2\right]$$
$$=\frac{1}{2\mathcal{I}}\left[(\vec{J}-\vec{j})^2\right]=\frac{1}{2\mathcal{I}}\left[J^2+j^2-2\vec{J}\cdot\vec{j}\right]$$

Eq. 2.31

in analogy with Equation 2.22. The term involving j^2 involves only particle motion and can be included in the particle Hamiltonian:

$$H_o\equiv H_p+\frac{1}{2\mathcal{I}}j^2$$

Eq. 2.32

The matrix element of the remainder of Eq. 2.31 can be written

$$\frac{1}{2\mathcal{I}}\langle\left[J^2-2\vec{J}\cdot\vec{j}\right]\rangle=\frac{\hbar^2}{2\mathcal{I}}\left[J(J+1)-2K^2\right]-\frac{2}{2\mathcal{I}}\langle J_1j_1+J_2j_2\rangle$$

Eq. 2.33

The second term in Eq. 2.33 indicates that the rotational and particle coordinates are not completely separable.

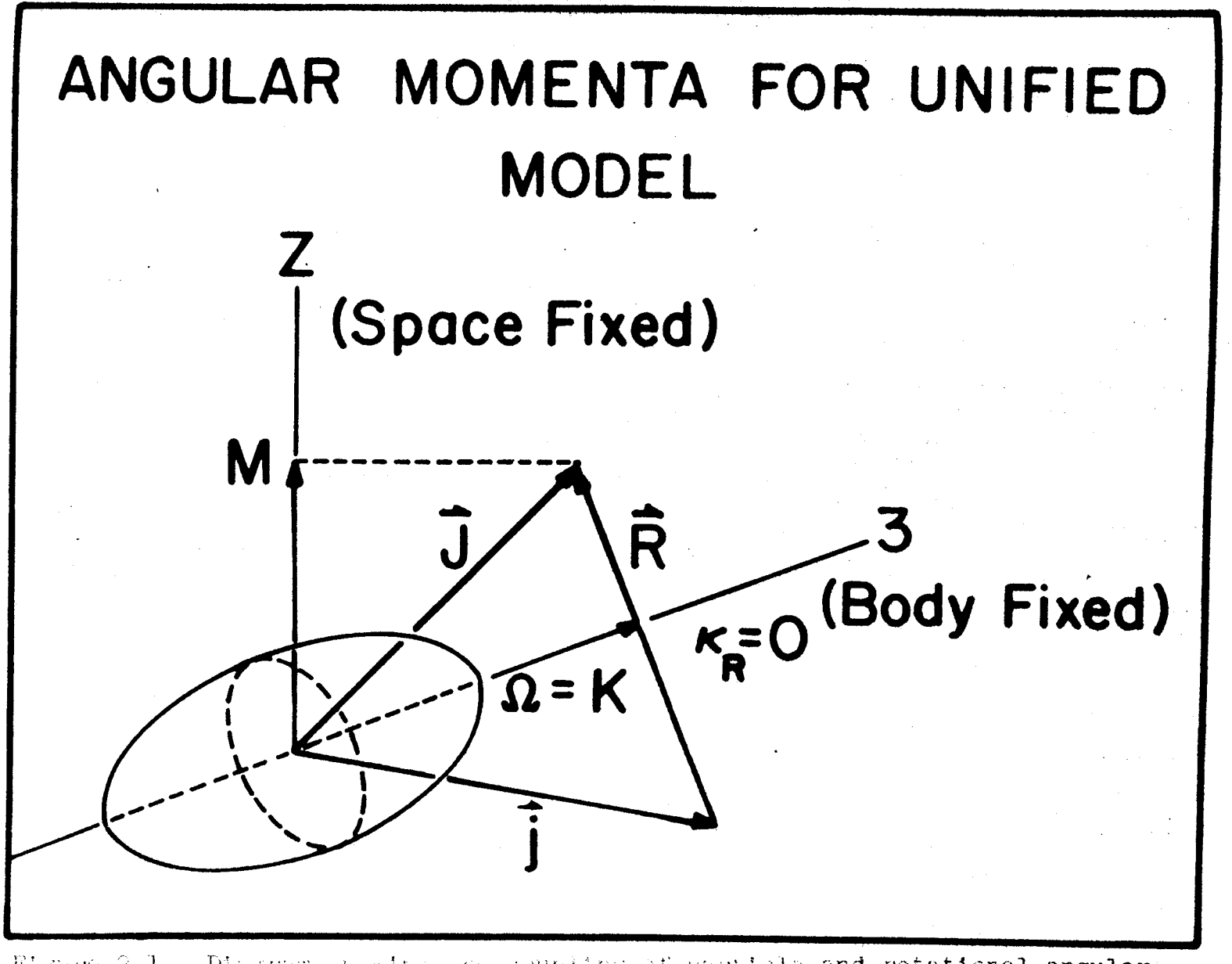

Figure 2.1. Diagram showing the coupling of particle and rotational angular momenta in the unified model.

Denoting this term by RPC (rotation-particle coupling) we can write

$$RPC \equiv -\frac{1}{2\mathcal{I}}\left[J_+ j_- + J_- j_+\right]$$

Eq. 2.34

where $J_\pm = J_1 \pm i J_2$ and $j_\pm = j_1 \pm i j_2$ are raising and lowering operators. The $J_\pm$ and $j_\pm$ operators change the value of the K quantum number to $K \pm 1$ when RPC operates on the total wave function $\Psi^o_\alpha(JMK)$. Thus RPC mixes states of different K, so that K is not really a good quantum number. In the cases of axial symmetry, however, RPC can be treated as a perturbation. Its matrix element then vanishes by the orthogonality of the $\Psi^o_\alpha(JMK)$, except when K=1/2.

The Schroedinger equation (Eq. 2.29) can be re-written as

$$\left[\frac{1}{2\mathcal{I}}\left(J^2 - 2J_3 j_3\right) + H_o + RPC\right]\Psi^o = E\Psi^o$$

Eq. 2.35

where H_o and RPC are given by Eqs. 2.32 and 2.34 respectively. The solutions to Eq. 2.35 involve both rotational and particle wave functions, where the normalized particle (intrinsic) wave functions are defined by

$$H_o \chi_{K\alpha} = \epsilon_{K\alpha} \chi_{K\alpha}$$

Eq. 2.36

Note that $\chi_{K\alpha}$ contains the coordinates of <u>all</u> the particles

outside of the assumed core (See Eqs. 2.25 and 2.32). If RPC=0, the solution to Eq. 2.35 is explicity

$$\Psi^{\sigma}_{\alpha}(JMK) = \sqrt{\frac{2J+1}{16\pi^2}}\left[\mathcal{D}^{J}_{MK}\chi_{K\alpha} + (-)^{J+2K}\mathcal{D}^{J}_{M-K}\sum_{j}(-)^{j}C_{jK}\chi^{(\alpha)}_{j-K}\right]$$

Eq. 2.37

where the $\mathcal{D}^{J}_{MK}$ are functions of the Euler angles. $\chi_{j,-K}$ is just some wave function having constant j, and is defined by the expansion

$$\chi_{K\alpha} = \sum_{j} C_{jK}\chi^{(\alpha)}_{jK}$$

Eq. 2.38

The total energy (Eq. 2.35) can now be written

$$E_{\alpha JK} = \underbrace{\epsilon_{K\alpha} - \frac{\hbar^2}{2\mathcal{I}}(2K^2)}_{E_p} + \underbrace{\frac{\hbar^2}{2\mathcal{I}}J(J+1)}_{E_{rot.}} + E^{(J)}_{RPC}\delta_{K,1/2}$$

Eq. 2.39

where

$$\delta_{K,1/2}E^{(J)}_{RPC} = \langle RPC\rangle = \frac{\hbar^2}{2\mathcal{I}}a(-1)^{J+1/2}(J+1/2)\delta_{K,1/2}$$

Eq. 2.40

and

$$a = -\sum_{j}(-1)^{j+1/2}(j+1/2)\left|C_{j\,1/2}\right|^2$$

Eq. 2.41

The total angular momentum (J) has the values K, K + 1, K + 2, etc. It is seen from Eq. 2.39 that states of +K

and $-K$ are degenerate. Equation 2.39 also shows that states of different K are actually different particle (or hole) states, each of which is the basis of a rotational band. If $K \neq 1/2$, the excitation energy within a band increases like $J(J+1)$ since $\langle RPC \rangle = 0$. For $K=1/2$ the ordering of the levels depends on the value obtained for a in Eq. 2.41. For the above treatment to be valid, it is necessary to separate the single particle and collective modes of motion (Eq. 2.24), which requires that the frequency of the collective rotation be much less than the frequency of the single particle motions.

The term labelled $\epsilon_{K\alpha}$ in Eq. 2.39 is still unknown, and is obtained by solving Eq. 2.36 for the particle wave functions. This procedure is outlined in the next section.

2.2.3 Single Particle States in Deformed Nuclei

Consider the Hamiltonian of Eq. 2.32 for a single particle. Then Eq. 2.36 may be written

$$\left[H_p + \frac{1}{2\mathcal{I}} j^2\right] \psi_{K\alpha} = \epsilon_{K\alpha} \psi_{K\alpha}$$

Eq. 2.42

where $\psi_{K\alpha}$ is a single particle wave function and

$$H_p = \frac{-\hbar^2}{2m} \nabla^2 + V\left(\frac{r}{f}; \vec{s}, \vec{l}\right)$$

Eq. 2.43

for one particle in the body-fixed system. The j^2 term is small and makes Eq. 2.42 non-separable. It is therefore neglected, which reduces the problem to solving

$$\left[\frac{-\hbar^2}{2m}\nabla^2 + V\left(\frac{r}{f};\vec{\lambda},\vec{s}\right)\right]\psi_{\alpha K} = E_{\alpha K}\psi_{\alpha K}$$

Eq. 2.44

From Eq. 2.27, the form factor is

$$f(\beta,\theta) = 1 + \beta Y_2^0(\theta)$$
$$= 1 + \beta\sqrt{\frac{5}{4\pi}}P_2(\cos\theta)$$

Eq. 2.45

for axial symmetry.

The solution of the anisotropic oscillator will be considered first. The potential V(r/f) for this case has the form

$$V\left(\frac{r}{f}\right) = \frac{1}{2}m\sum_{k=1}^{3}\omega_k^2 x_k^2$$

Eq. 2.46

This results in the frequencies

$$\omega_1 = \omega_2 = \omega_0(1+\delta/3)$$
$$\omega_3 = \omega_0(1-2/3\,\delta)$$

Eq. 2.47

where

$$\delta \equiv 3/2\sqrt{\frac{5}{4\pi}}\beta \simeq 0.95\beta$$

Eq. 2.48

and ω_0 is the frequency for an isotropic oscillator corresponding to the same nuclear volume. Introducing the coordinates

$$\xi_k \equiv \sqrt{\frac{m\omega_k}{\hbar}}\, x_k$$

Eq. 2.49

and using Eq. 2.46, a separable form is obtained for the Hamiltonian (Eq. 2.43):

$$H_p = \sum_k \frac{\hbar\omega_k}{2}\left(\frac{-\partial^2}{\partial\xi_k^2} + \xi_k^2\right)$$

Eq. 2.50

Then the solutions to Eq. 2.44 are just

$$|n_1 n_2 n_3\rangle = H_{n_1}(\xi_1)\, H_{n_2}(\xi_2) H_{n_3}(\xi_3)\, e^{-\xi^2/2}$$

Eq. 2.51

where the energy eigenvalues are

$$\begin{aligned} E_{n_1 n_2 n_3} &= \sum_k (n_k + 1/2)\hbar\omega_k \\ &= (n_1 + n_2 + 1)\hbar\omega_1 + (n_3 + 1/2)\hbar\omega_3 \\ &= (N + 3/2)\hbar\omega_1 + (n_3 + 1/2)\hbar(\omega_3 - \omega_1) \end{aligned}$$

Eq. 2.52

and $N = n_1 + n_2 + n_3$. Using Eq. 2.47, we obtain

$$E_{n_1 n_2 n_3} = (N + 3/2)\hbar\omega_0\left(1 + \delta/3\right) - (n_3 + 1/2)\hbar\omega_0\,\delta/3$$

Eq. 2.53

which reduces to the spherical case for $\delta = 0$ (See Sec. 2.1). These are the $\epsilon_{K\alpha}$ needed in Eq. 2.39 (for the

extreme single particle case), which are degenerate since $\omega_1 = \omega_2$. They are also degenerate with respect to K but this is remedied by the Nilsson model and is discussed later.

Another quantity of interest is a "pseudo angular momentum" which is defined by

$$\vec{\lambda} = -i\hbar\,\vec{\xi} \times \vec{\nabla}_\xi$$

Eq. 2.54

and is equal to $\vec{l}$ if $\xi = 0$. In the case of axial symmetry λ_3 is a constant of motion, which gives rise to another set of eigenfunctions that are also solutions of Eq. 2.47. They are the $|Nn_3\Lambda\rangle$ states, where

$$\langle \lambda_3 \rangle = \hbar\Lambda$$

Eq. 2.55

With the introduction of spins,

$$\langle s_3 \rangle = \hbar\Sigma$$

Eq. 2.56

and

$$\Lambda + \Sigma = K$$

Eq. 2.57

Again, λ^2 and j^2 are <u>not</u> constants of the motion, except in the spherical limit.

This model gives a poor description of spherical

nuclei, since it reduces to the spherical harmonic oscillator (Sec. 2.1) as δ approaches zero. However it does provide a suitable set of wave functions with which to improve the calculation. This was done first by Nilsson (Ni55), who solved the equation

$$[H_{h.o.} + H_{\epsilon} + C\vec{\lambda}\cdot\vec{s} + D\lambda^2]\psi = E\psi$$

Eq. 2.58

for the case of axial symmetry ($\gamma=0$). The spin orbit term is included in analogy with the spherical description, and the $D\lambda^2$ term splits the ℓ-degeneracy that arises in the spherical harmonic oscillator. The $H_{h.o.}$ term is just the spherical oscillator Hamiltonian, while H_{ϵ} is the H_p of Eq. 2.50. The solutions depend on the values of C and D, which are chosen to fit the data on spherical nuclei ($\delta=0$). The wave functions and energies (which now depend on K) are then calculated for various values of δ. The results are illustrated by the well known Nilsson diagram. The portion of this diagram relevant to the present work in the 2s-1d shell is shown in Fig. 2.2. The wave functions on the right are the $[Nn_3\Lambda]$ states, since for large distortions n_3 is nearly a constant of motion. The values of K and the parity are also shown. For large distortions, the nuclear volume tends to change so that ω_0 is no longer independent of δ; it is then convenient to introduce the parameter

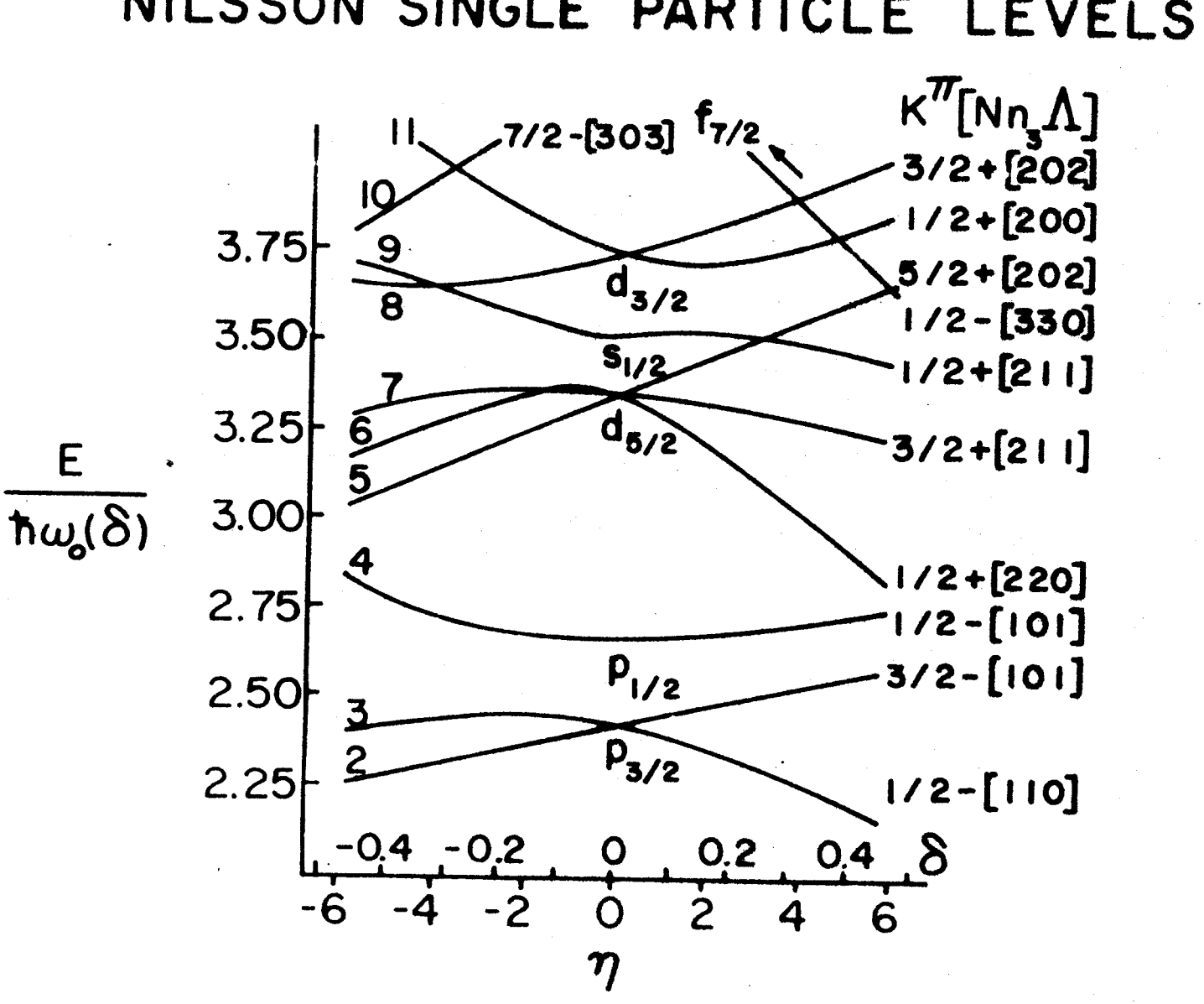

Figure 2.2. Nilsson diagram of single particle levels in a deformed well (Ni55). Each level can hold two protons and two neutrons; the first K=1/2 ($1s_{1/2}$) level is not shown.

$$\eta \equiv \frac{2\delta \hbar \omega_0(\delta)}{C}$$

Eq. 2.59

which is also shown.

The solutions to Eq. 2.58 ($\psi_{\alpha K}^{(S)}$) may be expanded in a number of representations, e.g.,

$$\psi_{\alpha K} = \sum a_{l\Lambda} |N l \Lambda \Sigma\rangle$$

Eq. 2.60

where $|N l \Lambda \Sigma\rangle$ are the spherical oscillator solutions and $\Lambda+\Sigma=K$. The quantum number α defines the particular Nilsson orbit for a given value of N and K. Also, as mentioned above, for large deformations

$$\psi_{\alpha K} \simeq |N n_3 \Lambda K\rangle$$

Eq. 2.61

which are just the solutions for the Hamiltonian of Eq. 2.50. Chi (Ch66) and others (Ba66, Ba67) have expanded the $\psi_{\alpha K}$ in terms of the shell model states $|N l j K\rangle$ (See Sec. 2.1):

$$\psi_{\alpha K} = \sum_{j=K}^{j_{max.}} C_{jK}(\alpha) |N l j K\rangle$$

Eq. 2.62

where j_{max} is determined by N, and $l = j \pm 1/2$ is restricted by $\pi = (-)^l = (-)^N$.

Equations 2.60 - 2.62 involve only <u>single</u> particle

wave functions, and in general more than one particle outside a closed core is included. In this case, the total particle wave function is (in the notation of Eq. 2.36)

$$\chi_{K\alpha} = \psi_{\alpha_q K_q} \psi_{\alpha_{q-1} K_{q-1}} \cdots \psi_{\alpha_2 K_2} \psi_{\alpha_1 K_1} \left| Core \right\rangle_{intrinsic}$$

Eq. 2.63

for q nucleons. If q is even, K=0 in the ground state, and $K=K_q$ if q is odd. The $\psi_{\alpha_i K_i}$ thus act as particle "creation operators" operating on $|core\rangle$.

The equilibruim shape (i.e., the deformation parameters) may be found for a particular nucleus by including all the particles in Eqs. 2.44 or 2.58. The total nuclear energy is then deduced from the particle energy and is minimized by requiring that $\frac{\partial E}{\partial \delta} = \frac{\partial E}{\partial \beta} = 0$. This method is discussed in detail in Ref. Pr62.

The Nilsson model has been quite successful in explaining the low-lying levels of some nuclei in the 2s-1d shell and in the rare earth region. This calculation was done for a symmetric nucleus, and has been extended by Newton (Ne60) to include asymmetric cases ($\delta \neq 0$).

2.2.4 Information from the (p,d) Reaction*

The (p,d) reaction excites mainly hole states in

* The author is indebted to L. Zamick for his helpful explanation of this subject.

the residual nucleus by a direct reaction mechanism. Since the transfer of a single nucleon is involved, the information obtained is related only to the particle wave function, independent of the collective motion. All of the target nuclei in this study have $J^{\pi}=0^{+}$ in the ground state so that $K_R=K=J_R=J=0$. Therefore, when a neutron is removed, the spin and parity of the final nuclear state (J_f^{π}) is equal to that of the picked up neutron (j_n^{π}). We have seen, however, that j_n is not a good quantum number in the deformed single particle wave function (Secs. 2.2.2 - 2.2.3).

The removal of a neutron from a non-spherical nucleus may be represented by a destruction operator ("hole" wave function) operating on the target ground state (Eq. 2.63):

$$\psi^{\dagger}_{\alpha_n K_n}\chi_{\alpha\alpha} = \psi^{\dagger}_{\alpha_n K_n}\psi_{\alpha_g K_g}\psi_{\alpha_{g-1} K_{g-1}}\cdots\psi_{\alpha_n K_n}\cdots\psi_{\alpha_1 K_1}\left|\text{Core}\right\rangle_{\text{int.}}$$

Eq. 2.64

which is just the particle wave function of the final nucleus. The $\psi^{\dagger}_{\alpha_n K_n}$ cancels the $\psi_{\alpha_n K_n}$ of the picked up neutron, leaving the final nucleus wave function with $K_f=K_n$ and energy depending on K_n and α_n. It is seen then, that the spin of the final state can be any of the j_n's in the expansion

$$\psi_{\alpha_n K_n} = \sum_{j_n=K_n}^{j_n(\text{max.})} C_{j_n K_n}^{(\alpha_n)}\left|N\ell_n j_n K_n\right\rangle$$

Eq. 2.65

which is similar to Eq. 2.62. For example, if $K_n^{\pi}=1/2^+$ and N=2 (e.g., Nilsson orbits 6, 9 or 11 in Fig. 2.2), Eq. 2.65 becomes

$$\psi_{\alpha_n 1/2} = C_{1/2\,1/2}^{(\alpha_n)} \underbrace{|2\,0\,1/2\,1/2\rangle}_{2s_{1/2}} + C_{3/2\,1/2}^{(\alpha_n)} \underbrace{|2\,2\,3/2\,1/2\rangle}_{1d_{3/2}} + C_{5/2\,1/2}^{(\alpha_n)} \underbrace{|2\,2\,5/2\,1/2\rangle}_{1d_{5/2}}$$

Eq. 2.66

Direct neutron pick-ups from one of the $K^{\pi}=1/2^+$, N=2 Nilsson orbits thus excite three levels having spins and parities $1/2^+$, $3/2^+$ and $5/2^+$, which also correspond to members of a rotational band based on the Nilsson orbit. The experimentally obtained (p,d) spectroscopic factors (Chapter 6) are therefore measures of the $|C_{j_n K_n}^{(\alpha_n)}|^2$ in Eq. 2.65. The calculation of theoretical spectroscopic factors from Eq. 2.65 is outlined in Appendix A, and the values obtained from the wave functions of Chi (Ch66) are compared to experiment in Chapter 6.

Chapter 3

The Distorted Wave Theory for Pick-up and Stripping Reactions

The theoretical formalism for direct reactions in the distorted wave Born approximation has been treated in detail by Tobocman (To61) and Satchler (Sa64). Some of the relevant results are presented here. Particular attention is given to a discussion of form factors for the nuclear bound states and the extraction of spectroscopic factors.

The direct interaction model for nuclear reactions is based on the assumption that the reaction is a one step process, without the formation of an intermediate nuclear state. Direct reactions were first described by the plane wave Born approximation, which predicted a cross-section that was strongly peaked for small angles of the emitted particles (Bu51). This theory treated the interaction as a perturbation of plane waves, while the distorted wave Born approximation (DWBA) involves the perturbation of elastically scattered waves. The predicted DWBA cross-sections are similar to those of the plane wave theory and are more consistent with experimental results.

3.1 Analogies in the Distorted and Plane Wave Formalisms

3.1.1 The Plane Wave Born Approximation

Consider the simple case of scattering from a

potential well $V(\vec{r})$. The exact asymptotic solution for the total wave function in the center of momentum system is

$$\psi(\vec{k},\vec{r}) = e^{i\vec{k}\cdot\vec{r}} - \left[\frac{\mu}{2\pi\hbar^2}\int e^{i\vec{k}\cdot\vec{r}'} V(\vec{r}')\,\psi(\vec{k},\vec{r}')\,d\vec{r}'\right]\frac{e^{ikr}}{r}$$

Eq. 3.1

where μ is the reduced mass of the scattered particle. The Born approximation consists of setting

$$\psi(\vec{k},\vec{r}') \simeq e^{i\vec{k}\cdot\vec{r}'}$$

Eq. 3.2

in the integral of Eq. 3.1. Defining the quantity in brackets as $-f(\theta)$, we then have

$$\psi(\vec{k},\vec{r}) \rightarrow e^{i\vec{k}\cdot\vec{r}} + f(\theta)\frac{e^{ikr}}{r}$$

Eq. 3.3

where $f(\theta)$ is the plane wave scattering amplitude. The angular dependence is determined by the momentum transfer $\vec{k}'-\vec{k}$. It can then be shown that the differential cross-section is given by

$$\frac{d\sigma(\theta)}{d\Omega} = |f(\theta)|^2$$

Eq. 3.4

In this case, the potential acted as a perturbation to an incoming plane wave to produce outgoing spherical waves, i.e., it was an interaction between plane wave states. To predict the cross-section, one must evaluate

$f(\Theta)$ for some specified $V(\vec{r})$.

3.1.2 The Distorted Wave Born Approximation

The total wave function for the reaction A(d,p)B is given asymptotically by*

$$\Psi_{dp}(\vec{k}_d,\vec{r}_d) \rightarrow \psi_d \psi_A e^{i\vec{k}_d\cdot\vec{r}_d} - \frac{\mu_p}{2\pi\hbar^2} T_{dp} \psi_B \frac{e^{ik_p r_p}}{r_p}$$

Eq. 3.5

where, in the exact case, the transition amplitude T_{dp} is

$$T_{dp} = \langle \psi_B(\xi, \vec{r}_{An}) \chi_p^-(\vec{k}_p,\vec{r}_p) | V_{pB} - \bar{V}_{pB} | \Psi_{dp}^+(\vec{k}_d,\vec{r}_d) \rangle + \delta_{d,p} f_d(\vec{k}_p, k_d)$$

Eq. 3.6

The second term relates only to elastic scattering and thus vanishes for the (d,p) reaction. The vectors $\vec{k}_i$, $\vec{r}_i$ refer to the momentum and position of particle i in the center of momentum system. The internal wave functions of the particles $\psi_i(\xi, r_{jk})$ have been included; ξ refers to the internal coordinates of the sub-units of nucleus i and the $\vec{r}_{jk}$ are the relative coordinates of these sub-units. The $\chi_i^-(\vec{k}_i,\vec{r}_i)$ and χ_i^+ are the distorted waves for particle i, with outgoing and incoming boundry conditions, respectively. They are generated from an optical model-plus-Coulomb potential. V_{pB} is the interaction between p and B in the exit channel; $\bar{V}_{pB}$ is the optical

---

*Equations 3.5 and 3.6 are derived in refs. To61 and Gl65(a).

potential in the exit channel. Effects due to isospin, Coulomb phases and the Exclusion Principle are ignored for simplicity.

The distorted wave Born approximation consists of approximating the total wave function $\Psi^{(+)}_{dp}(\vec{k}_d, \vec{r}_d)$ in Eq. 3.6 by the total incident channel wave function:

$$\Psi^{(+)}_{dp} \approx \psi_d(\vec{r}_{np})\,\psi_A(\xi)\,\chi^{(+)}_d(\vec{k}_d, \vec{r}_d)$$

Eq. 3.7

The interaction V_{pB} can be written

$$V_{pB} = V_{pn} + V_{pA}$$

Eq. 3.8

so that

$$V_{pB} - \bar{V}_{pB} = V_{pn} + V_{pA} - \bar{V}_{pB} \approx V_{pn}$$

Eq. 3.9

i.e., the difference between V_{pA} and $\bar{V}_{pB}$ is assumed to be negligible. Using equations 3.7 and 3.9, the transition amplitude of Eq. 3.6 becomes

$$T_{dp} = \langle \psi_B(\xi, \vec{r}_{An})\,\chi^{(-)}_p(\vec{k}_p, \vec{r}_p) \,|\, V_{pn} \,|\, \psi_d(\vec{r}_{np})\,\psi_A(\xi)\,\chi^{(+)}_d(\vec{k}_d, \vec{r}_d) \rangle$$

Eq. 3.10

The (d,p) cross-section is then given by

$$\frac{d\sigma}{d\Omega}(\theta) = \frac{\mu_p \mu_d}{(2\pi\hbar^2)^2} \frac{k_p}{k_d} |T_{dp}|^2$$

Eq. 3.11

in analogy with Eq. 3.4.

Thus, in the distorted wave Born approximation, the potential V_{np} (for the (d,p) reaction) acts as a perturbation to the "distorted" or optical model wave functions, just as $V(\vec{r})$ perturbed the plane wave in Sec. 3.1.1. This allows the perturbation to affect both elastically scattered waves and plane waves. This is illustrated by the asymptotic form of the distorted waves:

$$\chi^{+} \longrightarrow e^{i\vec{k}\cdot\vec{r}} + f(\theta)\frac{e^{ikr}}{r}$$

Eq. 3.12

The transition is thus one between the elastic scattering states of the target and residual nuclei. Again, the problem lies in evaluating the transition amplitude T for a given interaction. This is done for the (d,p) and (p,d) reactions in the zero range approximation in Appendix B. The results of this calculation are used in the next section.

3.2 Extraction of (p,d) Spectroscopic Factors.

The transition amplitude for the A(d,p)B stripping reaction is calculated in Appendix B, where the expression

$$\left(\frac{d\sigma}{d\Omega}\right)_{dp} = \frac{2(2J_B+1)}{(2J_A+1)(2s_n+1)} \sum_{l,j} D_0^2 S_{lj}\, \sigma_{lj}(\theta)_{dp}$$

Eq. 3.13

is obtained for the (d,p) cross-section. D_0 is the zero range parameter ($D_0^2 \approx 1.5\times10^4$ MeV^{2}fm^3), S_{lj} is the spectroscopic factor and $\sigma_{lj}(\theta)_{dp}$ is the "reduced" (d,p) cross-

section.

The cross-section for the inverse B(p,d)A pick-up reaction is related to the (d,p) cross-section by (To61):

$$\left(\frac{d\sigma}{d\Omega}\right)_{pd} = \frac{k_d^2}{k_p^2}\frac{(2s_d+1)(2J_A+1)}{(2s_p+1)(2J_B+1)}\left(\frac{d\sigma}{d\Omega}\right)_{dp}$$

Eq. 3.14

Combining Eqs. 3.13 and 3.14,

$$\left(\frac{d\sigma}{d\Omega}\right)_{pd} = \frac{2(2s_d+1)}{(2s_p+1)(2s_n+1)}\sum_{l,j} S_{lj}\, D_o^2\, \sigma_{lj}(\theta)_{pd}$$

Eq. 3.15

where l and j are the angular momentum quantum numbers of the picked up neutron and s_i is the intrinsic spin of particle i. The reduced (p,d) cross-section is

$$\sigma_{lj}(\theta)_{pd} = \frac{\mu_p \mu_d}{(2\pi\hbar^2)^2}\frac{k_d}{k_p}\sum_m \left|\beta^{lm}_{s_n j}\right|^2 = \frac{k_d^2}{k_p^2}\sigma_{lj}(\theta)_{dp}$$

Eq. 3.16

where $\beta^{lm}_{s_n j}$ is the "reduced amplitude". The quantity

$$\sigma^{lj}_{DWBA}(\theta) \equiv \frac{2(2s_d+1)\times 10^4}{(2s_p+1)(2s_n+1)}\sigma_{lj}(\theta)_{pd} = \frac{3}{2}\sigma_{lj}(\theta)_{pd}\times 10^4$$

Eq. 3.17

is calculated by the Macefield computer code with a specified l and j for the picked up neutron bound in a

Woods-Saxon well of a given shape. Only the factor $\sigma_{\ell j}(\theta)_{pd} \times 10^4$ is calculated by the Oak Ridge program JULIE, so that

$$\sigma_{JULIE} \times 3/2 = \sigma_{MACEFIELD}$$

Eq. 3.18

The units in Eq. 3.17 have the masses in proton mass units, energies in MeV and length in fermis. The factor 10^4, which arose in the value for D_o^2 (see above), is also included. Equation 3.15 now becomes

$$\left(\frac{d\sigma}{d\Omega}\right)_{pd} = D_o^2 \times 10^{-1} \sum_{\ell,j} S_{\ell j} \sigma^{\ell j}_{(\theta)\,DWBA} \approx 1.5 \sum_{\ell,j} S_{\ell j} \sigma^{\ell j}_{(\theta)\,DWBA}$$

Eq. 3.19

The ℓ and j values that the picked up neutron is allowed to have for a transition from some initial state $J_B^{\pi_B}$ to a final state $J_A^{\pi_A}$ are limited by two selection rules. One, the spin of the target must be equal to the j of the picked up neutron coupled to the spin of the residual nucleus; i.e.,

$$\vec{J}_A = \vec{j} + \vec{J}_B \quad \text{or}$$

$$J_A + J_B \geq j \geq |J_A - J_B|$$

Eq. 3.20

Secondly, the parity of the final state must be

$$P_A = (-)^{\ell} P_B$$

Eq. 3.21

If the target spin is zero, as is the case for all targets in the work reported here, $j = J_A$ only, and since $\ell = j \pm 1/2$, only one ℓ is allowed for a given parity change. When measuring $S_{\ell j}$ experimentally, the experimental (p,d) cross-section is used for $(d\sigma/d\Omega)_{pd}$ in Eq. 3.19. The spectroscopic factor is then given by

$$S_{\ell j} = \left(\frac{d\sigma}{d\Omega}\right)_{pd}^{Exp.} \Big/ \left(1.5\, \sigma_{DWBA}^{\ell j}(\theta)\right)$$

Eq. 3.22

It is this equation that is used in Chapter 6 to extract the spectroscopic factors given there.

The physical significance of $S_{\ell j}$ can be seen by expanding the wave function of the target nucleus (B) in terms of the states of the residual nucleus (A) coupled to a bound neutron:

$$|\psi_B^{J_B M_B}\rangle = \sum_{\substack{j'\mu' \\ J_A' M_A'}} \alpha_{\ell j'} |\psi_A^{J_A' M_A'} \psi_n^{\ell j' \mu'}\rangle (J_A' j' M_A' \mu' | J_B M_B)$$

Eq. 3.23

Here, the $\alpha_{\ell j}$ are the coefficients of fractional parentage (c.f.p.) and $\psi_n^{\ell j \mu}$ is the wave function of a neutron bound in an (ℓ, j) orbit. Projecting $\alpha_{\ell j}$ out of Eq. 3.23 we obtain for $S_{\ell j}$

$$S_{\ell j} = n_{\ell j} |\alpha_{\ell j}|^2 = \frac{n_{\ell j} |\langle \psi_A^{J_A M_A} \psi_n^{\ell j \mu} | \psi_B^{J_B M_B}\rangle|^2}{(J_A j M_A \mu | J_B M_B)^2}$$

Eq. 3.24

where $n_{\ell j}$ is the number of neutrons in the (ℓ, j) orbit. Thus, the spectroscopic factor is proportional to the square of the overlap of the initial state $\psi_B^{J_B M_B}$ with the final state coupled to the picked up neutron.

3.3 Discussion of Bound State Form Factor

The radial part of the neutron wave function, $\mathcal{U}_{\ell j}(r_{nA})$, is often referred to as the neutron "form factor". It was originally assumed that this quantity was involved in the details of the reaction mechanism, and that all the nuclear structure properties could be collected in the spectroscopic factor (Fr60). Recent pick-up and stripping experiments have shown that the angular distributions depend on the J-value of the final nuclear state, even though the ℓ of the transferred particle is the same (Ko67, Wh66, Sh65, Gl65(a), Le64, Sh64). This indicates that there exists an interdependence between reaction mechanisms and nuclear structure which cannot be ignored (Pi65).

Equation 3.24 shows that the spectroscopic factor obtained is sensitive to the neutron wave function $\psi_n^{nlj,m}$, the radial part of which is just the $\mathcal{U}_{\ell j}(r_{nA})$. The form factor also affects the shape of the calculated angular distribution (Eq. 3.16 and 3.17), since the form factor enters into the integration over the partial waves (Appendix B).

The usual method for obtaining this form factor is to assume a spherical (Woods-Saxon) potential whose

radius ($R=r_0A^{1/3}$) and diffuseness (a) is similar to that used for the optical model central potential:

$$V(r) = \frac{-V_0}{1+\exp\left(\frac{r-r_0A^{1/3}}{a}\right)}$$

Eq. 3.25

The depth (V_0) is then determined by the separation energy of the picked up neutron, which also gives the correct asymptotic form to the neutron wave function.

If one wishes to explain the observed J-dependence in a way that does not explicitly involve the elastic scattering wave functions, the neutron form factor cannot be the same for $j=\ell+1/2$ and $j=\ell-1/2$. The addition of a spin orbit term to Eq. 3.25 would seem to be an obvious move at this point; it is well known from the shell model that the $\vec{\ell}\cdot\vec{s}$ potential acting on a bound nucleon is strong. This is a surface potential which is attractive for $j=\ell+1/2$ and repulsive for $j=\ell-1/2$, with the result that the overall radius of V(r) would be larger for $j=\ell+1/2$ than for $j=\ell-1/2$. However, the DWBA calculation then predicts that the position of the forward maximum for a $j=\ell+1/2$ distribution occurs at a smaller angle than that for $j=\ell-1/2$, which is contrary to the effect observed experimentally for $\ell=2$ and $\ell=3$ (Ko67, G165(a), Sh64, Sh65, and Chapters 5 and 6).

There have been two other main approaches to this problem. One is to assume different binding energies

for neutrons that have different spins, even though their separation energies may be nearly the same. Both Sherr et. al. (Sh64) and Glashausser (Gl65(a)) have obtained satisfactory DWBA fits to the $\ell = 3$ J-dependence using this method. Pinkston and Satchler (Pi65) have shown, however, that this approach is wrong in principle. In order to obtain the correct asymptotic form for the neutron wave function, the correct separation energy must be used. The wave function must decrease asymptotically as e^{-Kr} where

$$K^2 = 2M(E_B - E_A)/\hbar^2$$

Eq. 3.26

Therefore, the shape of the well must be changed in a way that does not affect the neutron binding energy. Pinkston and Satchler have suggested changes in radius or diffuseness.

An attempt to fit the $\ell_n = 3$ J-dependence in the $^{56}Fe(p,d)^{55}Fe$ reaction by changing the neutron well radius (e. g., r_o in Eq. 3.25) has been made by Glashausser (Gl65(a)), and was partially successful at his highest bombarding energy (27.5 MeV). The same method has been used to fit the $\ell_n = 2$ J-dependence here in the (p,d) reaction, where it was also partially successful. These results are discussed in detail in Chapter 6.

Chapter 4

Experimental Methods

4.1 Experimental Arrangement

4.1.1 Cyclotron and Beam System

The 33.6 MeV protons used to study the (p,d) reaction were obtained by accelerating negative hydrogen ions in the 64 in. Michigan State University sector-focusing cyclotron (Blue). The experiments were performed in a 36 in. scattering chamber. A schematic diagram of the cyclotron, and beam system is shown in Fig. 4.1, while a more detailed sketch of the scattering chamber and experimental arrangement is shown in Fig. 4.2.

A single turn was extracted from the cyclotron with a 0.0001 in. aluminum stripper foil placed near the edge of the magnetic field (Fig. 4.1). The beam was directed through a three-slit collimation system into the scattering chamber with a 20° bending magnet; a fine control of the horizontal and vertical positions of the beam was supplied by two "kinking" magnets (K_1 and K_2 in Fig. 4.1). The horizontally and vertically focusing quadrupole magnets were adjusted to minimize the size of the beam spot observed on a quartz scintillator. The viewer was then removed, and final adjustments were made by equalizing the beam currents (I_1 and I_2 in Fig. 4.2) on the sides of the vertical slit behind the scattering chamber. The slit opening

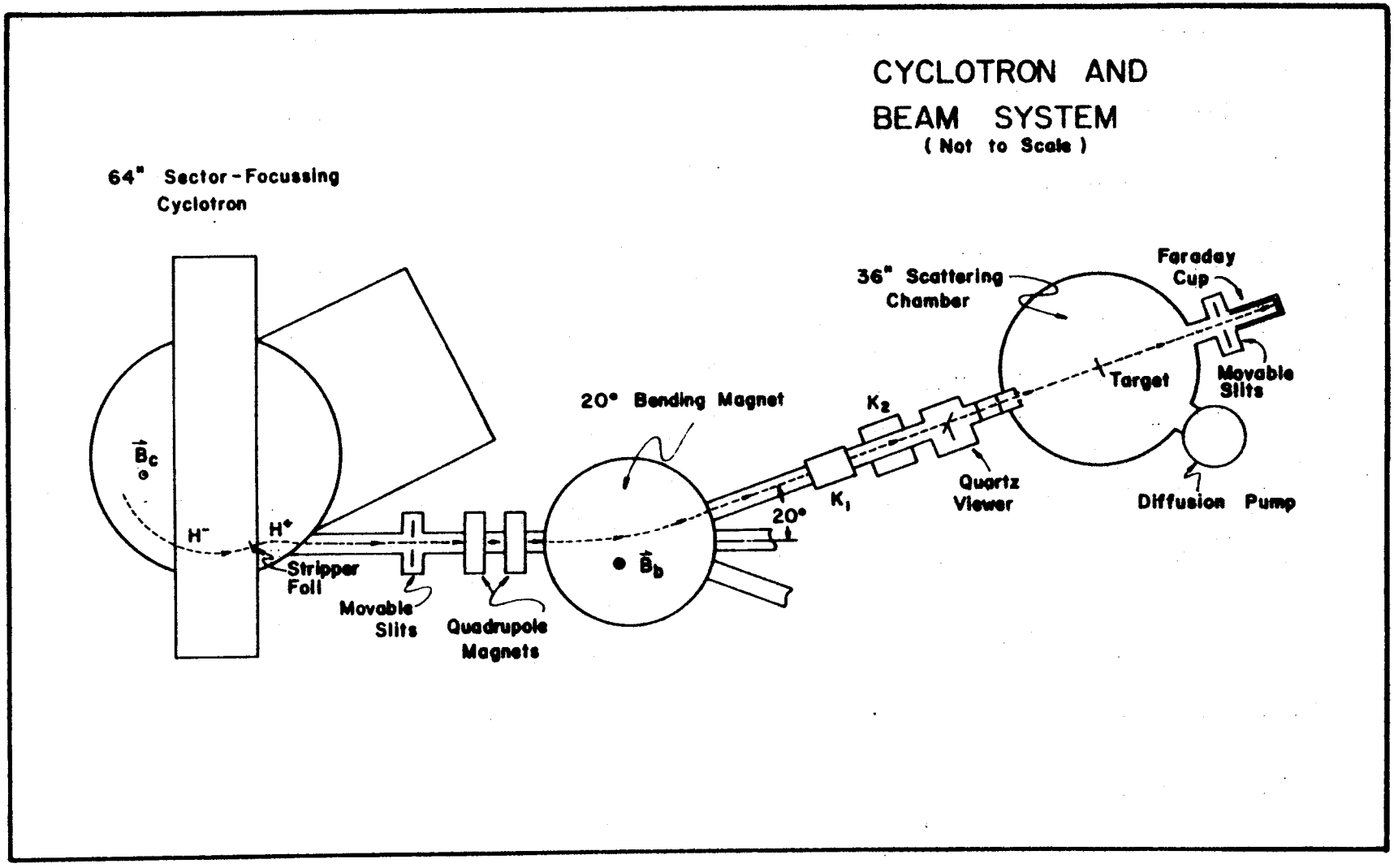

Figure 4.1. Schematic diagram of cyclotron and beam system.

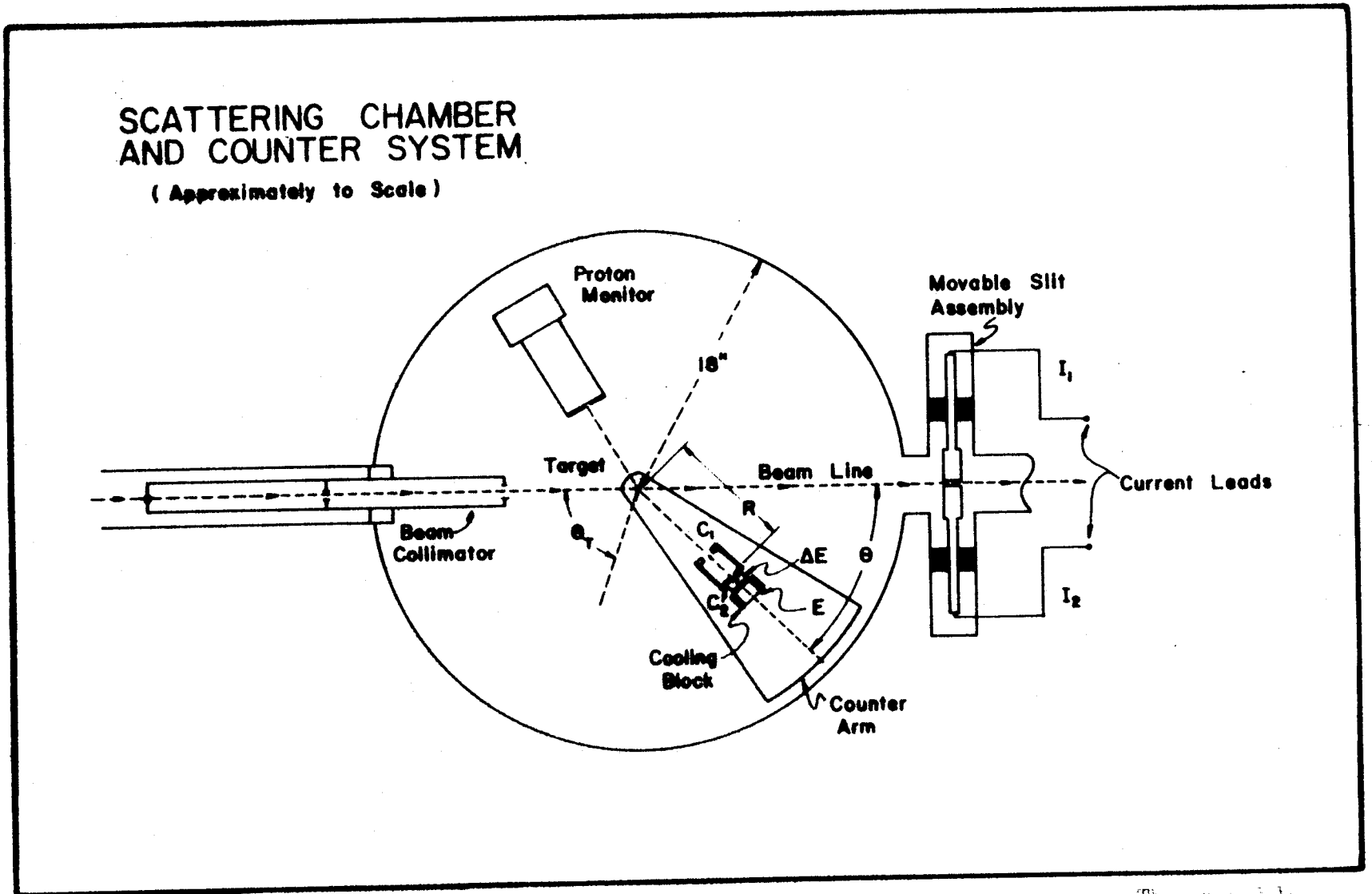

Figure 4.2. Experimental arrangement in the 36 in. scattering chamber. The movable slit assembly was used to insure proper beam alignment.

was approximately 0.1 in., and was previously aligned with both the center of the scattering chamber and the collimator in front of the chamber. The beam pipe was cleared by opening the slit after the proper alignment was obtained. The above procedure resulted in a beam diameter of approximately 0.25 in. at the center of the scattering chamber.

The beam was collected in a Faraday cup at the rear of the scattering chamber during the experimental runs (Fig. 4.1) and the charge was summed by a current integrator with an error of less than 1%. Beam currents from 1 nA to 100 nA were used, depending on the scattering angle (θ in Fig. 4.2).

4.1.2 Scattering Chamber Set-up

A 1 in. x 1 in. target containing the nuclei under investigation was mounted in the center of the scattering chamber as shown in Fig. 4.2. An angular accuracy of $\pm 2^{\circ}$ was achieved in setting the target angle (θ_T) by remote control. The reaction products were observed with a (dE/dx)-E counter telescope consisting of a 279μ silicon surface-barrier detector (ΔE) and a 3mm lithium drifted silicon counter (E). This thickness for the ΔE counter would stop only those deuterons having energy $\lesssim 8$ MeV, which permitted the observation of 10 - 12 MeV of excitation in the nuclei studied. The lithium-drifted E counter was cooled to approximately dry ice temperature

(-77° C) by circulating cooled methyl alcohol through the copper block shown in Fig. 4.2. The telescope was mounted on a movable arm in the scattering chamber which could be positioned by remote control to an angular accuracy of $\pm$ 0.5°. Two collimators (C_1 and C_2) were placed in front of the telescope. Collimator C_1 consisted of a 0.5 in. diameter aperture in copper of 0.25 in. thickness, and was used to shield the detectors from possible scattering from the target frame. Brass plates were attached to the sides of C_1 to provide additional shielding. The solid angle was defined by a tantalum collimator (C_2) having a circular aperture of 0.152$\pm$0.001 in. diameter and 0.060 in. thickness. This thickness was sufficient to stop protons of the bombarding energy (33.6 MeV) and the most energetic deuterons encountered in this work (~21 MeV). The distance from the target (R) was typically about 10 in., which corresponds to a subtended angle of $\lesssim 1°$ and a solid angle of $\sim 2 \times 10^{-4}$ steradians. When the ^{36}Ar and H_2S gas targets were used, two collimators were used to define the solid angle, and a brass collimator with a slit width of 0.125 in. was used in place of C_1. The use of gas targets is discussed in more detail in Sec. 4.4.2.

A cesium iodide monitor counter was placed at a fixed scattering angle of 120° and was used to observe elastically scattered protons (Fig. 4.2). This served as a normalization check on the absolute differential cross-section measurements in addition to the current integrator.

The 0.25 in. x 0.5 in. CsI crystal was collimated with a 0.125 in. diameter aperture in tantalum of ~0.125 in. thickness. This same detector was used to obtain the $^{26}Mg(p,p)^{26}Mg$ and $^{36}Ar(p,p)^{36}Ar$ elastic scattering data with an overall resolution of ~650 keV.

4.1.3 Electronics

(a) (p,d) Reaction

A schematic block diagram of the electronics used in this work is shown in Fig. 4.3. The "free" electrons produced by charged particles in the E and ΔE detectors were swept from the counters with bias voltages of 400 - 500 V. and 60 V. respectively. The resultant pulses were amplified by charge sensitive preamplifiers, which were connected to the detectors through a side port in the scattering chamber with approximately 3 ft. of 125Ω coaxial cable having 9.3 pf/ft. capacitance. The pulses were further amplified by Goulding amplifiers and sorted by a particle identificaction system, also designed by Goulding, et. al. (Go64).

The operation of the particle identifier is based upon the range-energy relationship for charged particles,

$$R = aE^b \qquad \text{Eq. 4.1}$$

where a is a constant for a given particle (i.e., a given mass and charge) and $b \approx 1.73$. For a particle that loses

ELECTRONICS

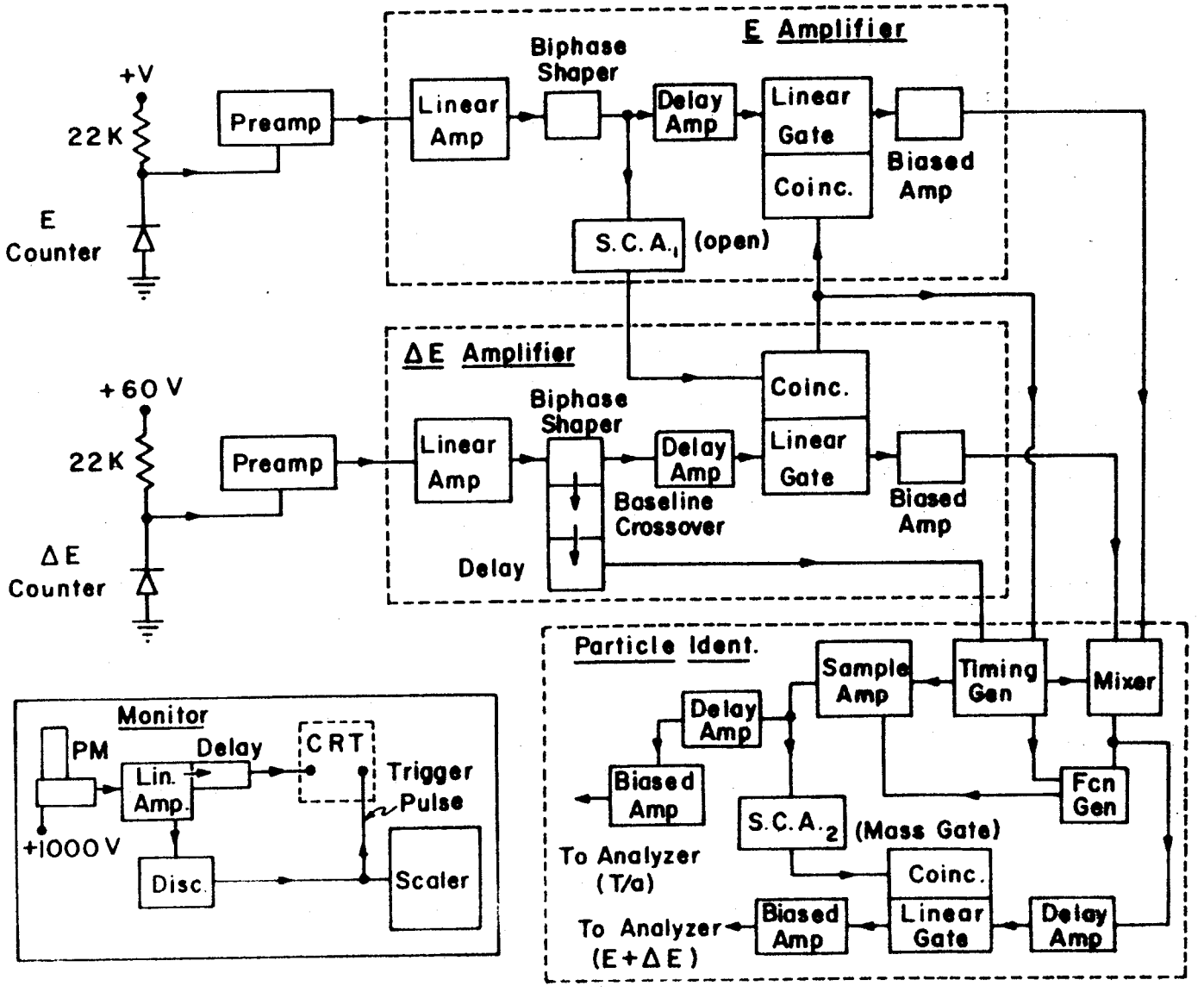

Figure 4.3. Block diagram of electronics used for (p,d) experiments. A [illegible] is also shown.

energy ΔE in the ΔE-counter and has total energy $E+\Delta E$, it can be shown that (Goo4):

$$T/a = (E+\Delta E)^{1.73} - (\Delta E)^{1.73}$$

Eq. 4.2

where T is the thickness of the ΔE counter. The quantity T/a, the value of which defines a particular particle, is determined by the identifier as explained below.

After the E and ΔE pulses were properly shaped in the amplifiers they were fed into the mixer unit of the particle identification system (Fig. 4.3). A coincidence between the detectors was also required within the amplifier systems to reduce the pulse rates entering the identifier. The height of the output pulse from the mixer is proportional to E for about the first 1.5 μsec and proportional to the total particle energy $(E+\Delta E)$ for an additional 1.5 μsec, i.e., the pulse has the shape of a step function. This signal from the mixer is fed into the function generator, where the entire wave form is raised to the 1.73 power. The sample amplifier picks out only the height of the step in this wave form, which is proportional to T/a in Eq. 4.2. The timing generator gets its start signal from the coincidence circuit in the amplifiers and stops with the baseline crossover of a doubly differentiated ΔE pulse. This provides the 1.5 μsec delay to produce the step in the wave form, while synchronizing signals are sent to the function generator and sample amplifier.

The "mass" output (T/a) of the identifier was fed into the 4096 channel analyzer and was displayed on an oscilloscope as the horizontal axis of a 64x64 array. The energy signal was displayed on the verical axis. This resulted in a contour plot of the counts per channel for each type of particle, with easily distinguishable groups of protons, deuterons, tritons, etc. An intense group appeared as a tail on the low mass side of the proton group. This corresponded to the elastically scattered 33.6 MeV protons, which were not stopped by the detectors. The deuteron selection was made by setting a gate on the T/a signal with a single channel analyzer (SCA_2 in Fig. 4.3) such that only pulses corresponding to the deuteron group were available to satisfy the coincidence requirement with the energy signal. In order to be certain that all of the deuterons were included in the gate, a very low background of protons and tritons was allowed in some cases. After the gate was set, a one dimensional deuteron energy spectrum was recorded and stored in each of four 1024 channel groups. The memory was then punched out on paper tape and printed on photographs by an optical readout system.

An overall electronic noise width of about 50 keV was attained with both detectors under bias, while the overall deuteron energy resolution was typically between 95 and 130 keV.

(b) Proton Monitor

A block diagram of the circuit for the proton monitor is also shown in Fig. 4.3. The pulses from the photo multiplier tube were preamplified and fed into a linear amplifier. A discriminator level was set such that only pulses corresponding to the elastically scattered protons reached the scaler to be recorded. This setting was made by displaying the amplifier output on an oscilloscope (CRT) which was triggered by the output of the discriminator. The ratio of the number of counts recorded (times the sine of the target angle) to the charge indicated by the current integrator remained constant to within a few percent for all data points.

4.2 Lithium-Drifted Silicon Detectors

Most of the lithium-drifted detectors used for these experiments were commercially purchased, although some of the preliminary data was taken with counters made in the laboratory. The method by which these detectors were constructed is discussed below.

A P-type silicon wafer of about 2 cm. diameter and 5 mm. thickness was lapped until smooth with 1000 grit lapping compound. Lithium was evaporated to one surface, and diffused into the surface by heating the wafer at a temperature of about 400°C. for approximately ten minutes. The wafer was then etched for about ten minutes in a solution of 3:1 HNO_3:HF, and rinsed thoroughly with

de-ionized water. The diffused lithium formed an N-type surface to which a positive potential of ~500 V. was applied. This caused lithium ions to drift through the crystal, forming an intrinsic region. With a power dissipation in the crystal of ~1 watt, about three weeks were required to drift to a depth of 3 mm. The depth was checked periodically with a staining solution that deposited copper only on the intrinsic region.

After the drifting process was completed, the wafer was cut into a shape similar to that shown in Fig. 4.4 (a). All surfaces were lapped and etched, and gold was evaporated to the surfaces indicated in the diagram. This provided a good electrical contact between the P-type and intrinsic regions. The crystal was then mounted in a capsule consisting of a brass case with a lucite filler as shown in Fig. 4.4(b). A spring-loaded electrical contact was inserted at the rear of the capsule, and a 0.00025 in. Mylar window was placed over the front aperture to keep the crystal free from dust. A copper block was designed to serve both as a mount for the capsule and a cooling device.

Although several of these counters failed to work satisfactorily, an overall energy resolution of 100 - 130 keV with elastically scattered 25 MeV protons was obtained with some of these devices. This resolution is comparable to that obtained under similar conditions

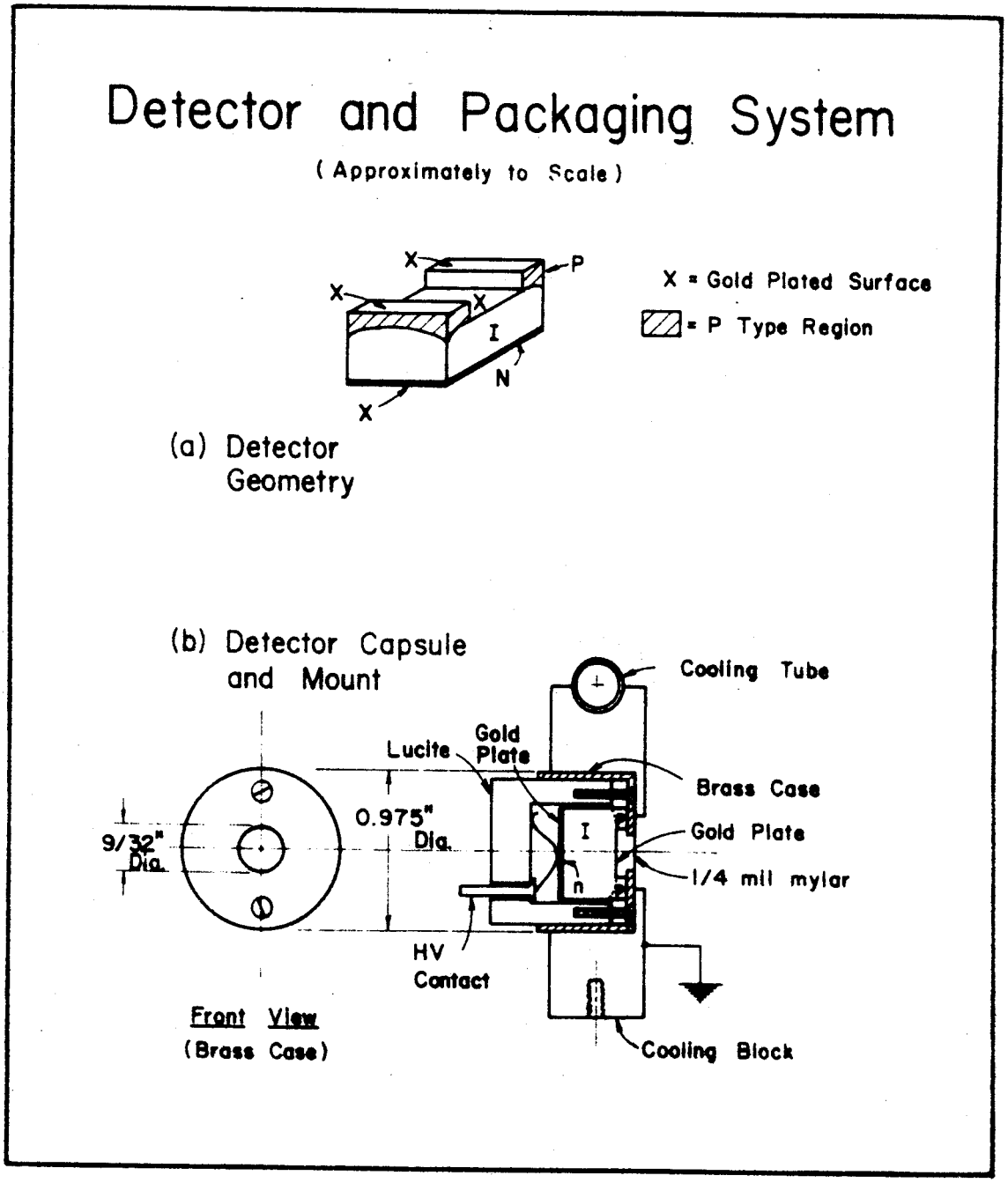

Figure 4.4. Geometry and package system for lithium-drifted silicon detectors.

with the commercially purchased counters. The major difficulty encountered was that the quality of performance decreased rapidly with time, even without large exposures to radiation.

4.3 Targets

The nuclear bombardment targets used for each experiment in this study are described below. Most of the nuclei have a high natural isotopic abundance, and were therefore fabricated in the laboratory from ordinary materials.

4.3.1 ^{24}Mg

The target used for the $^{24}Mg(p,d)^{23}Mg$ experiment was a commercially purchased rolled foil of 1.07 mg/cm^2 which was enriched to >99% ^{24}Mg. An oxygen contaminant corresponding to ~0.02 mg/cm^2 was observed in the (p,α) spectra (Chapter 5).

4.3.2 ^{28}Si

Chemically pure SiO of natural isotopic abundance (92.2% ^{28}Si) was evaporated from a tantalum boat to a 0.0001 in. nickel backing. The nickel was cooled during the evaporation by passing cold water through a copper block, which decreased the expansion of the nickel caused by heat from the boat. This therefore decreased the contraction of the nickel when the boat

was cooled, and prevented the extremely brittle SiO layer from cracking. A 2 cm^2 area of the nickel was then dissolved with HNO_3, exposing both sides of the SiO layer. A thickness of 0.68 ± 0.04 mg/cm^2 was obtained from the weights and areas of several pieces of the foil.

4.3.3 ^{32}S

A gas target containing H_2S was used to study the $^{32}S(p,d)^{31}S$ reaction. The gas cell consisted of a 5 in. diameter by 1 in. high copper cylinder having 0.001 in. Kapton walls. The cell was filled to a pressure of 45 cm Hg with natural H_2S (95.0% ^{32}S). This pressure corresponds to an equivalent target thickness of ~ 1 mg/cm^2 at a counter angle of 30° with the collimators described previously (Sec. 4.1.2). The pressure was monitored continuously during the experimental runs with a mercury manometer.

4.3.4 ^{36}Ar

A leak-proof cell was constructed for the purpose of making a permanent, isotopically enriched (>99%) ^{36}Ar gas target. A sketch of the cell is shown in Fig. 4.5. The frame was milled from a single piece of brass, and a Havar window of 10 mg/cm^2 thickness ($\approx$0.0005 in.) was attached with epoxy cement. A compound pressure gauge, which was readable to within an error $\pm$ 1 cm of Hg, was

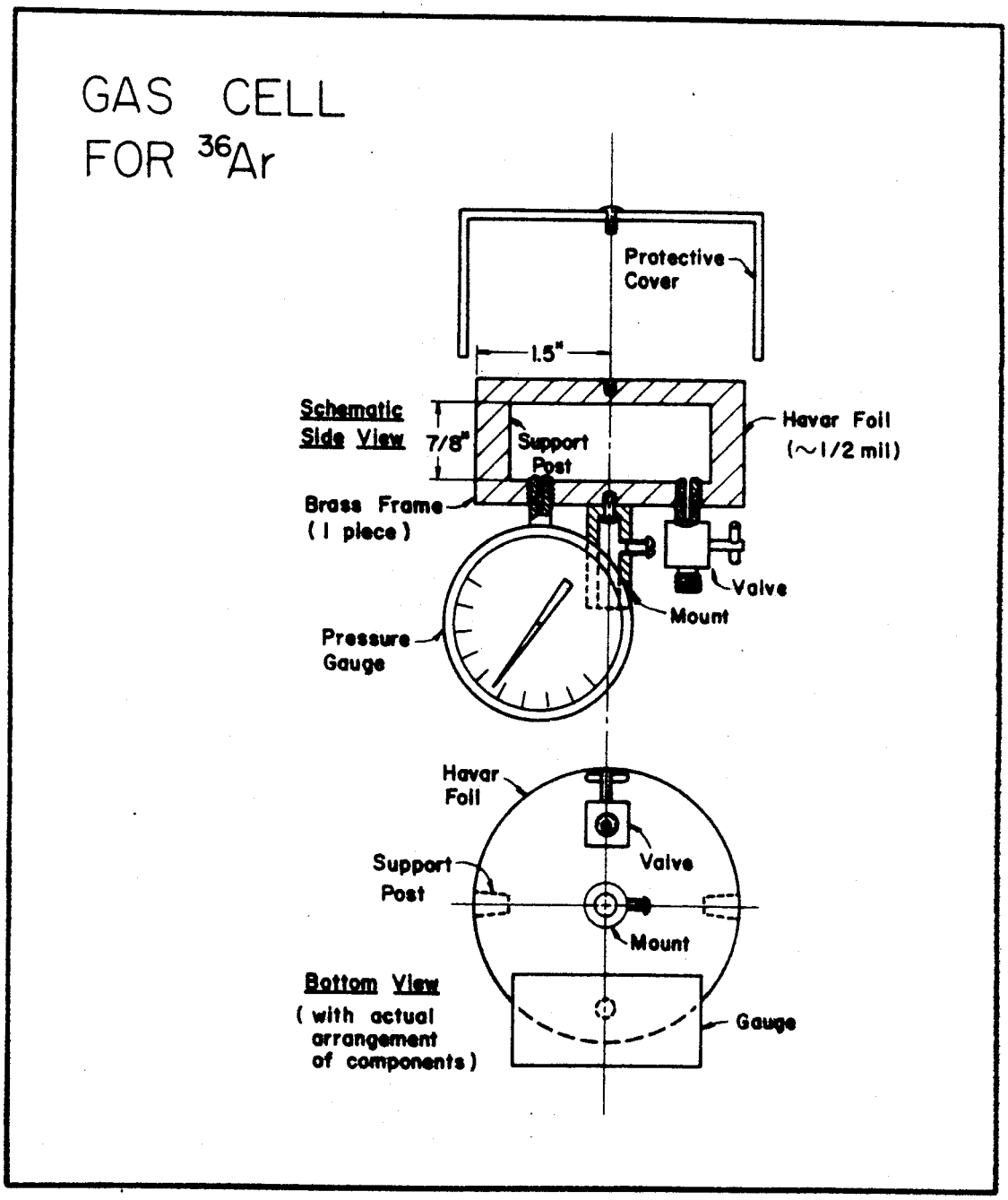

Figure 4.5. Schematic diagram of cell for ^{36}Ar gas target.

mounted on the bottom of the cell. A helium leak-tested Circle Seal valve was also included. The cell was filled with ^{36}Ar to a pressure of 45.1 ± 1.0 cm. of Hg at 25° C., which corresponded to a 1 mg/cm^2 thickness at a laboratory angle of 30°.

The strength of the 0.5 mil Havar window proved to be sufficient to withstand the above pressure and the flexing encountered when the cell was moved from atmospheric pressure to the evacuated scattering chamber and back again. The target has existed for a period of eight months with no detectable change in pressure.

4.3.5 ^{40}Ca

Natural calcium foils (97.0% ^{40}Ca) were used for the study of the $^{40}Ca(p,d)^{39}Ca$ reaction. These targets were made by evaporating calcium metal on a 0.001 in. tantalum foil. The heat from the evaporation process caused the tantalum to expand and, when cooled, the two foils separated due to their different coefficients of expansion. Calcium foils as thin as ~1 mg/cm^2 could be obtained with this method. Experimental data was obtained with foils of 1.10, 1.67 and 2.27 mg/cm^2 thickness.

4.4 Data Analysis

The deuteron energy spectra were stored in 1024-channel groups of the 4096 channel analyzer as mentioned earlier. After every four data points, the memory was

punched on paper tape and printed on photographs by the optical readout system. The information from the tape was then transferred to computer cards, and plots of the spectra and listings of the counts per channel were obtained through the use of a computer program. The photographic prints permitted some preliminary data analysis while the run was in progress, which helped to determine if the experiment was proceeding normally.

4.4.1 Determination of Excitation Energies

The ground state (p,d) reaction Q-values for the nuclei studied ranged from -14.95 MeV for the $^{28}Si(p,d)^{27}Si$ reaction to -12.86 MeV for the $^{32}S(p,d)^{31}S$ reaction. The Q-values for the $^{16}O(p,d)^{15}O$ and $^{12}C(p,d)^{11}C$ reactions are in the same region (-13.44 MeV and -16.50 MeV, respectively) and the ^{15}O and ^{11}C energy levels are well known (Lab1). A (p,d) spectrum from a Mylar target was therefore an ideal calibration device. Figure 4.6 shows a Mylar (p,d) spectrum obtained from a 0.00025 in. foil at a laboratory angle of 30°.

The deuteron energies for the levels excited in ^{15}O and ^{11}C in the (p,d) reaction were determined from relativistic kinematics by a computer program and plotted versus channel number. This effectively served to calibrate the electronics and counter system. All the points on this plot fell within $\pm$ 10 keV of a straight line, except that on some occasions the ^{15}O ground state appeared at a channel number which was too low. This was

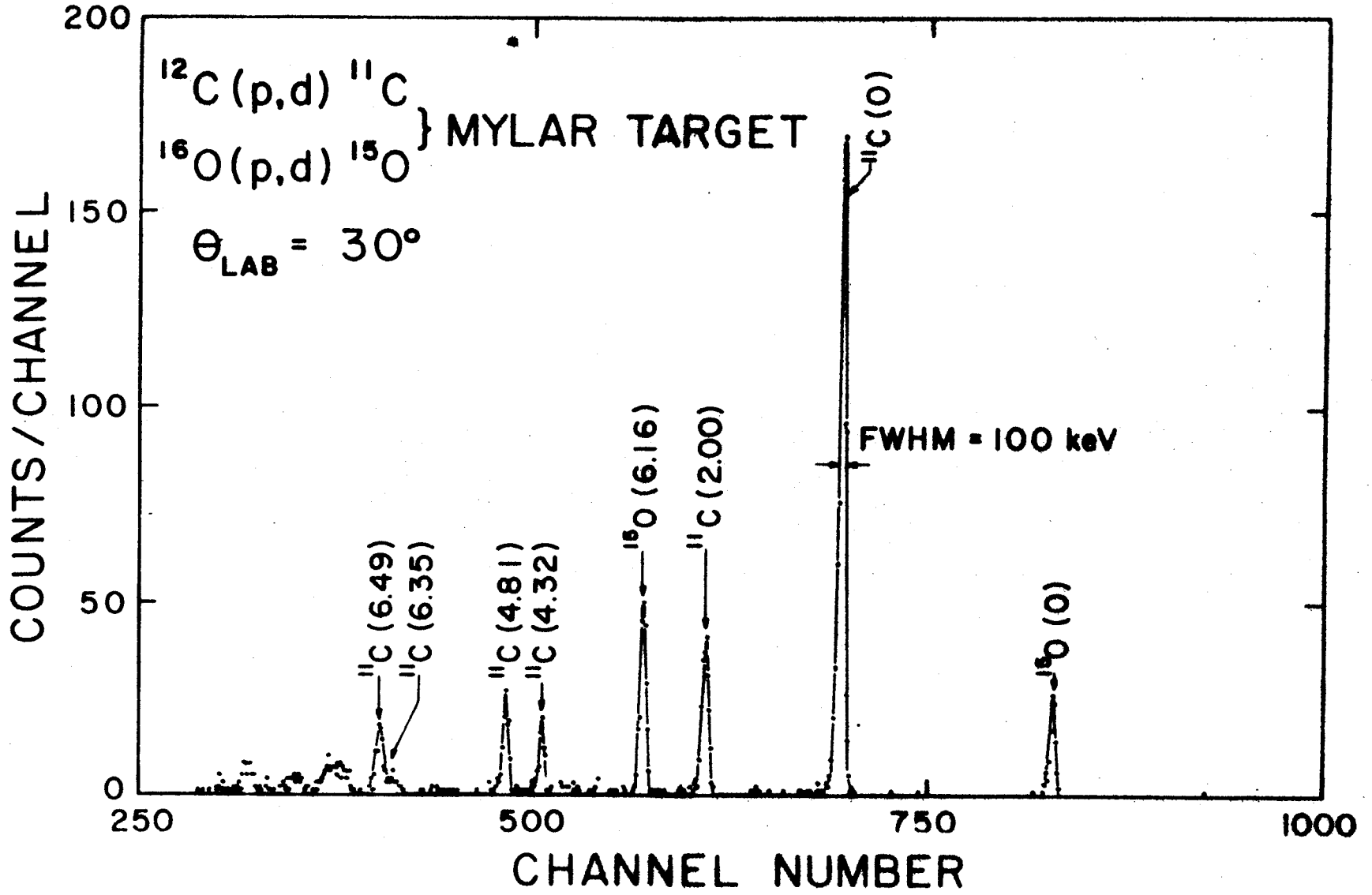

Figure 4.2. Deuteron calibration spectrum taken at 30° from a 0.00025" Mylar target. Levels excited in the $^{12}C(p,d)^{11}C$ and $^{16}O(p,d)^{15}O$ reaction are indicated.

possibly due to a lack of charge collection efficiency in the detector for the higher energy deuterons. In such cases, the deuteron energy from the ground state of the nucleus under study was plotted for several consecutive laboratory angles to determine the shape of the curve in this region. The deuteron energies corresponding to the excited levels in the residual nucleus were determined from the curve by their positions in the deuteron spectrum, and the excitation energies were obtained from a kinematics calculation.

4.4.2 Measurement of Differential Cross-Section

Deuteron energy spectra were obtained for laboratory angles from 10° to 155° for each residual nucleus. The total number of events (deuterons) in each peak was determined for each angle, and a reasonable background was subtracted. The differential cross-section was then calculated from the formula

$$\frac{d\sigma}{d\Omega} = \frac{N_1}{n N_2 \Delta\Omega} \times 10^{27} \frac{mb}{sr}$$

Eq. 4.3

where N_1 is the net number of counts in the peak, n is the number of target nuclei per cm^2, N_2 is the number of incident protons and $\Delta\Omega$ is the solid angle.

The quantity N_2 is calculated from the total charge obtained with the current integrator. For foil targets,

the solid angle is defined by the collimator directly in front of the counter telescope (C_2 in Fig. 4.2), and n is determined by the equivalent target thickness exposed to the beam (which depends on the target angle θ_T). In this case, Eq. 4.3 can be written in the form

$$\frac{d\sigma}{d\Omega} = \frac{C N_1 \sin\theta_T}{Q t \Delta\Omega}$$

Eq. 4.4

where Q is the integrated charge, t is the measured target thickness and C is a constant which depends on the chemical ratio of the element in the target and the isotopic abundance and mass of the nucleus.

The cross-section formula is somewhat different for the $^{36}Ar(p,\alpha)^{33}Ar$ and $^{32}S(p,\alpha)^{31}S$ experiments where gas targets were used. Two collimators were used in each of these cases to shield the detectors from the reaction products emitted from the windows of the cell. The expression for the cross-section can then be written as

$$\frac{d\sigma}{d\Omega} = \frac{N_1 H R \sin\theta}{n' N_2 \pi \left(\frac{A}{2}\right)^2 B \left[1.0 + \left(\frac{A}{4R}\cot\theta\right)^2 - \left(\frac{B}{H\sqrt{2}}\right)^2 - \frac{3}{32}A^2\left(\frac{1}{R^2}+\frac{1}{H^2}\right) + \left(\frac{B'}{4R}\right)^2\left(\frac{1}{\sin^2\theta} - \frac{3}{2}\right)\right]}$$

Eq. 4.5

where the quantity in brackets is part of the "G-factor" derived by Silverstein (Si59), which takes into account

the size of the beam (B') and certain geometrical factors. It was observed in this work that this quantity was unity to within 0.1% for $\theta_{LAB} \gtrsim 15^{\circ}$. In Eq. 4.5, A is the diameter of the rear collimator, B is the width of the front slit collimator, H is the distance between the collimators and R is the distance from the rear collimator to the center of the gas cell. n' corresponds to the number of nuclei per cm^3, and is obtained from the gas law for a given pressure and temperature. Neglecting the correction, Eq. 4.5 can be written

$$\frac{d\sigma}{d\Omega} = \frac{C' N_1 H R \sin\theta}{N_2 \pi \left(\frac{A}{2}\right)^2 B P}$$

Eq. 4.6

where C' depends on the temperature and the quantites mentioned for C in Eq. 4.4.

The differential cross-sections were calculated in the center of momentum system with the aid of computer programs. The G-factor correction was included in the calculations for the gas targets. The statistical error

$$e = \frac{\sqrt{N + N_B}}{\sqrt{N_1}} = \frac{\sqrt{N_1 + 2N_B}}{\sqrt{N_1}}$$

Eq. 4.7

was also calculated, where N_B is the number of background counts and N is the total number of counts in the peak.

4.5 Measurement of Beam Energy

The energy of the proton beam from the cyclotron was measured by the kinematic cross-over method (Bac4) and checked by an independent range-energy calibration. The cross-over measurement was made by bombarding a polystyrene (CH) target and observing the protons emitted from the $H(p,p)H$ and $^{12}C(p,p')^{12}C^*$ reactions with a counter telescope. The energies of the protons from both the 9.63 MeV level of ^{12}C and the p-p scattering were found to be equal to 22.68 MeV at a scattering angle of 33.9°. This cross-over was checked for both positive and negative scattering angles and agreement was found to within $\pm 0.1^\circ$. This corresponds to an error in the energy measurement of approximately ± 200 keV.

The range-energy method was devised to serve as a rapid check on the beam energy when setting up the cyclotron for a particular run. An aluminum absorber was carefully machined to a thickness of 1165.4 ± 0.3 mg/cm^2, which is just sufficient to stop a 30.130 MeV proton. For protons of energy greater than this, the energy of the proton after passing through the block (E_p'') is a rapidly varying function of the incident energy (E_p'), as shown in Fig. 4.7 (a). Therefore, a rough measurement of E_p'' gives a sensitive measure of the incident energy. This was done by placing the absorber in front of a 279μ surface barrier detector

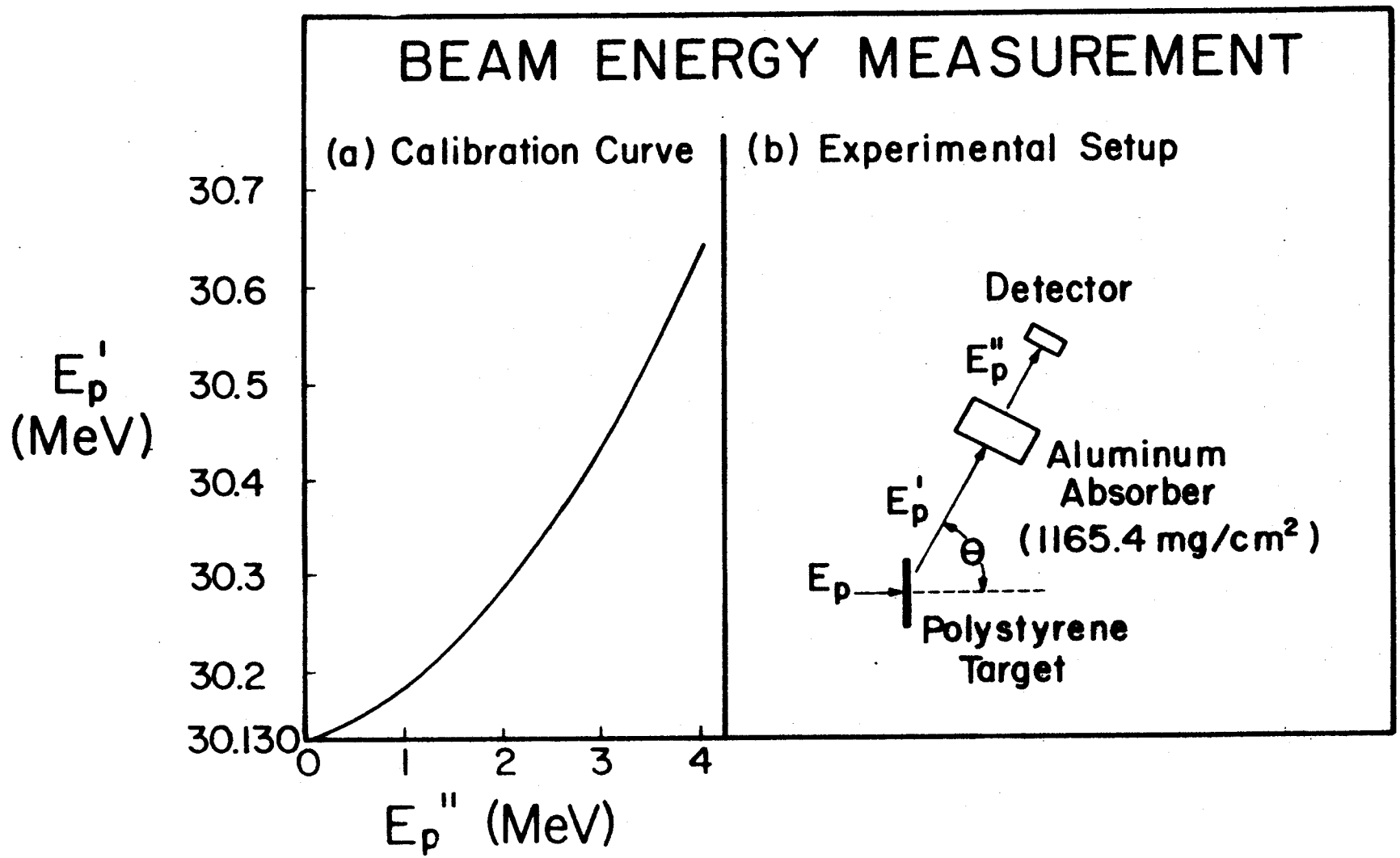

Fig. 4.7. Calibration curve and experimental arrangement for measuring beam energy by the [illegible] method.

on the counter arm in the scattering chamber and bombarding a polystyrene (CH) target with protons from the cyclotron (Fig. 4.7 (b)). The energy (E_p") of protons elastically scattered from ^{12}C was measured after they had passed through the absorber, and E_p' was determined from the calibration curve (Fig. 4.7 (a)). The energy of the incident beam (E_p) was then determined from the appropriate kinematics calculation for a given scattering angle. The results obtained from this measurement varied between 33.6 and 33.8 MeV for different experiments, with an estimated error of $\pm$ 200 keV for each measurement. The error was due mostly to uncertainties in the scattering angle ($\pm 0.5^{\circ}$) and the position of the broad peak in the E_p" spectrum. Due to the lower value of 33.4 MeV obtained by the cross-over method, the proton energy for all the experiments in this study is estimated to be 33.6 $\pm$ 0.2 MeV.

4.6 Estimate of Errors

4.6.1 Measurement of Energy Levels

The energies of the excited levels for the residual nuclei in the (p,d) reaction were measured by assuming the levels of ^{11}C and ^{15}O as standards as described earlier (Sec. 4.4.1). The only exception to this was in the measurement of the levels of ^{31}S, where the gas cell was filled with air to approximately the same pressure as the H_2S gas used in the experiment (45 cm of Hg),

and the calibration levels were those of ^{15}O and ^{13}N.

The position of the peak in the deuteron spectrum for the ground state of the nucleus being studied was used as a reference point for determining the excitation energies. This point was chosen at the same laboratory angle that the calibration spectrum was taken, with an estimated error of ± 5 keV. The error in the calibration curve due to the $\pm 0.5^{\circ}$ uncertainty in the counter angle was therefore negligible, since the spacing of levels in the deuteron spectrum is a very slowly varying function of angle. The uncertainty in the slope of the calibration curve is estimated to be 0.05 keV/channel, which corresponds to an error of about ± 10 keV at 4 MeV of excitation. The excitation energy for each level was determined from the spectra at a number of laboratory angles, and the average of these values corresponds to the result quoted in Chapter 5. The standard deviation for each set of measurements was determined from the formula

$$\sigma_E = \frac{1}{N-1}\sqrt{\sum_i (E_{x_i} - \bar{E}_x)^2}$$

Eq. 4.8

where the E_{x_i} are the measured values, $\bar{E}_x$ is the average value and N is the number of measurements. The quantity σ_E reflects the errors due to choosing the postions of the peaks in the spectra and the uncertainty in the laboratory angle for angles other than that corresponding to

the calibration spectrum.

The sources of error quoted in Chapter 5 for levels of ^{23}Mg, ^{31}S and ^{39}Ca can be summarized approximately as follows (typical case):

Slope of curve:	10 keV	(E_x 4 MeV)
G.S. Peak position:	5 keV	
σ_E:	10 keV	(5 measurements)

$$\varepsilon_{tot.} = \pm\sqrt{(10)^2+(5)^2+(10)^2} = \pm 15 \text{ keV} \sim \pm 20 \text{ keV}$$

Eq. 4.9

In the $^{28}Si(p,d)^{27}Si$ experiment, the constant presence of the well-known ^{15}O levels in the spectrum, in addition to the usual calibration spectrum from the Mylar target, enabled the measurement of ^{27}Si energy levels with an error of $\pm$ 10 keV in many cases. The positions of the ground and 6.16 MeV levels of ^{15}O were plotted versus deuteron energy for several laboratory angles. Since these two levels occur at opposite ends of the ^{27}Si deuteron spectrum, the slope in the region of interest was well determined in this way and the corresponding error in energy measurement was reduced. Also, the overall resolution of 95 - 100 keV permitted an accurate positioning of the levels at a relatively large number of angles, thereby decreasing the value of σ_E to $\sim$5 keV.

For all of the above experiments the target used in the investigation was similar enough to the respective calibration target so that no corrections were necessary

to account for differences in energy loss. Such was not the case for the $^{36}Ar(p,d)^{35}Ar$ experiment, however, where the calibration was made with a Mylar target and the ^{36}Ar target was the gas cell described previously (Sec. 4.3.4). Corrections were made for the proton and deuteron energy losses in the 10 mg/cm^2 Havar windows of the cell and in the gas itself. These corrections are slowly varying functions of particle energy and are summarized below:

33.6 MeV Proton loss in Havar	= 114 keV
33.5 MeV Proton loss in ^{36}Ar	= 44 keV
Deuteron loss in ^{36}Ar	= 110 - 148 keV
Deuteron loss in Havar	= 287 - 380 keV

Here, the corrections corresponding to the ^{35}Ar ground state and 6.82 MeV level are shown for the deuterons. Each correction is estimated to be accurate within $\pm$5 keV, with some of the error due to the $\pm$200 keV uncertainty in bombarding energy. This results in another $\pm$10 keV error to be added in quadrature to $e_{tot.}$ in Eq. 4.9.

4.6.2 Energy Resolution

The overall deuteron energy resolution varied between 95 and 130 keV during this investigation. The major contributors to the energy width are listed below for the $^{28}Si(p,d)^{27}Si$ reaction:

Electronic and counter noise	50 keV
Target thickness	25 keV (0.88 mg/cm^2 SiO)

Kinematic broadening 21 keV ($\Delta\theta = 0.92^\circ$)

Other 74 keV

$$\sqrt{(50)^2 + (25)^2 + (21)^2 + (74)^2} = 95 \text{ keV}$$

Eq. 4.10

The electronic noise and kinematic broadening contributed similarly to the energy spread in the other foil targets, while an additonal width due to straggling in the gas and windows of the gas cells should be added in quadrature for the $^{32}S(p,d)^{31}S$ and $^{36}Ar(p,d)^{35}Ar$ experiments. These values are approximately 25 keV and 50 keV for ^{32}S and ^{36}Ar, respectively. The quantity labelled "Other" in Eq. 4.10 includes the energy spread involved in the charge collection in the detectors and the resolution of the incident beam, as well as other unknown sources.

4.6.3 Cross-Section Normalization

The errors involved in determining the absolute differential cross-sections for the foil targets are estimated as shown below:

Target thickness measurement:	2 - 5%
Measurement of solid angle:	2%
Current integration:	1%
Target angle error ($\pm 2^\circ$):	2%
Counter angle error ($\pm 0.5^\circ$):	3%

This results in errors of approximately ±5%, ±7% and

$\pm$5% for the normalization of the data from the ^{24}Mg, SiO and Ca targets, respectively, in addition to the statistical errors shown on the curves in Chapter 5. The estimated errors in target thickness are assumed to be mostly due to nonuniformities in the targets. The error due to uncertainty in the counter angle arises from the slope of the differential cross-section versus angle, and the above number corresponds to a typical case for an ℓ_n=2 angular distribution.

For the experiments involving gas targets, the errors in target thickness depend on the uncertainties in measurement of the pressure and temperature of the gas in the cell and the counter angle. These errors are summarized below for the ^{36}Ar and H_2S gas targets at $\theta_{LAB}=30 \pm 0.5^{\circ}$:

	H_2S	^{36}Ar
Temperature:	~1%	~1%
Pressure:	1%	2%
Counter Angle (target thickness):	2%	2%
Measurement of solid angle:	3%	3%
Current integration:	1%	1%
Counter angle (slope of cross-section):	3%	3%

The result is an error of approximately $\pm$ 5% for both the $^{32}S(p,d)^{31}S$ and $^{36}Ar(p,d)^{35}Ar$ reactions, again excluding the statistical error.

Chapter 5

Experimental Results

In this chapter the deuteron spectra and angular distributions obtained from the (p,d) reactions on ^{24}Mg, ^{28}Si, ^{16}O, ^{32}S, ^{36}Ar and ^{40}Ca are discussed. Since all of these targets have $J^{\pi}=0^{+}$ in the ground state, the spin and parity of the final state is always equal to that of the picked up neutron. The curves on the angular distributions represent only the general trend of the data, while the error bars refer only to statistics. Properties of the $\ell_n=2$ J-dependence are also described.

Since evidence exists that most of these nuclei are deformed (St65), a Nilsson diagram (Ni55) showing single particle energies in a deformed potential well is presented in Fig. 5.1. This model was discussed in more detail in Chapter 2.

5.1 $^{24}Mg(p,d)^{23}Mg$

5.1.1 Results and Interpretation

Typical deuteron spectra from the (p,d) reaction on an enriched (>99%) ^{24}Mg target are shown in Figs. 5.2 and 5.3 for laboratory angles 30° and 90°, respectively. Several strongly excited levels of ^{23}Mg and levels of ^{15}O at 0.00 and 6.16 MeV of

NILSSON SINGLE PARTICLE LEVELS

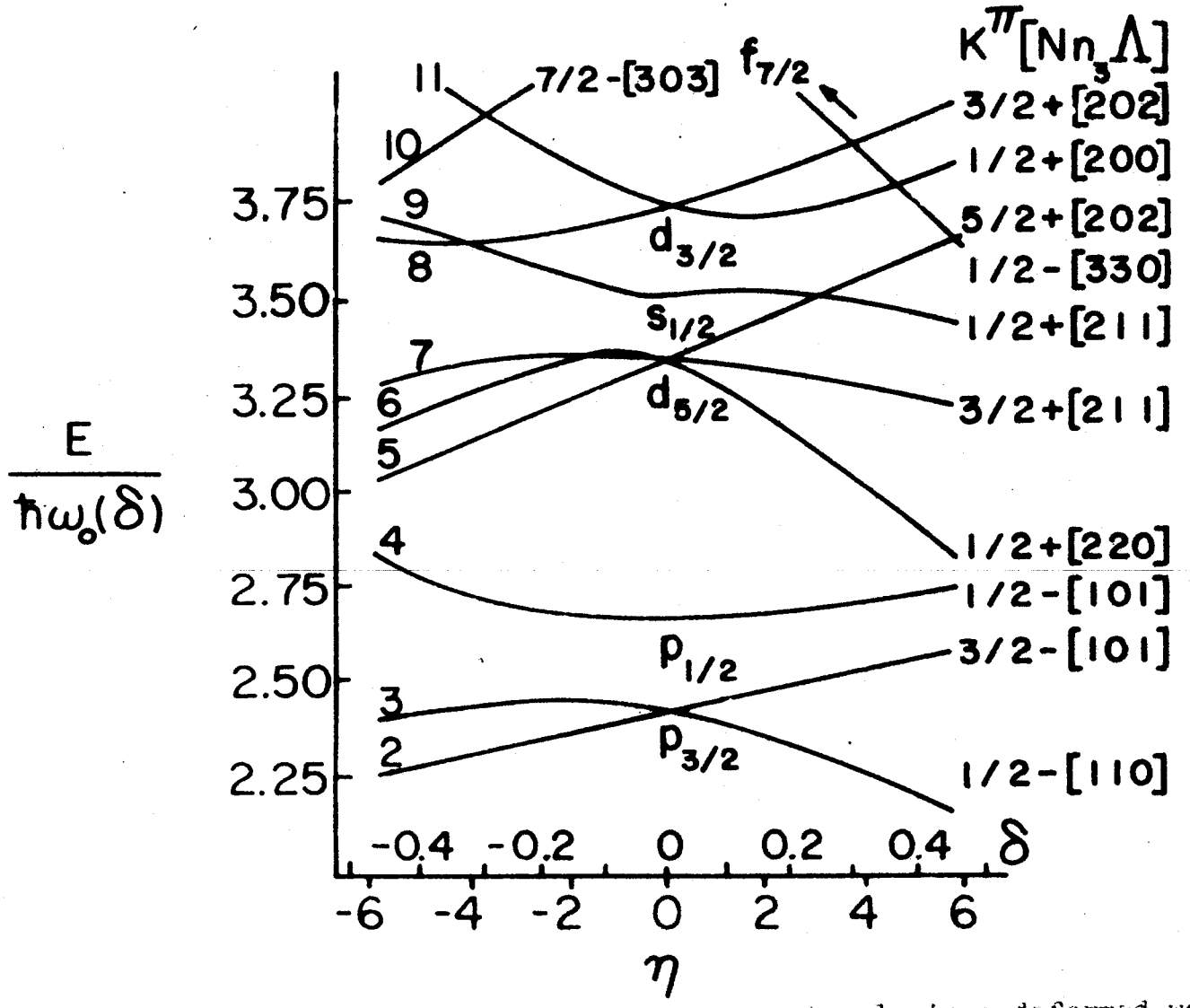

Fig. 1. Nilsson diagram of single particle levels in a deformed well (N155). Each level is doubly degenerate for protons and neutrons; the first K=1/2 ($1s_{1/2}$) level is [illegible].

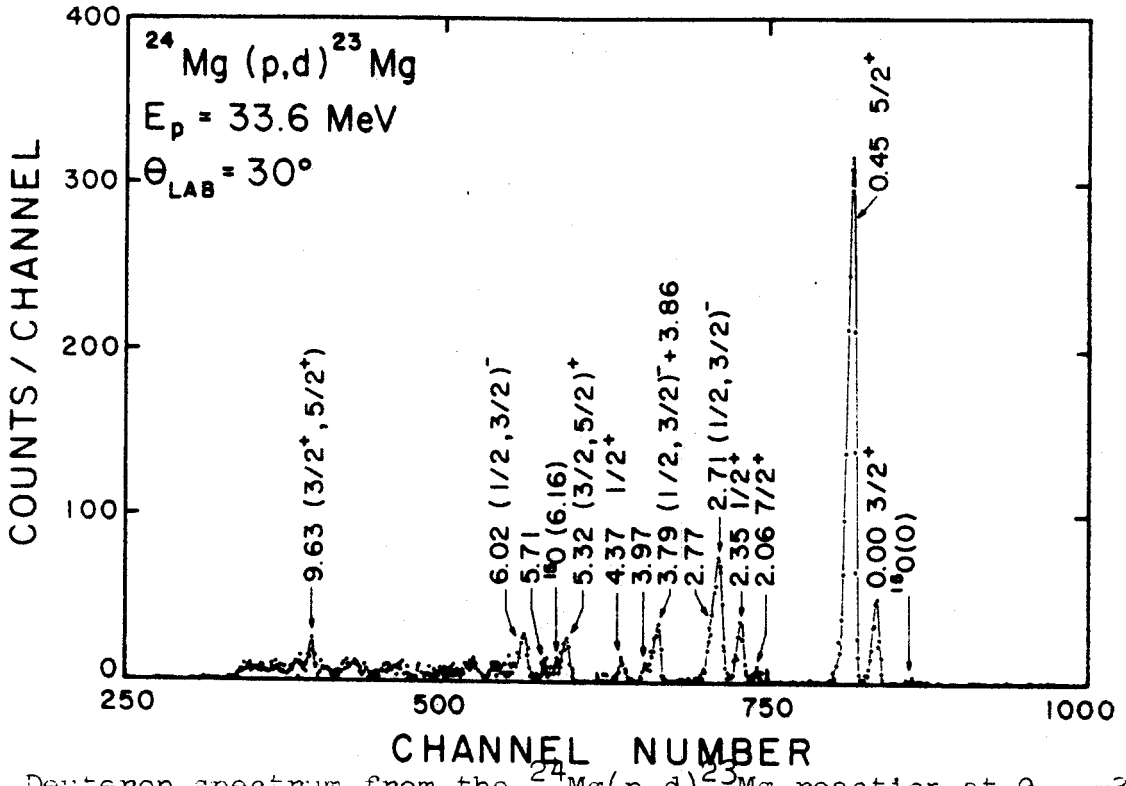

5.2. Deuteron spectrum from the ^{24}Mg(p,d)^{23}Mg reaction at θ_{LAB}=30°. An oxygen contaminant of ≲2% is observed.

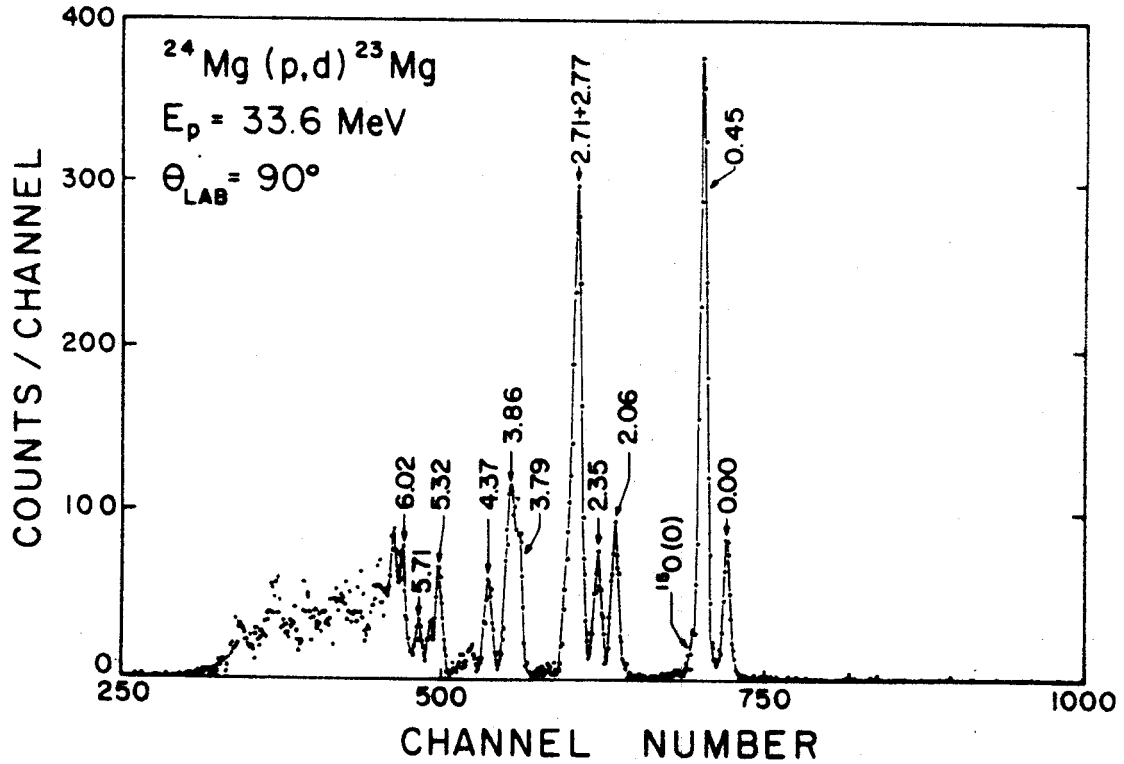

5.3. Deuteron spectrum from the ^{24}Mg(p,d)^{23}Mg reaction at θ_{LAB}=90°.

excitation were observed. The strengths of the ^{15}O excitations together with the measurement of the absolute differential cross-section (Sec. 5.3) indicate an oxygen contaminant of $\lesssim 2\%$. Corrections were made in the cross-sections for ^{23}Mg levels at those angles where they were not resolved from the oxygen peaks. An overall energy resolution of 115 - 120 keV was obtained. This was insufficient to resolve the 2.71 and 2.77 MeV levels of ^{23}Mg; a similar situation exists for the 3.79 and 3.86 MeV levels. Consequently, the 2.71 and 3.79 MeV levels were analyzed by assuming their peak shapes were the same as the well resolved 0.45 MeV level.

Deuteron angular distributions for ten of the excited levels were measured for laboratory angles from 10° to 155°. The distributions for levels of ^{23}Mg at 0.00, 0.45, and 5.32 MeV shown in Fig. 5.4 indicate a neutron pick-up from the 1d shell ($\ell_n=2$). The angular distribution from a level at 9.63 MeV is also shown, and corresponds to an ℓ_n of either 1 or 2. The position of the forward maximum seems to favor slightly the $\ell_n=2$ assignment, although the statistical errors are quite large. These results are consistent with spin and parity assignments $J^{\pi}=3/2^+$, $5/2^+$, $(3/2, 5/2)^+$ and $(3/2^+, 5/2^+)$ for excitation energies 0.00, 0.45, 5.32 and 9.63 MeV, respectively. The first two assignments

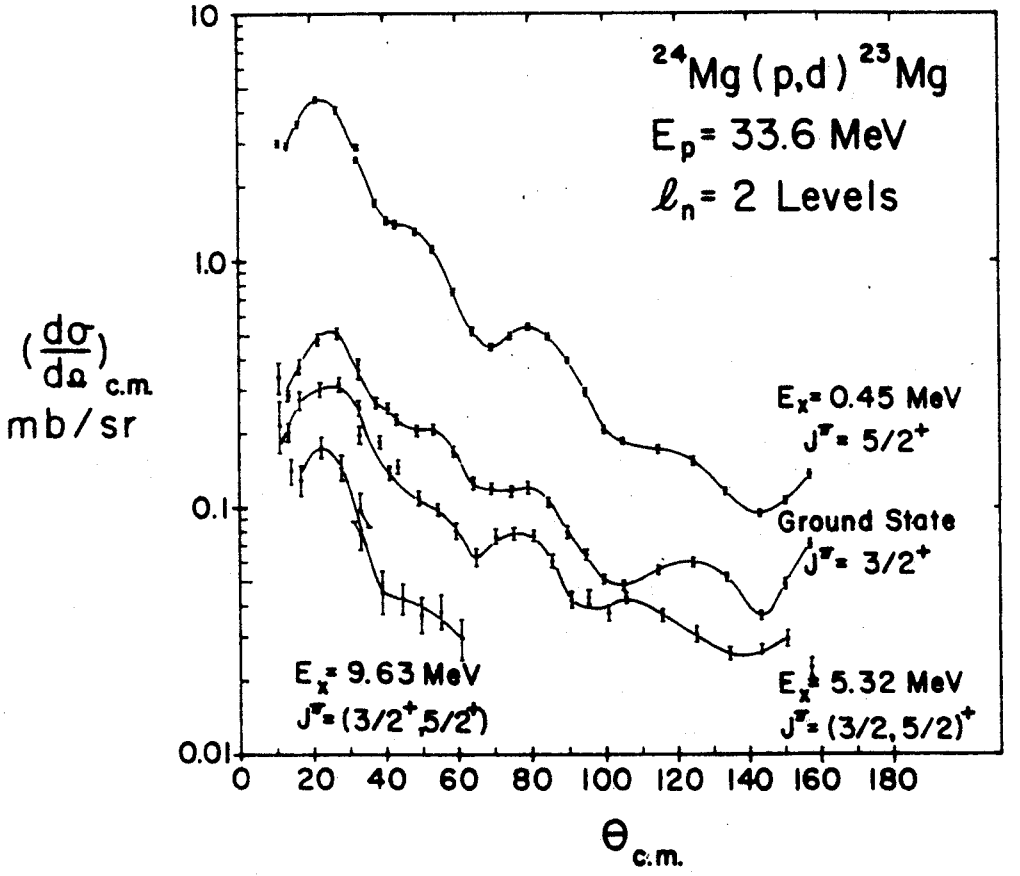

Figure 5.4. Deuteron angular distributions for the 0.00, 0.45, 5.32 and 9.63 MeV levels of ^{23}Mg from the ^{24}Mg(p,d)^{23}Mg reaction.

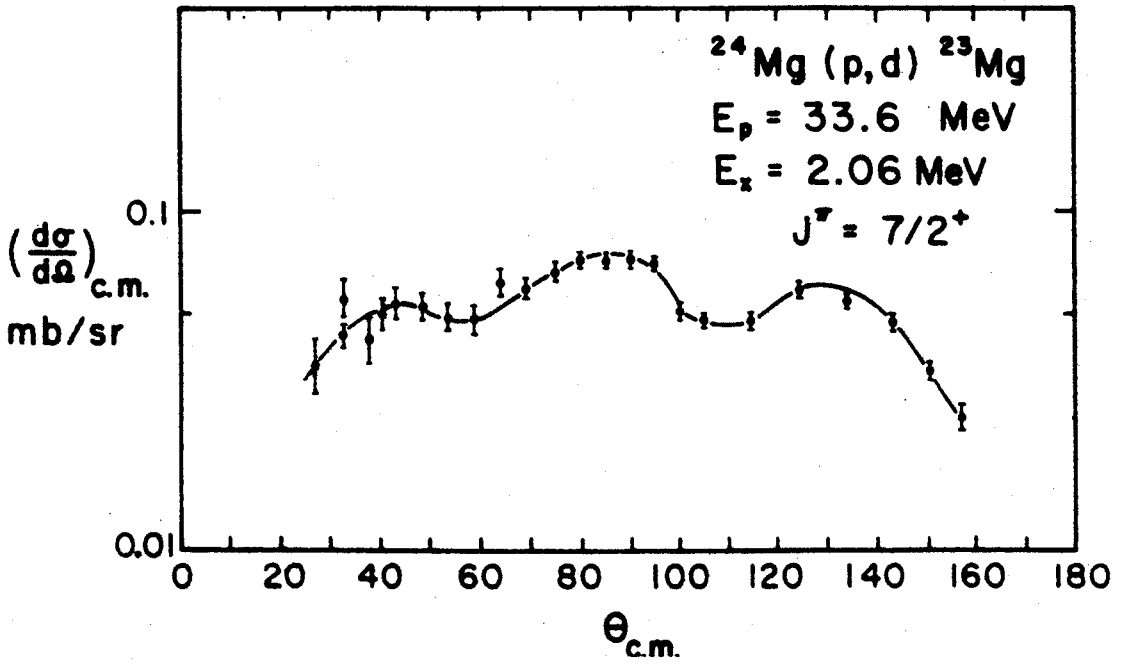

Figure 5.5. Deuteron angular distribution for the 2.06 MeV level of ^{23}Mg from the ^{24}Mg(p,d)^{23}Mg reaction.

correspond to well known mirror levels in ^{23}Na, and have been confirmed recently by ^{24}Mg(^{3}He,α)^{23}Mg experiments (Jo66, Du66). They are interpreted (Du66) as corresponding to members of a rotational band based on a K=3/2 hole in Nilsson orbit 7 (See Fig. 5.1). This seems reasonable since the nuclear deformations in this mass region are assumed to be prolate ($\delta > 0$) (Pr62). The third member of this band should be the $7/2^+$ level at 2.06 MeV. The angular distribution for this level (Fig. 5.5) is relatively isotropic, which is probably due to a complicated reaction mechanism involving an intermediate nuclear state. This is to be expected since, when the target ground state has $J^\pi=0^+$, the only mechanism by which a $7/2^+$ level can be excited in a direct process is by the removal of a $g_{7/2}$ neutron. This admixture is expected to be small in light nuclei.

The levels at 2.35 and 4.37 MeV are excited by an $\ell_n=0$ pick-up (Fig. 5.6) and therefore have $J^\pi=1/2^+$. Levels in ^{23}Na with the same J have been observed at similar excitation energies (Ha64). The 2.35 MeV level is assumed to be excited mainly by a pick-up from Nilsson orbit 6 (Du66), and should be the only $1/2^+$ level excited in ^{23}Mg. The excitation of both the 2.35 and 4.37 MeV levels is therefore evidence for configuration mixing between Nilsson orbits.

The angular distributions obtained for the 2.71,

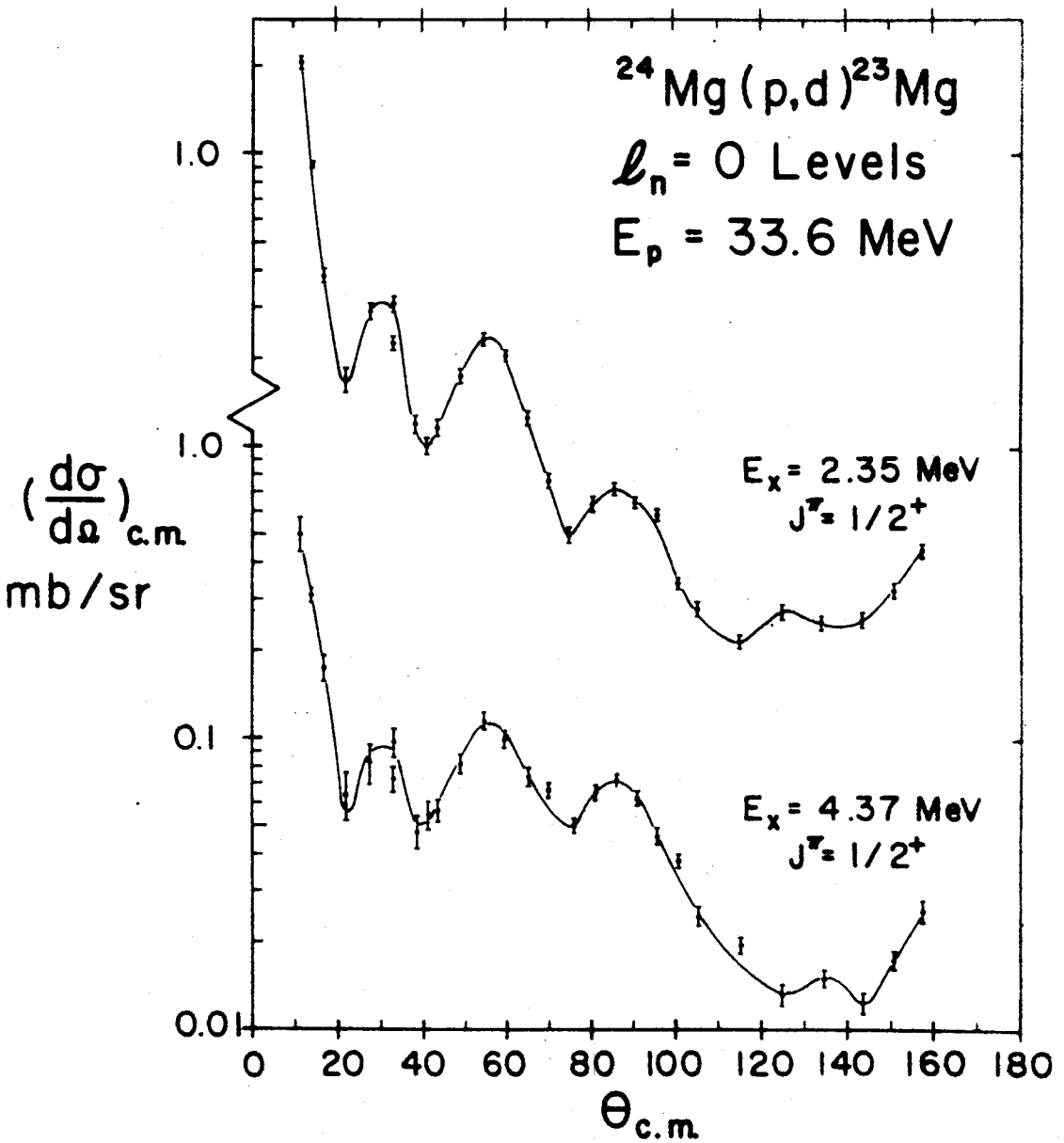

Figure 5.6. Deuteron angular distributions for the 2.35 and 4.37 MeV levels of ^{23}Mg from the ^{24}Mg(p,d)^{23}Mg reaction.

3.79 and 6.02 MeV levels in ^{23}Mg have shapes corresponding to ℓ_n=1 pick-ups, which indicates that these levels have negative parity with J=1/2 or 3/2 (Fig. 5.7). The spin and parity of the 2.64 MeV level of ^{23}Na, which should be the mirror to the 2.71 MeV level of ^{23}Mg has been previously reported as $1/2^+$ (Br62). DuBois et. al. (Du67), who have recently studied the ^{24}Mg(^{3}He,α)^{23}Mg reaction, have confirmed the assignments given here for the 3.79 and 6.02 MeV levels. However, they conclude that the excitation of the 2.77 MeV level is due to an ℓ_n=1 pick-up, while the level at 2.71 MeV is possibly excited by an ℓ_n=3 transfer. The energies measured for these two levels in the present work are estimated to be in error by about $\pm$ 20 keV, and it appears from the deuteron spectrum (Fig. 5.2) that the most strongly excited level in the doublet corresponds to the lowest excitation energy. It was this portion of the composite peak that was analyzed by the method discussed earlier to obtain the angular distribution shown in Fig. 5.7.

The origin of the picked up neutrons in the excitation of the ℓ_n=1 levels is ambiguous. It is not clear, even from the spectroscopic strengths (Chapter 6), whether these levels are excited by a pick-up from the 1p shell, the 2p shell or both. This ambiguity is discussed further in Sec. 5.2.1 (b), as ℓ_n=1 levels of relatively low excitation energy are also excited in the ^{28}Si(p,d)^{27}Si reaction.

5.1.2 J-dependence

J-dependence for the $^{24}Mg(p,d)^{23}Mg$ reaction is observed in the angular distributions for the ground ($3/2^+$) and 0.45 MeV levels of ^{23}Mg (Fig. 5.4). The $5/2^+$ distribution has a steeper overall slope versus angle than the $3/2^+$ distribution, while the forward maximum for J=5/2 seems to occur at a slightly smaller angle than for J=3/2. Although the J-dependence here seems relatively weak, the effects are generally opposite to those observed for most of the other nuclei investigated in this study.

5.1.3 Summary

The results obtained from previous work on the A=23 mirror nuclei are summarized in the level diagram (a) of Fig. 5.8 (Br62, La65), while the results from this experiment are shown in Fig. 5.8 (b). Errors in the energy measurements are indicated wherever the agreement with Fig. 5.8 (a) is not exact. In addition to the levels shown here, several others have been observed recently in $^{24}Mg(^3He,\alpha)^{23}Mg$ experiments (Jo66, Du66, Ha67). The energies for four of the levels are in agreement with those found by Ref. Ha67 at 4.362, 5.286, 5.7 (doublet) and 5.986 MeV, respectively.

In general, there appears to be extensive configuration mixing of shell model states, and even some

mixing of Nilsson orbits, in the ground state wave function of ^{24}Mg. This is not surprising, since the deformation of ^{24}Mg is believed to be large (St65). The level order of ^{23}Mg, at least for low excitations, seems to be consistent with a rotational model and a prolate deformation.

5.2 ^{28}Si(p,d)^{27}Si

5.2.1 Results and Interpretation

Typical deuteron spectra from the (p,d) reaction on the SiO target are shown in Figs. 5.9 and 5.10 for laboratory angles 25° and 80°, respectively. Several excited levels of ^{27}Si and ^{15}O were observed with an overall energy resolution of 95 - 100 keV. For emission angles $\theta_{LAB} \gtrsim 75°$ the deuterons from the ^{15}O ground state had energy less than or equal to those from the ^{27}Si ground state. The differential cross-sections for the ^{27}Si levels were obtained at the kinematic cross-over angles by interpolating both the oxygen and silicon angular distributions.

(a) Positive Parity Levels

Six deuteron groups from the ^{28}Si(p,d)^{27}Si reaction are observed to arise mainly from an ℓ_n=2 neutron pick-up (Figs. 5.11 and 5.12). Spin and parity assignments of $5/2^+$, $3/2^+$ and $5/2^+$ for excitation energies 0.00, 0.952 and 2.647 MeV, respectively, are

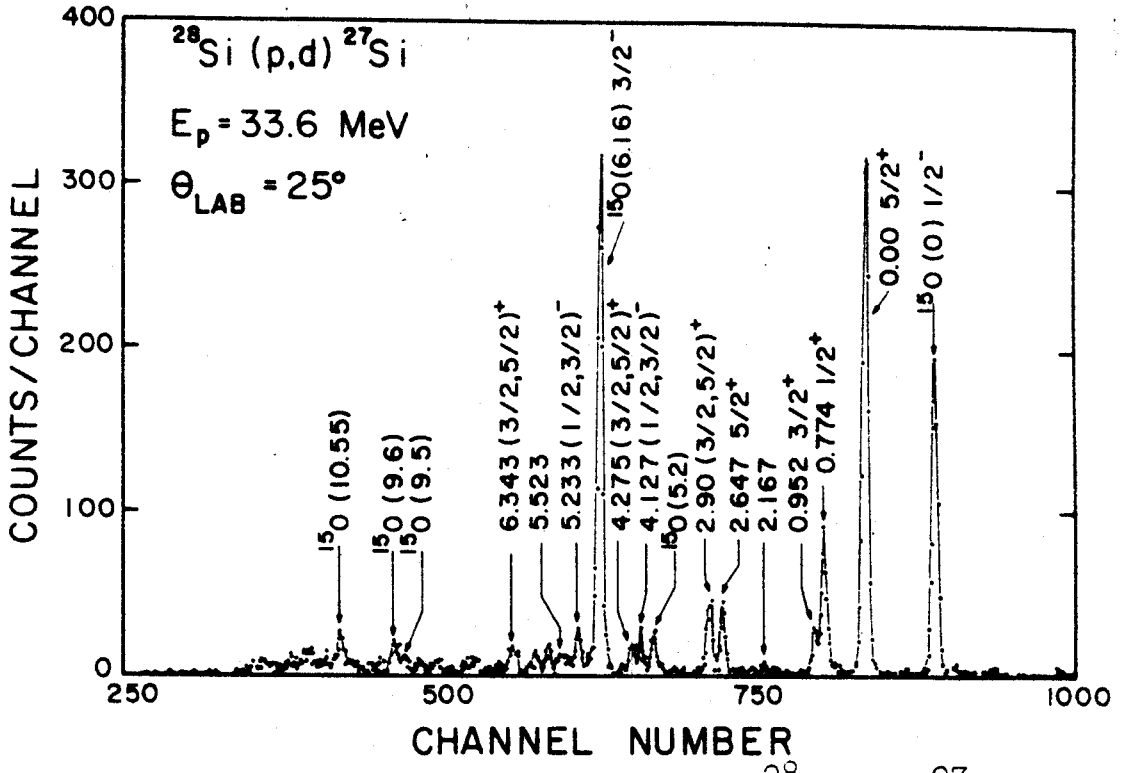

Figure 5.9. Deuteron spectrum from the ^{28}Si(p,d)^{27}Si reaction at θ_{LAB}=25°. A SiO target was used, and levels of ^{15}O and ^{27}Si are indicated.

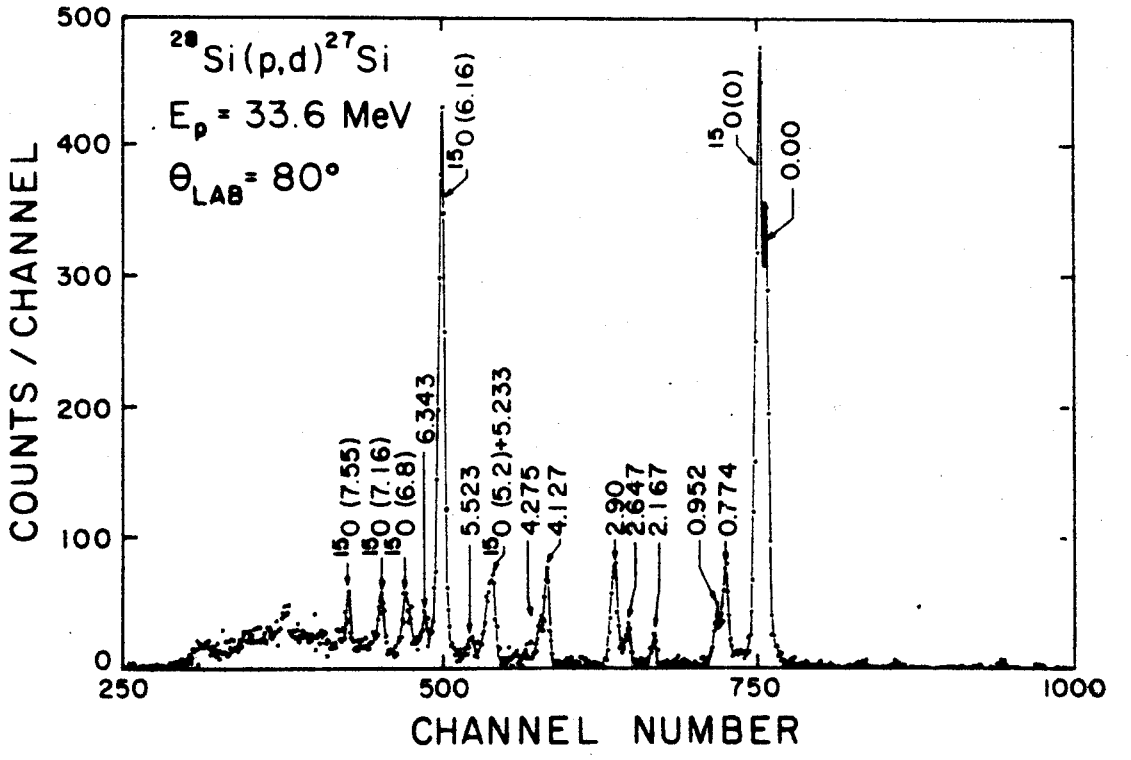

Figure 5.10. Deuteron spectrum from the ^{28}Si(p,d)^{27}Si reaction at θ_{LAB}=80° (SiO target).

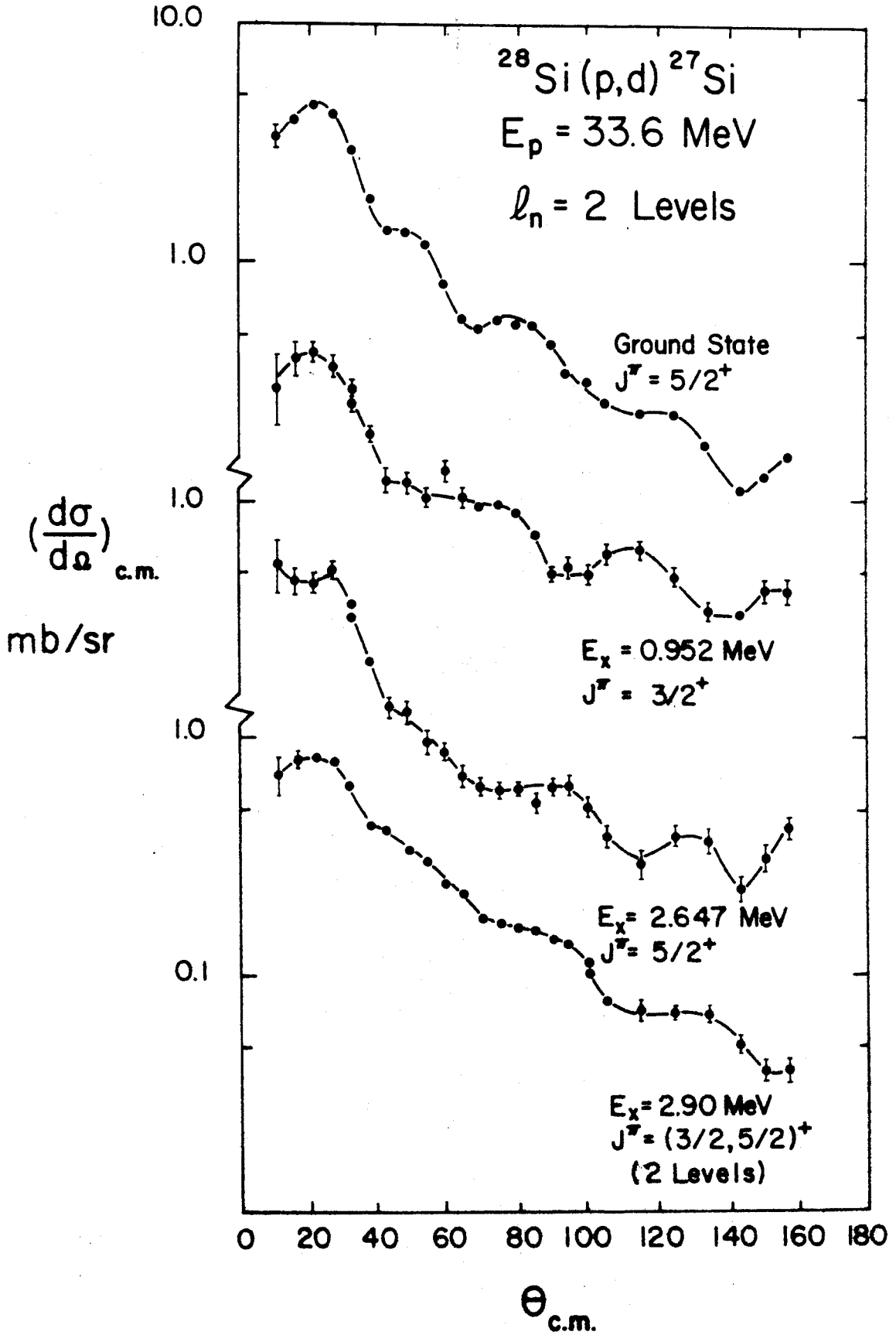

Figure 5.11. Deuteron angular distributions for the 0.00, 0.952,

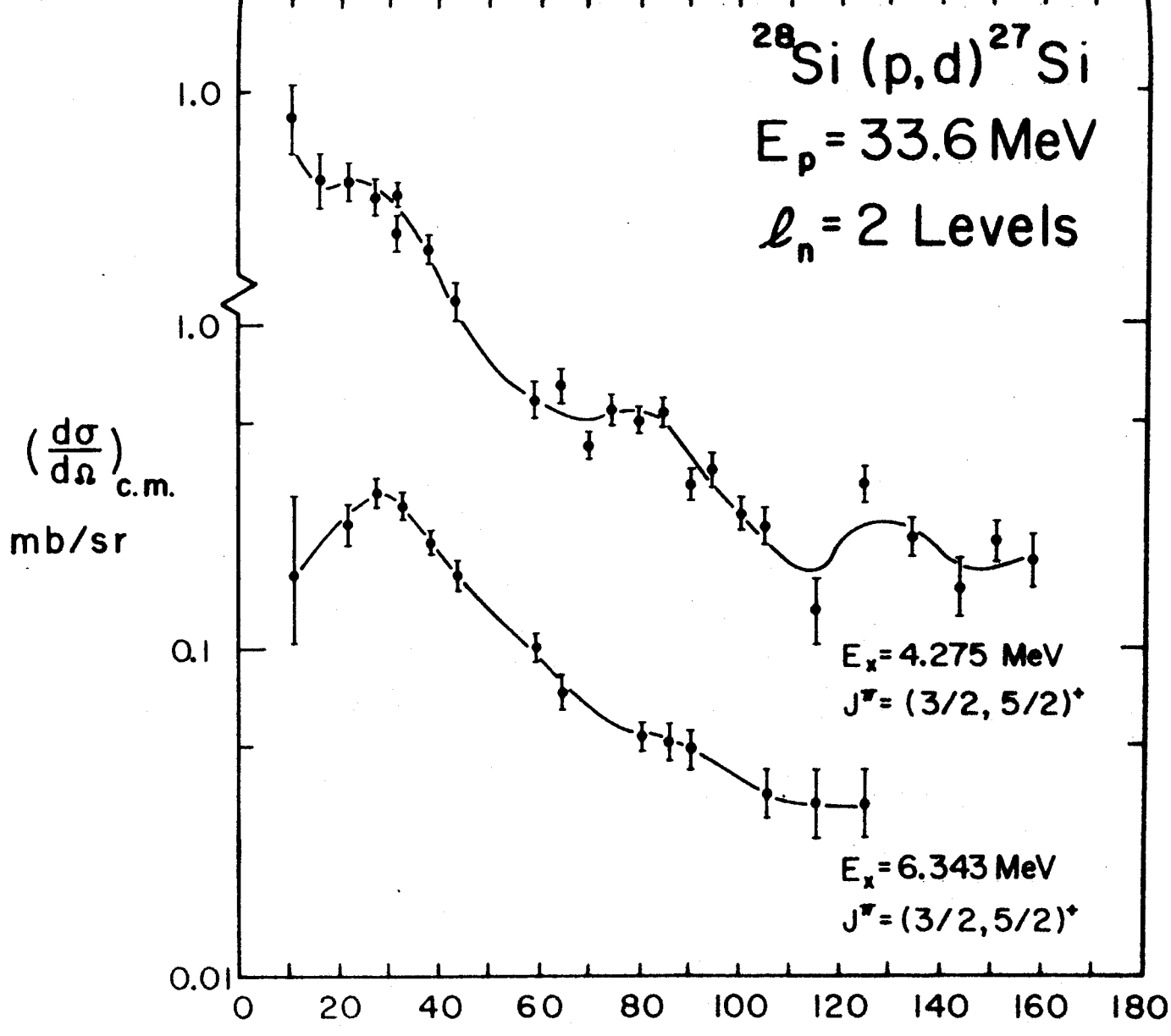

... for distributions for the 4.275 and 6.343 MeV levels of ^{27}Si ... ^{28}Si(p,d)^{27}Si reaction.

obtained from corresponding levels of known spin and parity in the ^{27}Al mirror nucleus (En62). The 2.90 MeV excitation is known to consist of two levels which are separated by about 40 keV, one of which has been assigned $J^{\pi}=3/2^{+}$ (En62). Since the FWHM of this group in the spectrum (Fig. 5.9) is about 40 keV larger than that for the other levels, it appears that both levels may be strongly excited. Therefore, since the sum of their angular distributions retains the $\ell_n=2$ shape with no ambiguity, the assignment $J^{\pi}=(3/2, 5/2)^{+}$ may be reasonable for both levels, unless one of them is not excited by a direct process.* The angular distribution for the 4.275 MeV level (Fig. 5.12) indicates some admixtures from other unresolved levels having $\ell_n\neq 2$, but the main contribution appears to be from the 1d shell, resulting in an $(3/2, 5/2)^{+}$ assignment for this level and the level at 6.343 MeV excitation. This assignment has also been obtained for a level in ^{27}Al at 4.403 MeV from the ^{28}Si(d, ^{3}He)^{27}Al reaction (Wi67).

The excitation of the 0.774 MeV level is evidence for a $2s_{1/2}$ admixture in the ^{28}Si ground state. The $\ell_n=0$ angular distribution for this level is shown in Fig. 5.13, and the $1/2^{+}$ assignment is consistent with

* A recent ^{28}Si(d, ^{3}He)^{27}Al experiment where the mirror of this doublet is resolved has indicated that the angular distribution for one of the levels is relatively isotropic (Go67).

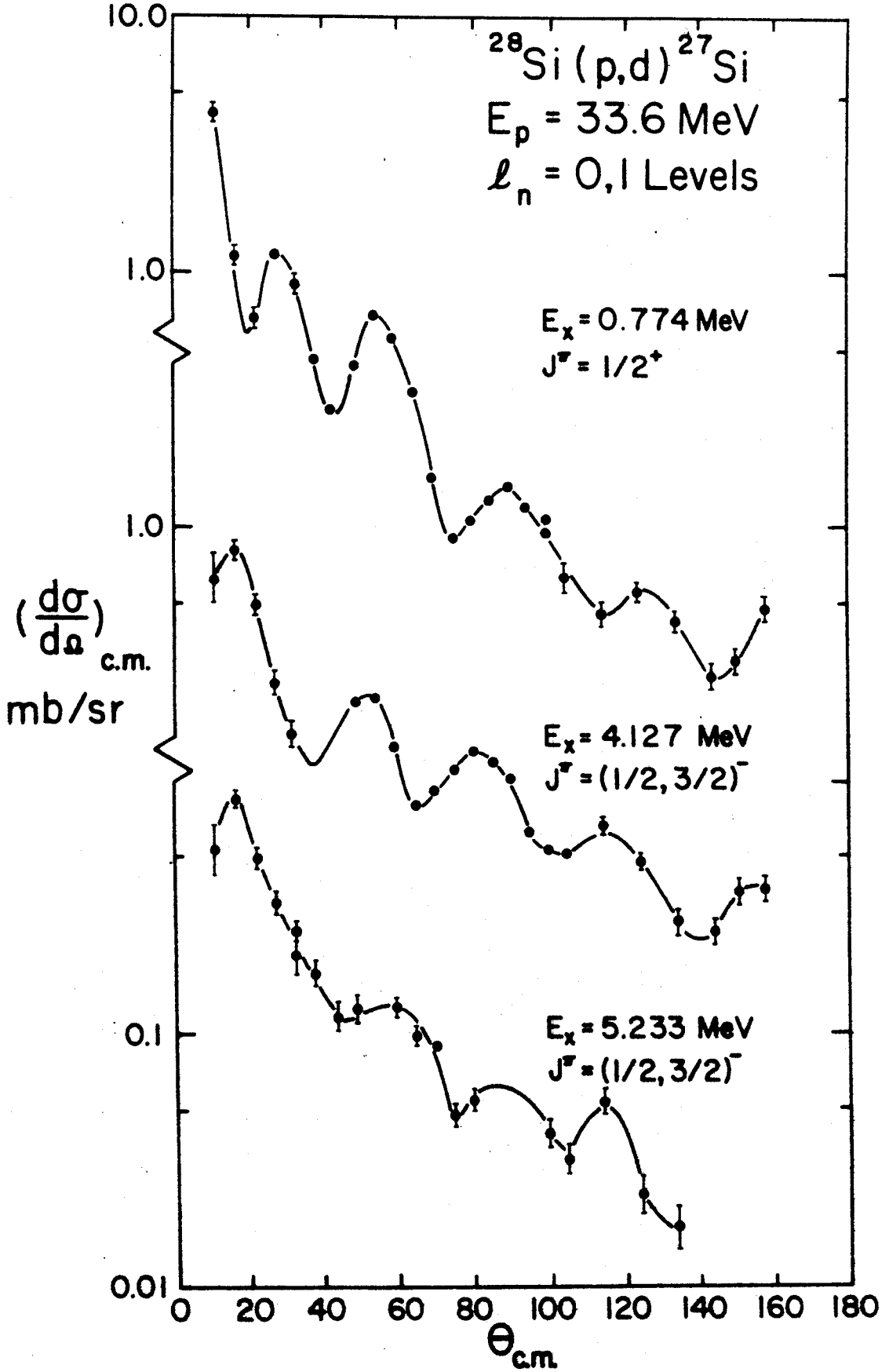

Figure 5.13. Deuteron angular distributions for the 0.774, 4.127

that for the first excited state of ^{27}Al (En62).

The fact that the ^{27}Si ground state has $J^{\pi}=5/2^{+}$ would suggest a spherical or prolate shape ($\delta \geq 0$) on the basis of the Nilsson model (Fig. 5.1), but the existance of the $1/2^{+}$ level at low excitation energy (0.774 MeV) suggests a pick-up from Nilsson orbit 6 with an oblate deformation ($\delta<0$). Also, the 0.952 MeV $3/2^{+}$ level could be excited by removing a neutron from orbit 7 with either a positive or negative δ. It is thus difficult to interpret the ground state of ^{28}Si in terms of the simple Nilsson model. This is not inconsistent with the result of a recent Hartree-Fock calculation, which suggests that the ^{28}Si nucleus undergoes shape oscillations (Mu67).

(b) Negative Parity Levels

The angular distributions for two $\ell_n=1$ levels of ^{27}Si at 4.127 and 5.233 MeV excitation are also shown in Fig. 5.13. The corresponding levels in the mirror nucleus have been observed by Wildenthal and Newman in the ^{28}Si(d, ^{3}He)^{27}Al proton pick-up reaction (Wi67). The predictions of Hartree-Fock calculations (Da66) and the conclusions of proton knock-out experiments (Ri65, Ja66) indicate a separation energy difference between the 1p and 2s-1d shells of 10 to 20 MeV in this mass region. This led to the conclusion that, because of their low

excitation energy, these levels are excited mainly by a pick-up from the 2p shell (Wi67). It seems worthwhile to note, however, that in the analysis of (p, 2p) data, it is difficult to distinguish between nuclear shells for which $l \neq 0$ (Ri65). For example, the data corresponding to a proton knock-out from the $1p_{1/2}$ shell could look very similar to that for a $d_{5/2}$ shell knock-out. In Fig. 5.14 the (p,d) reaction Q-values to the l_n=1 levels of lowest excitation are plotted for the N=Z, even-even nuclei for A=16 - 28 (La61 and this thesis). Since the transition to the ^{15}O ground state is due to a pick-up from the $1p_{1/2}$ shell, it seems reasonable, from the observed trend in the neutron separation energy, that the l_n=1 levels in the other nuclei could also be excited by a 1p pick-up. The strengths of these excitations are of little help in resolving this ambiguity, since a DWBA calculation predicts a much lower spectroscopic factor for a 2p pick-up than for a 1p pick-up (See Chapter 6). One can conclude from the plot in Fig. 5.14, however, that the evidence is at least as strong for a 1p hole state as for a 2p admixture.

5.2.2 J-dependence

The angular distributions for the ground ($5/2^+$) and 0.952 MeV levels ($3/2^+$) (Fig. 5.11) seem to be

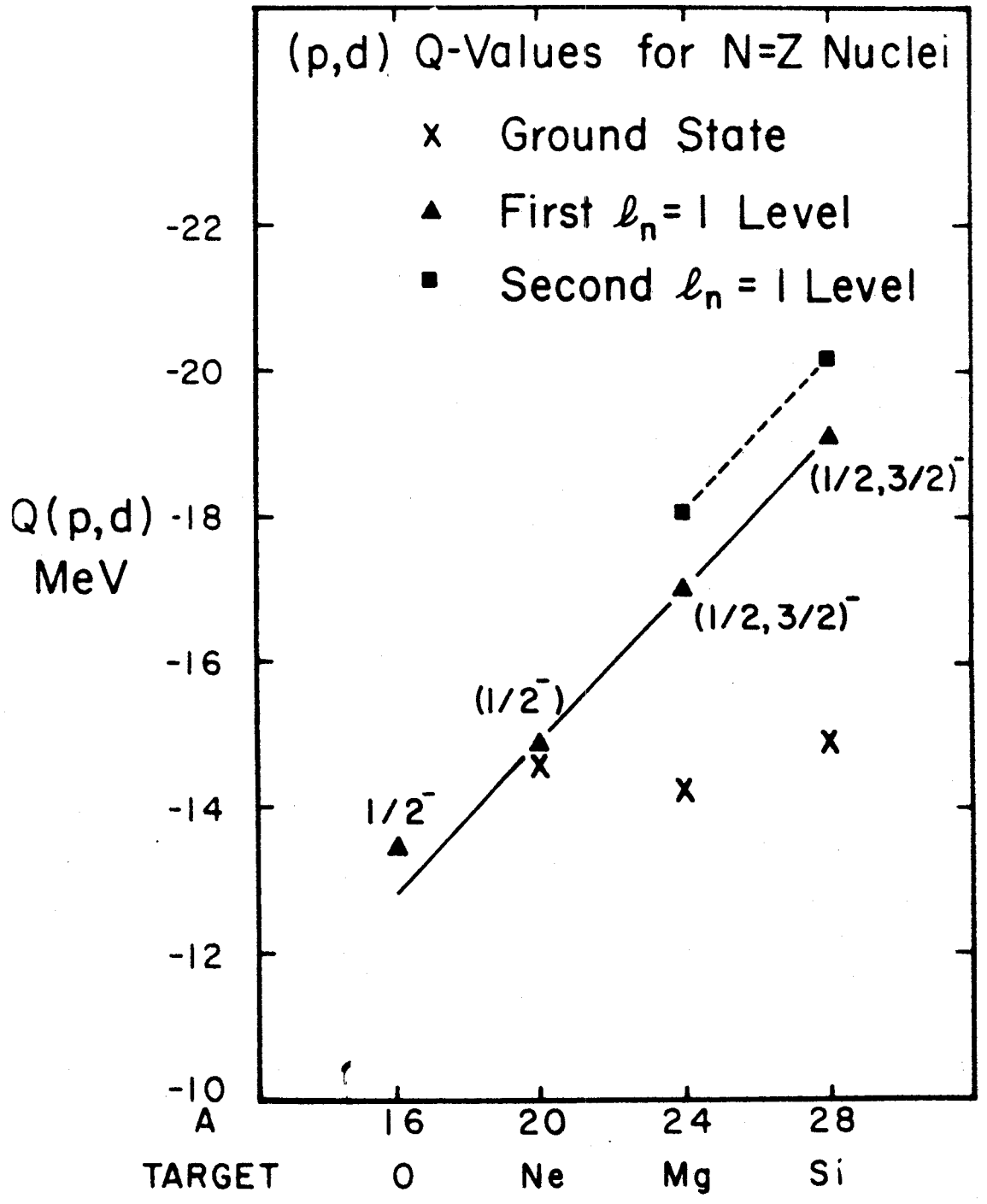

Figure 5.14. Plot of (p,d) reaction Q-values to ℓ_n=1 levels in N=Z nuclei versus target mass number. Straight lines are drawn for comparison.

very similar in shape, although there seems to be a flattening of the cross-section for the $3/2^+$ level for $\theta_{c.m.} \gtrsim 60^\circ$. The angle at which the forward maximum occurs in the $3/2^+$ distribution is about the same, or slightly smaller than for J=5/2. The relatively poor statistics for the $3/2^+$ level make this judgment difficult.

5.2.3 Summary

The excitation energies, spins and parities of the levels excited in the $^{28}Si(p,d)^{27}Si$ reaction are shown in Fig. 5.15. The energy measurements for the first six excited levels are in agreement with Ref. En62. Due to the constant presence of well-known ^{15}O levels in the spectrum, energy measurements with $\pm$10 keV error were possible in many cases.

The level order of ^{27}Si is difficult to interpret on the basis of a simple rotational model, especially if the ground state transition is included. The large number of levels excited by the direct pick-up process indicates that the configuration mixing in the ^{28}Si ground state is complex.

5.3 $^{16}O(p,d)^{15}O$

The ground and 6.16 MeV levels of ^{15}O are strongly excited in the (p,d) reaction on the SiO target (Figs. 5.9 and 5.10). These levels have

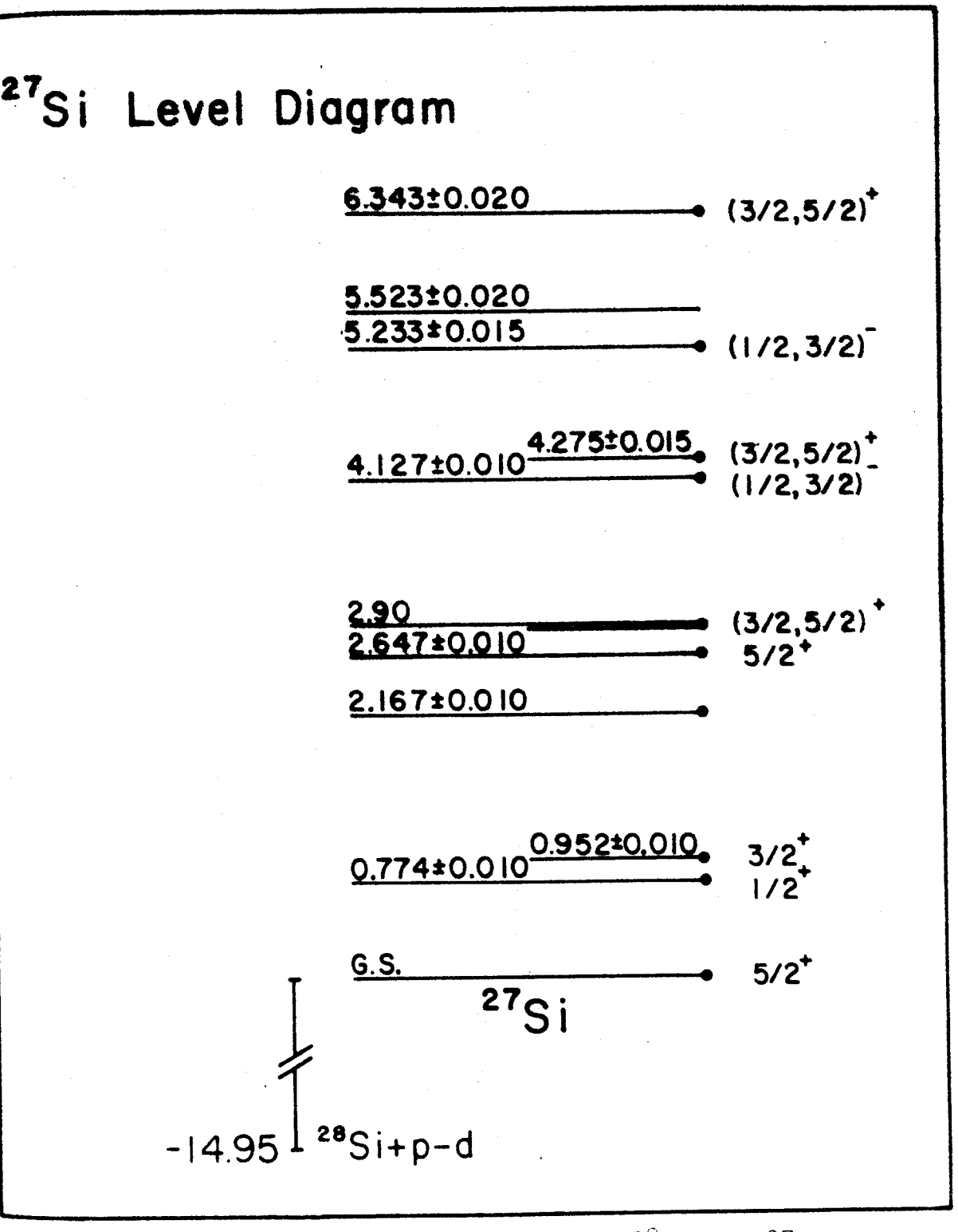

Figure 5.15. ^{27}Si levels observed in the ^{28}Si(p,d)^{27}Si reaction. The heavy dots indicate levels for which angular distributions were measured

spins and parities $1/2^-$ and $3/2^-$ respectively, corresponding to $1p_{1/2}$ and $1p_{3/2}$ neutron pick-ups. The J-dependence in their angular distributions (Fig. 5.16) is similar to that observed in the $^{16}O(p,d)^{15}O$ reaction with 35 and 40 MeV protons (Gr66). There is generally more structure in the $j=\ell_n-1/2$ distribution than for $j=\ell_n+1/2$, which is also the case for $\ell_n=2$ pick-ups from ^{32}S, ^{36}Ar and ^{40}Ca (See Secs. 5.4 - 5.6). The well known ^{15}O doublets (La61) at excitation energies 5.2, 9.5 and 9.6 MeV are indicated in the spectra (Figs. 5.9 and 5.10). A level at $E_x=10.55\pm0.05$ MeV in ^{15}O is also observed.

5.4 $^{32}S(p,d)^{31}S$

5.4.1 Results and Interpretation

Figures 5.17 and 5.18 show deuteron spectra from the (p,d) reaction on the H_2S gas target at laboratory angles 30° and 90°. The overall resolution is about 120 keV. Many of the thirty-nine levels observed in a $^{32}S(^3He,\alpha)^{31}S$ experiment (Aj66) are accounted for, in addition to a very weak level at $E_x=3.05\pm0.02$ MeV which had been observed earlier (We65, Ne63). No strongly excited ^{31}S levels are observed for $E_x>7.05$ MeV.

The deuteron angular distributions from levels of ^{31}S at 1.24, 2.23 and 4.09 MeV excitation energies

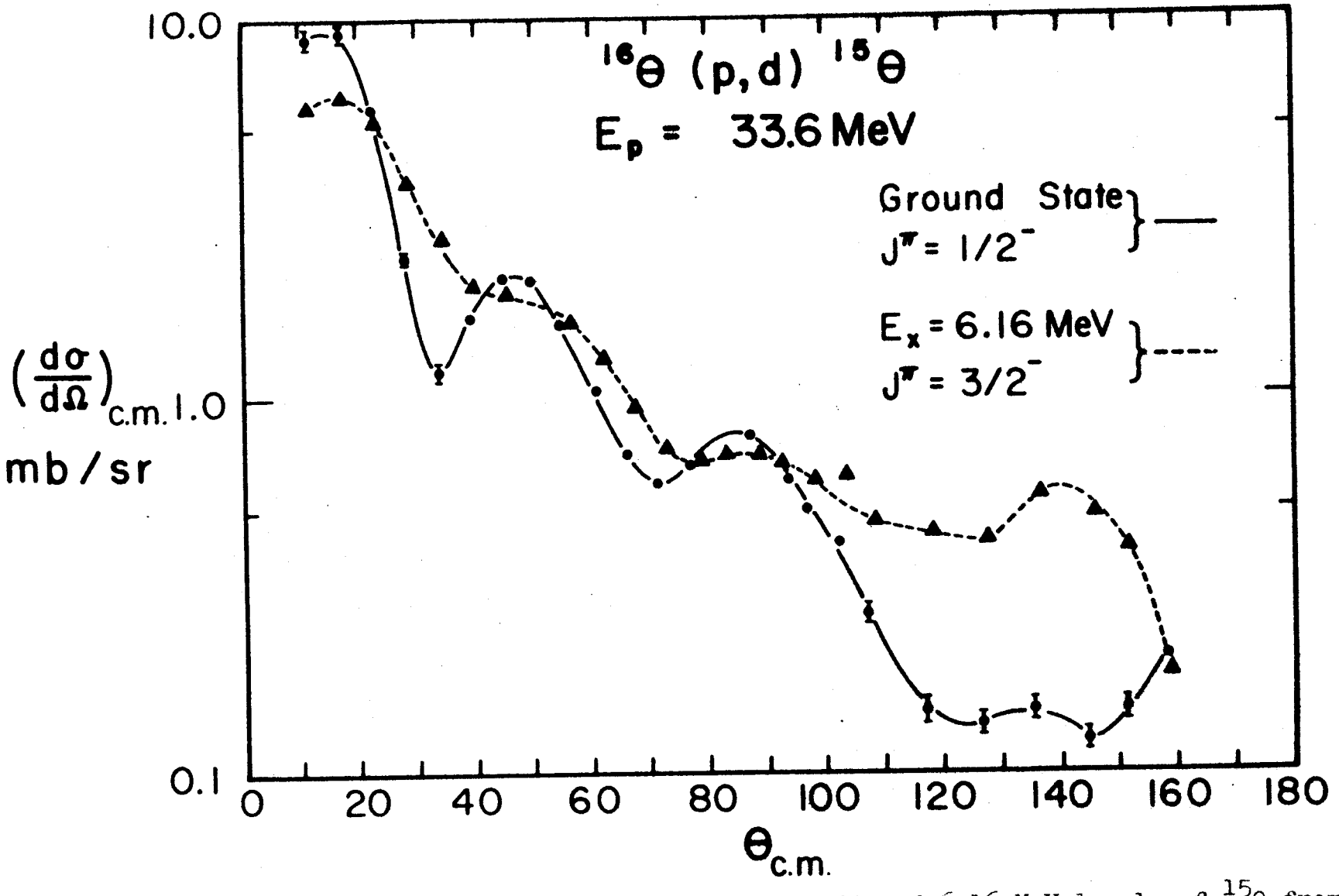

[illegible]. Deuteron angular distributions for the 0.00 and 6.16 MeV levels of ^{15}O from the [illegible](p,d)^{15}O reaction. The J- dependence is similar to that observed by Ref. Gr66.

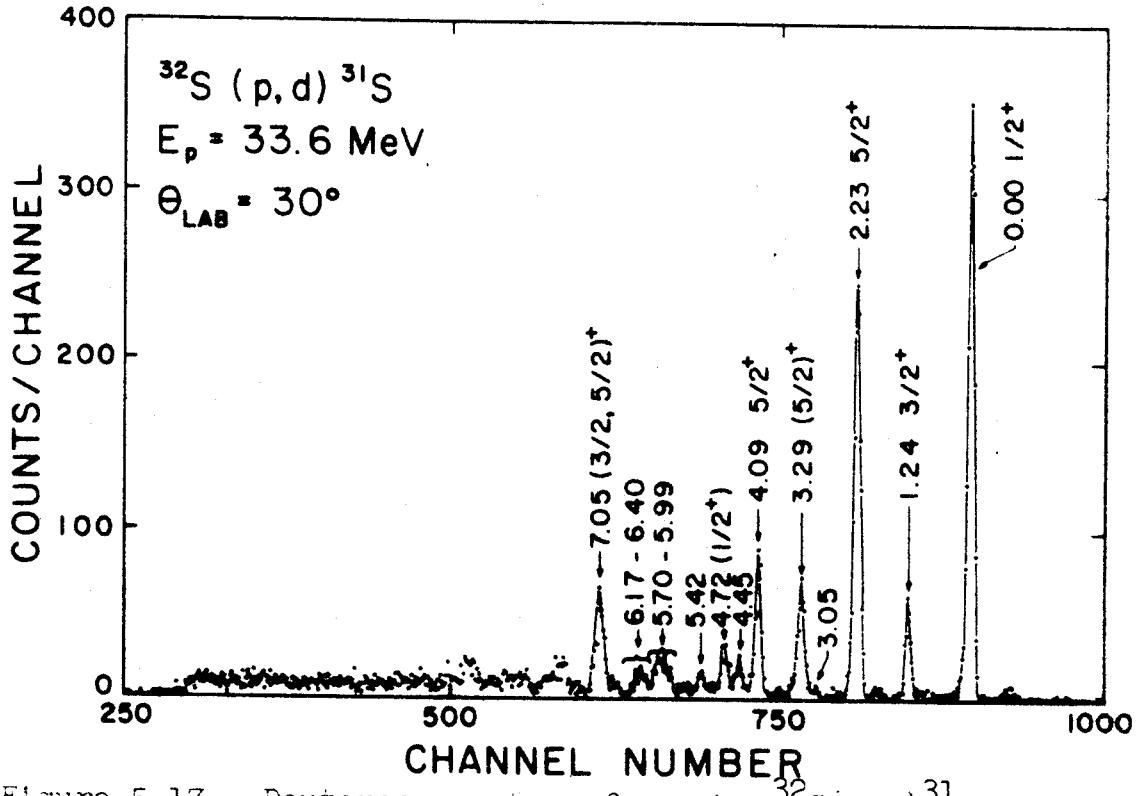

Figure 5.17. Deuteron spectrum from the $^{32}S(p,d)^{31}S$ reaction at $\theta_{LAB}=30^{\circ}$. No strongly excited levels are observed for E_x > 7.05 MeV.

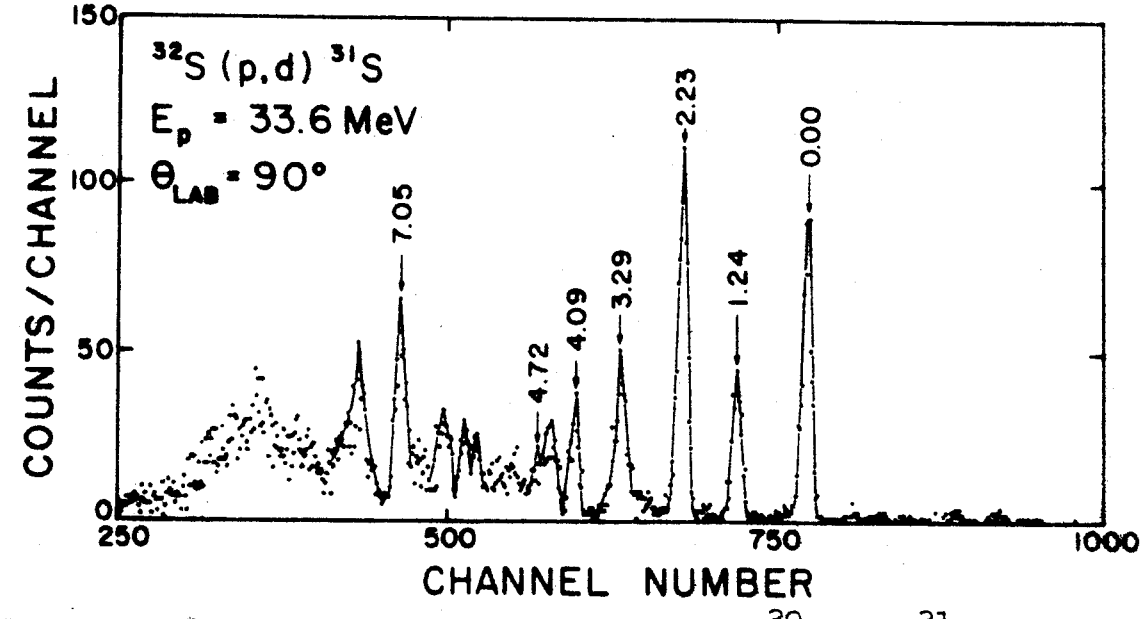

Figure 5.18. Deuteron spectrum from the $^{32}S(p,d)^{31}S$ reaction at $\theta_{LAB}=90^{\circ}$.

are shown in Fig. 5.19. All of these distributions correspond to an ℓ_n=2 neutron pick-up, and the respective assignments $3/2^+$, $5/2^+$ and $5/2^+$ are consistent with those for the corresponding levels in the mirror nucleus ^{31}P. Angular distributions were also measured for the ground, 3.29, 4.72 and 7.05 MeV levels and are shown in Fig. 5.20. The ground state corresponds to an ℓ_n=0 pick-up and has the expected spin and parity of $1/2^+$. The distribution for the 4.72 MeV level could also be due to an ℓ_n=0 pick-up, although the statistical errors are quite large. The 3.29 MeV level is excited mainly by an ℓ_n=2 pick-up, although the angular distribution indicates the presence of other admixtures. Ajzenberg-Selove and Wiza (Aj66) have reported a level at 3.359±0.015 MeV, which would be unresolved here. The $(5/2)^+$ assignment is consistent with the assignment for a possible mirror level in ^{31}P at the same energy (En62). The 7.05 MeV distribution also corresponds to an ℓ_n=2 pick-up, indicating that $J^\pi=(3/2, 5/2)^+$ for this level.

The first three levels of ^{31}S are the 0.00 $(1/2^+)$, 1.24 $(3/2^+)$ and 2.23 MeV $(5/2^+)$ levels, whose spins and parities are consistent with a rotational band based on a neutron hole in Nilsson orbit 9 with either a prolate or an oblate deformation (Fig. 5.1). This possibility will be investigated further in Chapter 6 by comparing the experimental spectroscopic factors

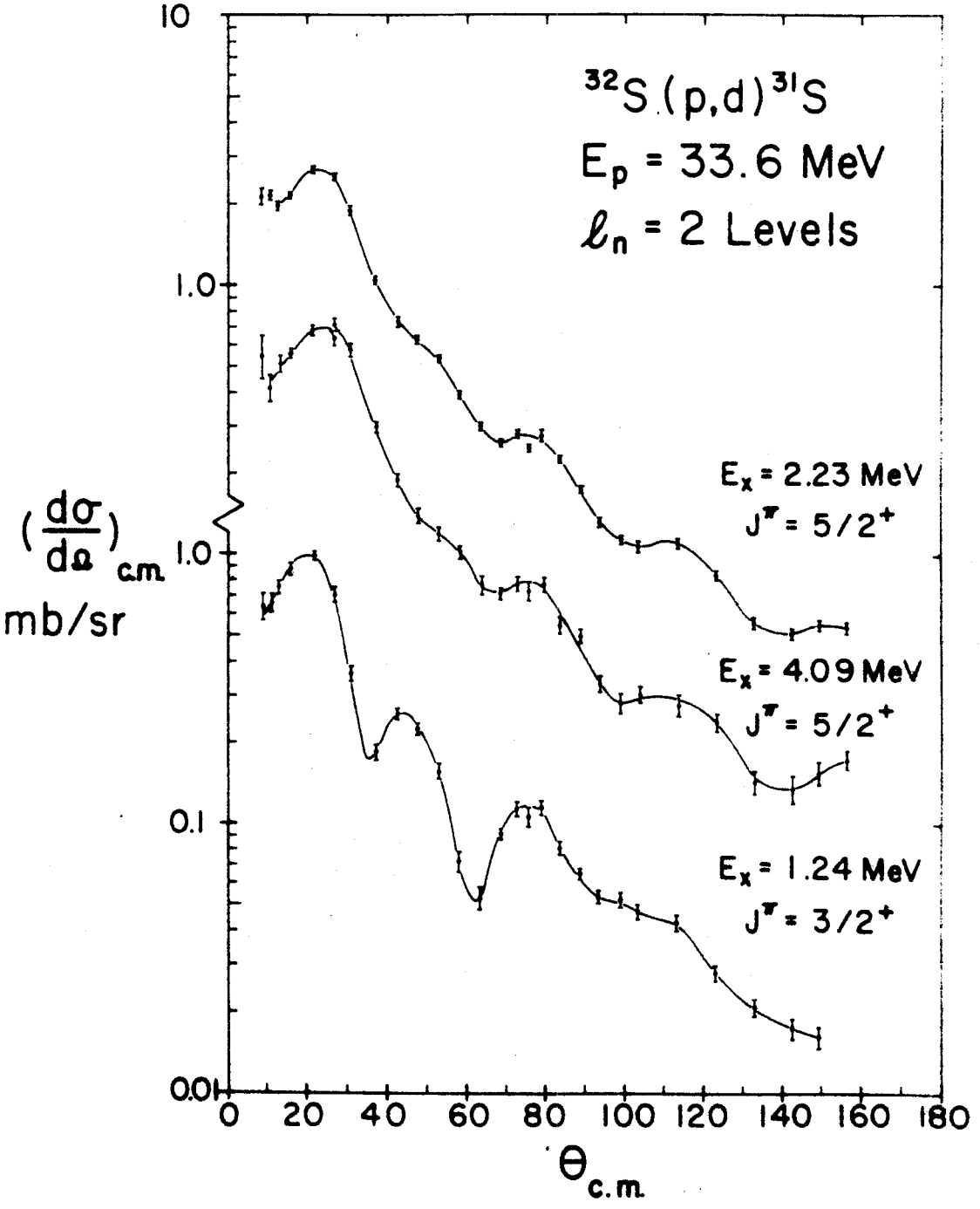

Figure 5.19. Deuteron angular distributions for the 1.24, 2.23, and 4.09 MeV levels of ^{31}S from the $^{32}S(p,d)^{31}S$ reaction. The J-dependence is similar to that observed by Ref. G165 (a).

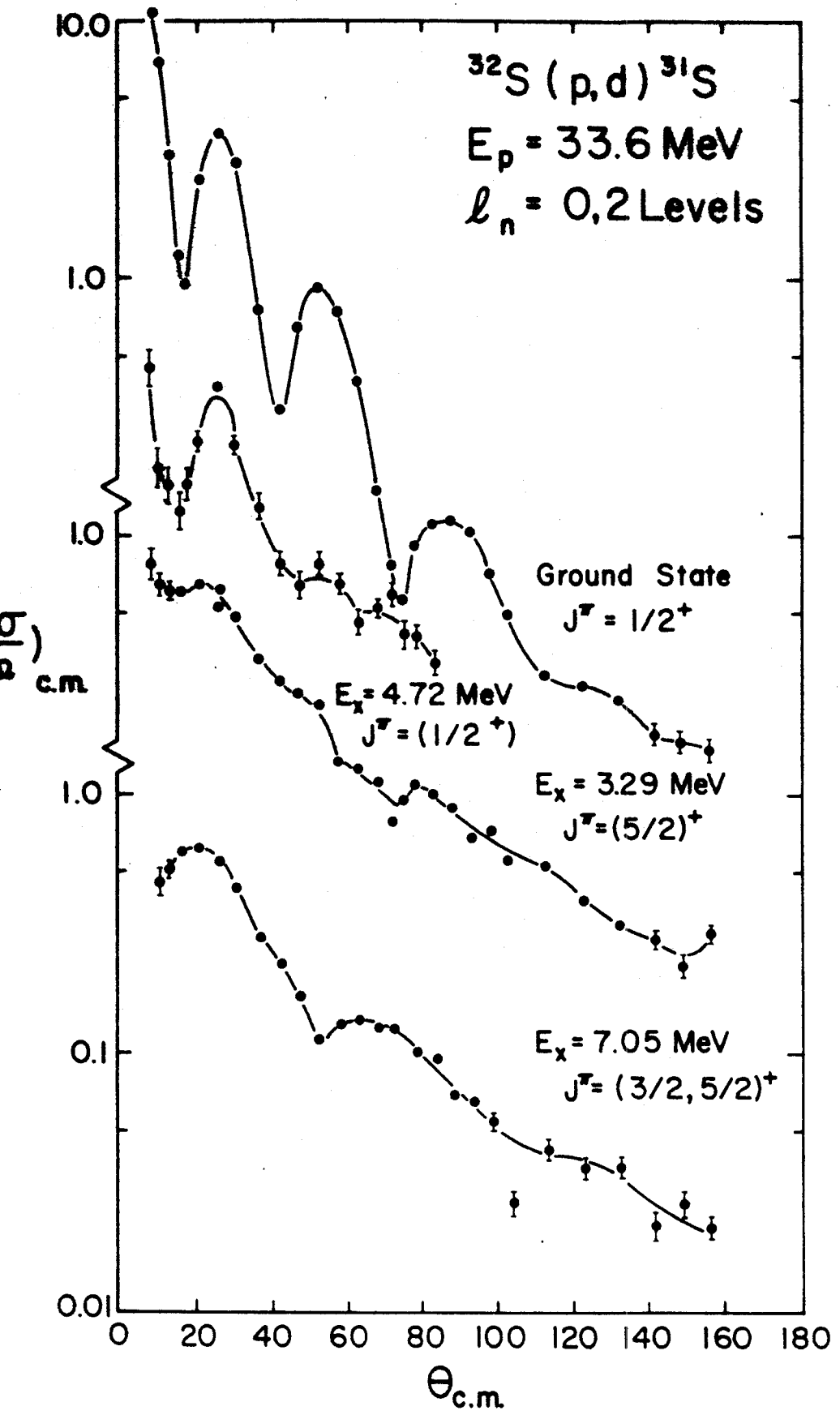

Figure 5.20. Deuteron angular distributions for the 0.00, [illegible] and 7.05 MeV levels of ^{31}S from the $^{32}S(p,d)^{31}S$ reaction.

with theoretical predictions of Nilsson model wave functions.

5.4.2 J-dependence

The $J^{\pi}=3/2^{+}$ and $5/2^{+}$ angular distributions shown in Fig. 5.19 exhibit a very striking example of J-dependence in the 1d shell, which is similar to that observed in the (p,d) reaction with 28 MeV protons (G165 (a)). The forward maximum of the distribution for the 1.24 MeV level (3/2) in ^{31}S occurs at a smaller angle than the distributions for either the 2.23 MeV or 4.09 MeV levels (both 5/2), and drops off much more rapidly to the first minimum. The oscillatory structure is much more pronounced for J=3/2; in fact, the second maximum ($\theta \approx 45^{\circ}$) is barely noticeable in the angular distributions for the $5/2^{+}$ levels. It is evident that the 4.09 MeV level, whose distribution is also shown in Fig. 5.19, could have been assigned $J^{\pi}=5/2^{+}$ on the basis of J-dependence alone. This is an example of the usefulness of J-dependence as a spectroscopic tool.

5.4.3 Summary

Figure 5.21 shows the ^{31}S levels indicated in the deuteron spectra (Figs. 5.17 and 5.18). The energy measurements are in agreement with the results of Ref. Aj66, to within about ± 20 keV for each level.

Due to the spins and parities of the strongly

^{31}S Level Diagram

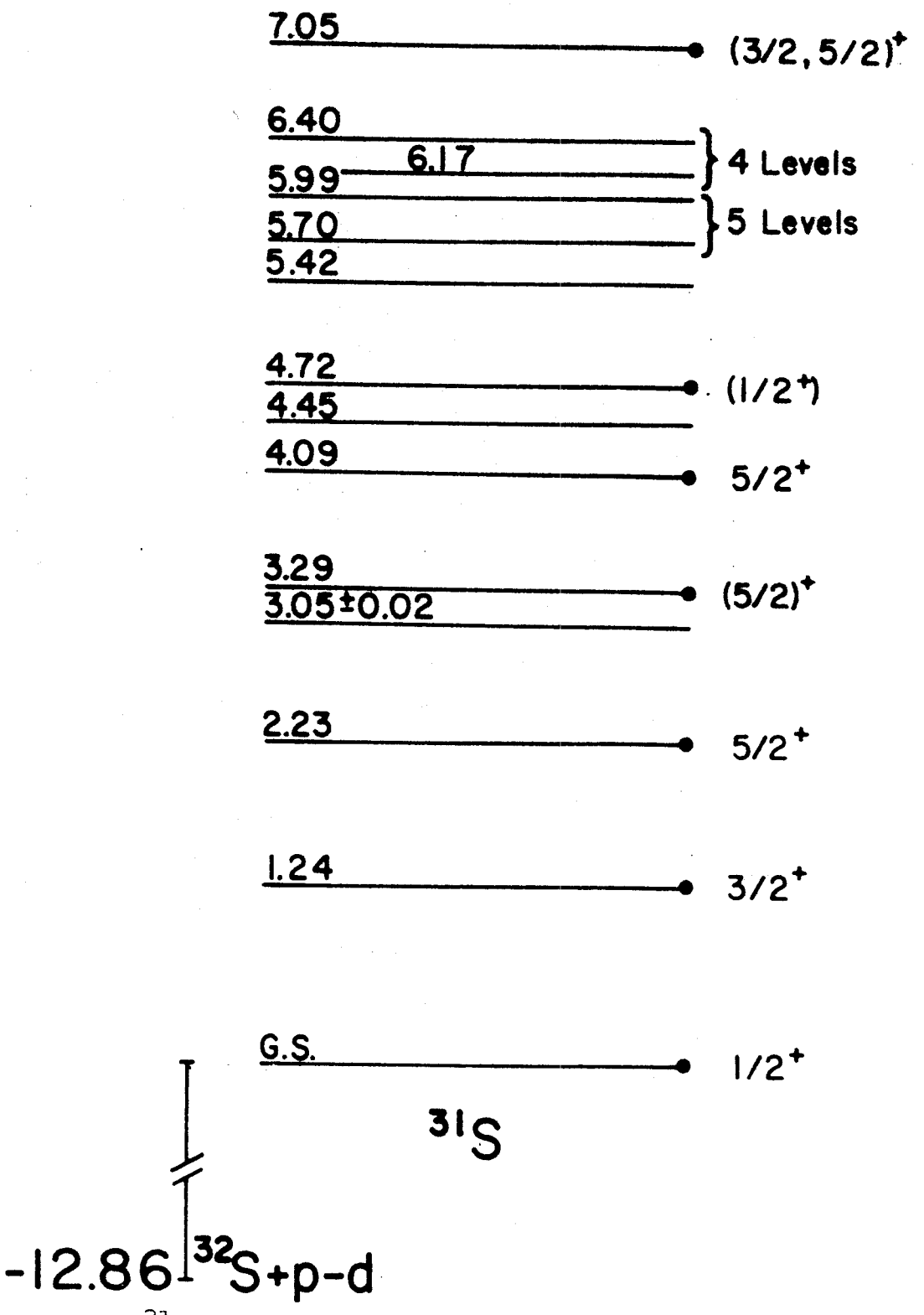

Figure 5.21. ^{31}S levels observed in the ^{32}S(p,d)^{31}S reaction. The heavy dots indicate levels for which angular distributions were measured.

excited levels, it appears that the configuration mixing in the ^{32}S ground state is less complicated than in ^{24}Mg and ^{28}Si (Secs. 5.1 and 5.2). In fact, the only confirmed admixture of sizeable strength is a $[d_{3/2}]^2$ configuration which results in the strong excitation of the 1.24 MeV $3/2^+$ level. The spins and parities of the ground and first two excited states are consistent with the strong coupling rotational model.

5.5 $^{36}Ar(p,d)^{35}Ar$

5.5.1 Results and Interpretation

Thirteen deuteron groups, corresponding to levels in ^{35}Ar, were observed in the $^{36}Ar(p,d)^{35}Ar$ reaction. Typical spectra from the gas target described in Chapter 4 are shown in Figs. 5.22 and 5.23, where the overall resolution is about 130 keV.

Angular distributions were measured for ten levels of ^{35}Ar and are shown in Figs. 5.24, 5.25 and 5.26. The $\ell_n=2$ distributions for levels at 0.00, 2.60, 2.95 and 6.82 MeV excitation (Fig. 5.24) show that they are excited by neutron pick-ups from the $d_{3/2}$ and $d_{5/2}$ shells. The spin assignments for the 2.60 ($3/2^+$) and 2.95 MeV ($5/2^+$) levels are made on the basis of the observed J-dependence discussed in Sec. 5.5.2. The ground state assignment of $3/2^+$ corresponds to the spin and parity of the ^{35}Cl mirror nucleus (En62).

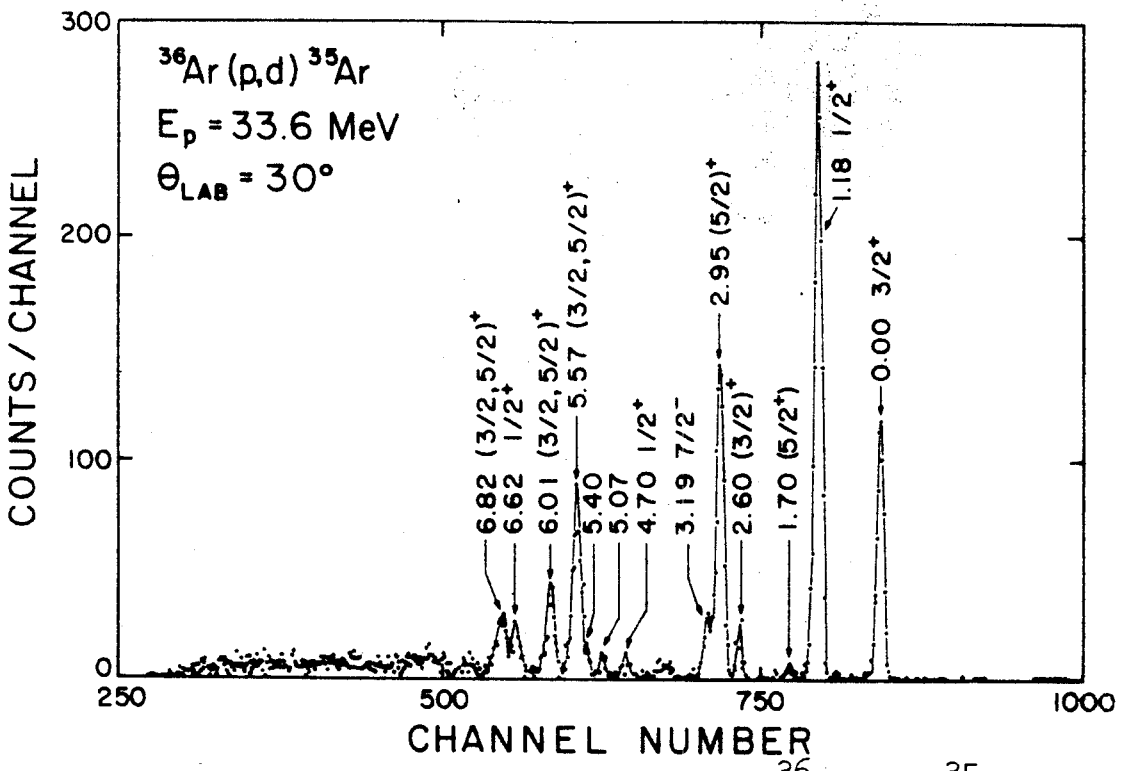

Figure 5.22. Deuteron spectrum from the $^{36}Ar(p,d)^{35}Ar$ reaction at $\theta_{LAB}=30°$. It is apparent that all of the 2s-1d shell hole strength has been observed.

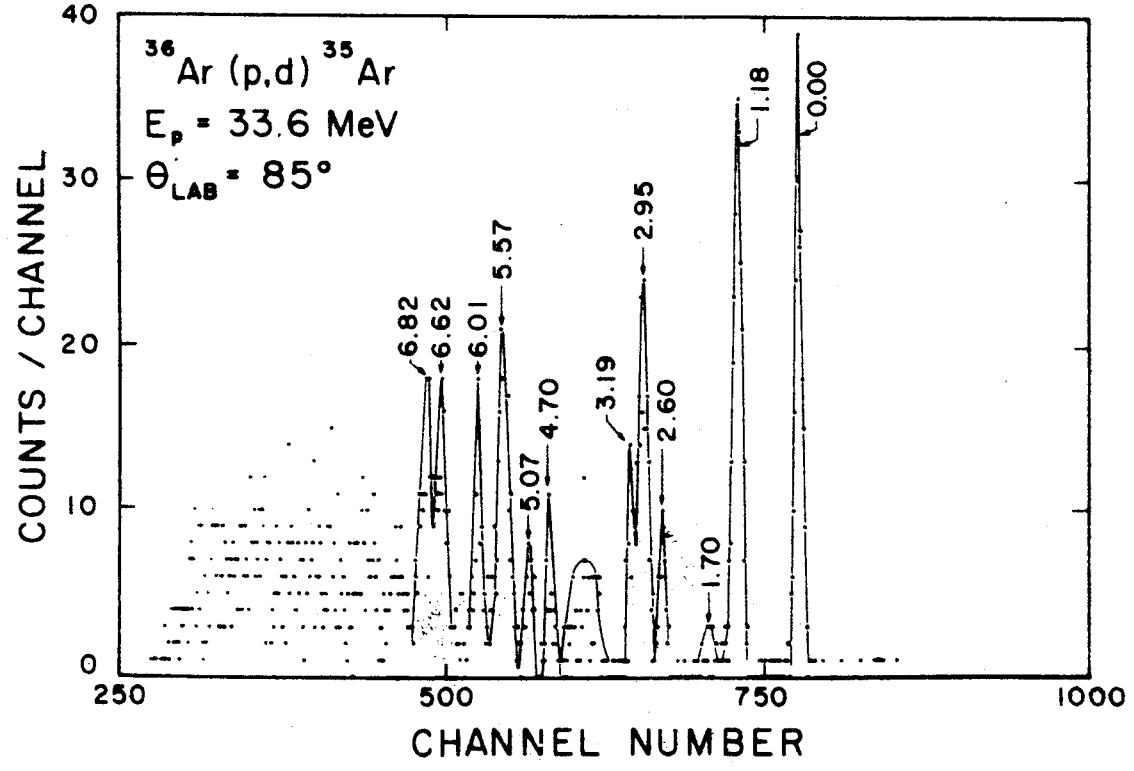

Figure 5.23. Deuteron spectrum from the $^{36}Ar(p,d)^{35}Ar$ reaction at $\theta_{LAB}=85°$.

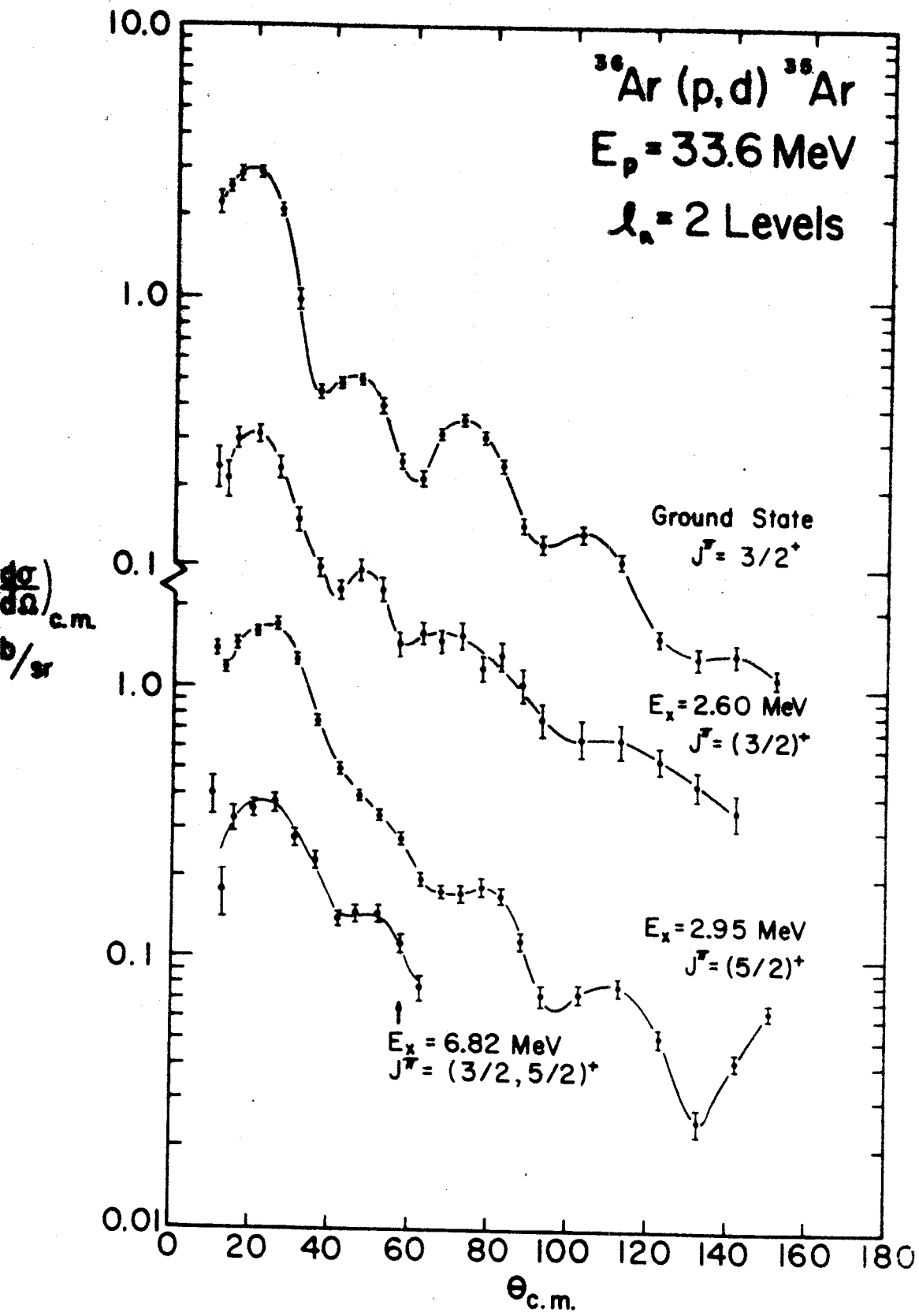

Figure 5.24. Deuteron angular distributions for the 0.00, 2.[illegible], [illegible] and 6.82 MeV levels of ^{35}Ar from the ^{36}Ar(p,d)^{35}Ar reaction. [illegible] assignments to the 2.60 and 2.95 MeV levels are made on the basis of [illegible]-dependence.

The spin of the 6.82 MeV level is uncertain but must be either 3/2 or 5/2. The distributions for the 5.57 and 6.01 MeV levels also correspond to an $\ell_n=2$ pick-up (Fig. 5.25) and are therefore assigned $J^\pi = (3/2, 5/2)^+$.

The angular distributions for the 1.18, 4.70, 6.62 and 3.19 MeV levels of ^{35}Ar are shown in Fig. 5.26. The first three of these correspond to an $\ell_n=0$ pick-up and therefore have $J^\pi=1/2^+$. The distribution for the 3.19 MeV level peaks at $\theta_{c.m.} \approx 30°$, which indicates that this level is excited by the pick-up of an $\ell_n=3$ neutron. This indicates configuration mixing with the 1f shell in the ^{36}Ar ground state. The level is assigned $J^\pi=7/2^-$ since a spin of 7/2 is most probable from a shell model standpoint, and the mirror level in ^{35}Cl is believed to have the same assignment (En62).

The spins and parities are $3/2^+$, $1/2^+$, $(5/2^+)$, $(3/2)^+$ and $(5/2)^+$ for levels of ^{35}Ar at 0.00, 1.18, 1.70, 2.60 and 2.95 MeV respectively, where the assignment for the 1.70 MeV level is assumed from the mirror level in ^{35}Cl (En62). By inspection of Fig. 5.1, this level order is consistent with that of rotational bands based on neutron pick-ups from Nilsson orbits 8 (first and third levels) and 9 (second, fourth and fifth levels) if $-0.2<\delta<0$ (oblate). The 4.70 MeV level ($1/2^+$) could then be excited by a pick-up from orbit 6, with at least

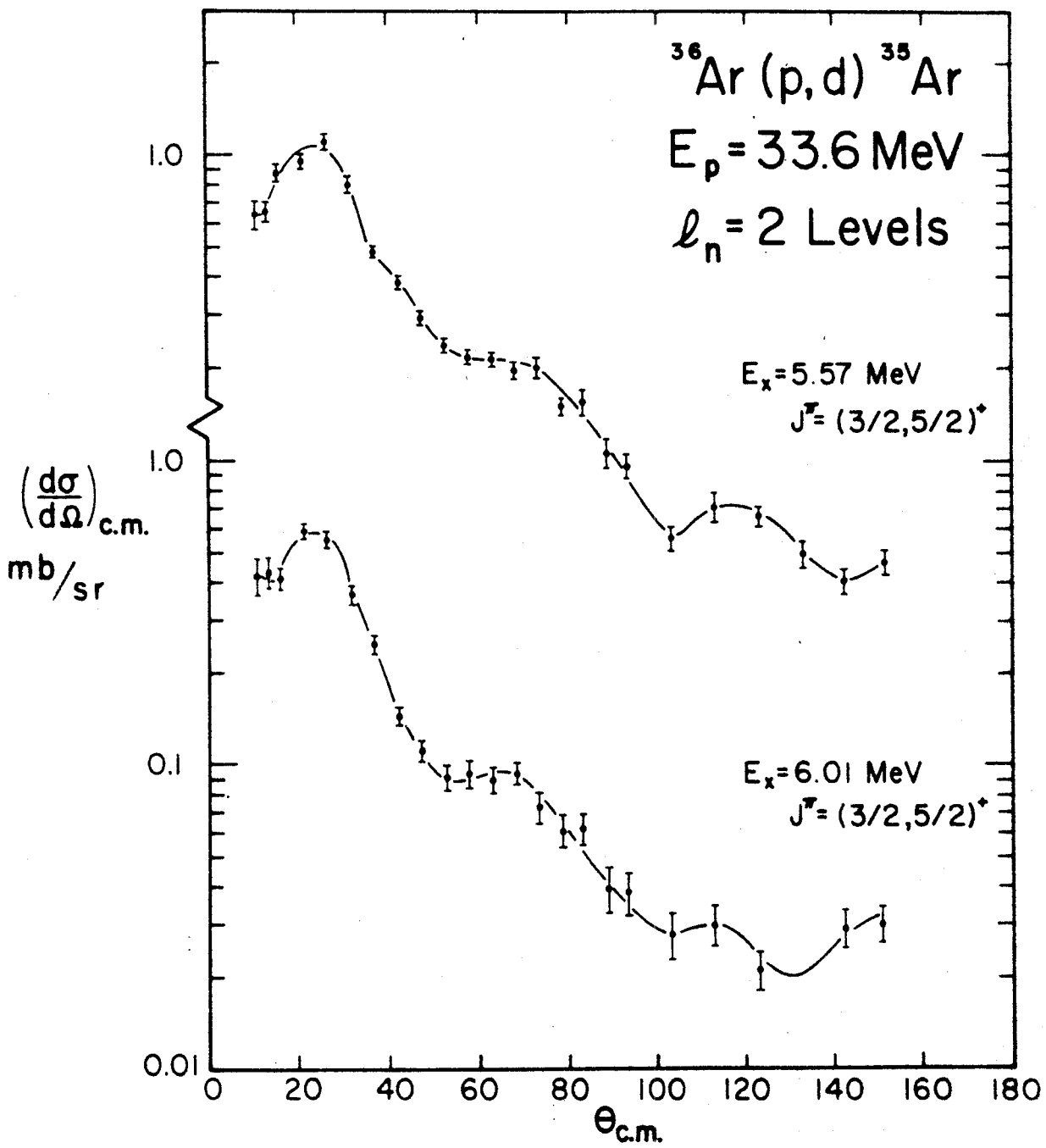

Figure 5.25. Deuteron angular distributions for the 5.57 and 6.01 MeV levels of ^{35}Ar from the ^{36}Ar(p,d)^{35}Ar reaction.

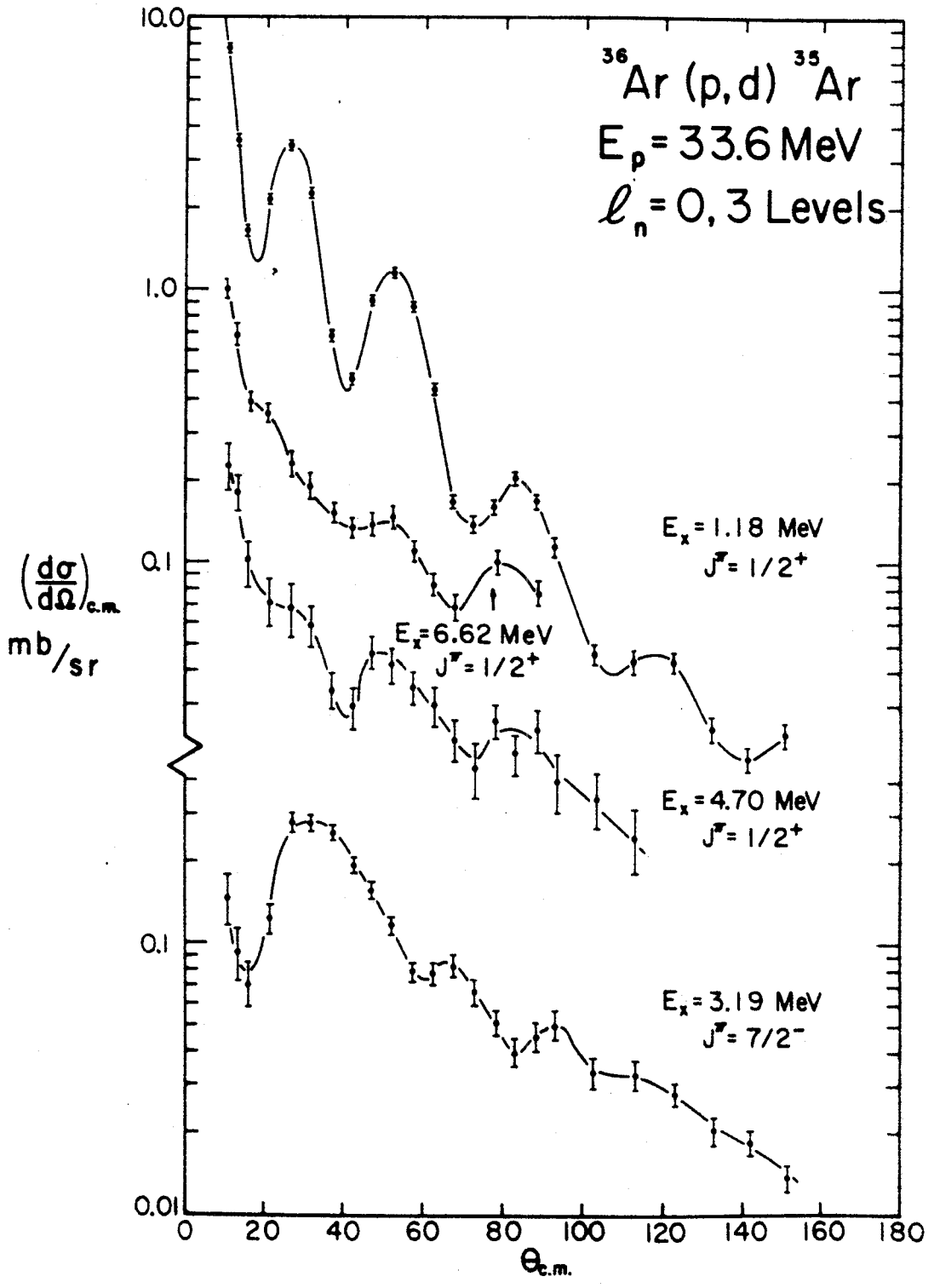

Figure 5.26. Deuteron angular distributions for the 1.18, 3.19, 4.70 and 6.62 MeV levels of ^{35}Ar from the ^{36}Ar(p,d)^{35}Ar reaction.

three remaining candidates (5.57, 6.01 and 6.82 MeV levels) for the $3/2^+$ and $5/2^+$ levels of this band. The excitation of a third $1/2^+$ level (6.62 MeV) and a $7/2^-$ level (3.19 MeV) indicates some configuration mixing of Nilsson orbits, possibly to orbits 11 (K= 1/2) and 10 (K=7/2), respectively.

5.5.2 J-dependence

The J-dependence observed in the $^{36}Ar(p,d)^{35}Ar$ reaction for $3/2^+$ and $5/2^+$ levels (Fig. 5.24) is very similar to that for the $^{32}S(p,d)^{31}S$ reaction. The angular distributions for the 2.23 and 4.09 MeV levels of ^{31}S and the 2.95 MeV level of ^{35}Ar are practically identical in shape for $\theta_{c.m.} \leq 90^\circ$ (Figs. 5.19 and 5.24). Since both of the ^{31}S levels have J=5/2, the 2.95 MeV level of ^{35}Ar is assigned $J^\pi = (5/2)^+$. The distributions for the ground and 2.60 MeV levels in ^{35}Ar are similar to the distribution for the ^{31}S 1.24 MeV level ($3/2^+$), although the oscillatory structure is not quite so pronounced. The existance of the 45° maximum and the relatively small angle for the forward maximum in the distribution for the 2.60 MeV level results in its assignment of $J^\pi = (3/2)^+$.

5.5.3 Summary

The diagram in Fig. 5.27 summarizes the information obtained about the level structure of ^{35}Ar

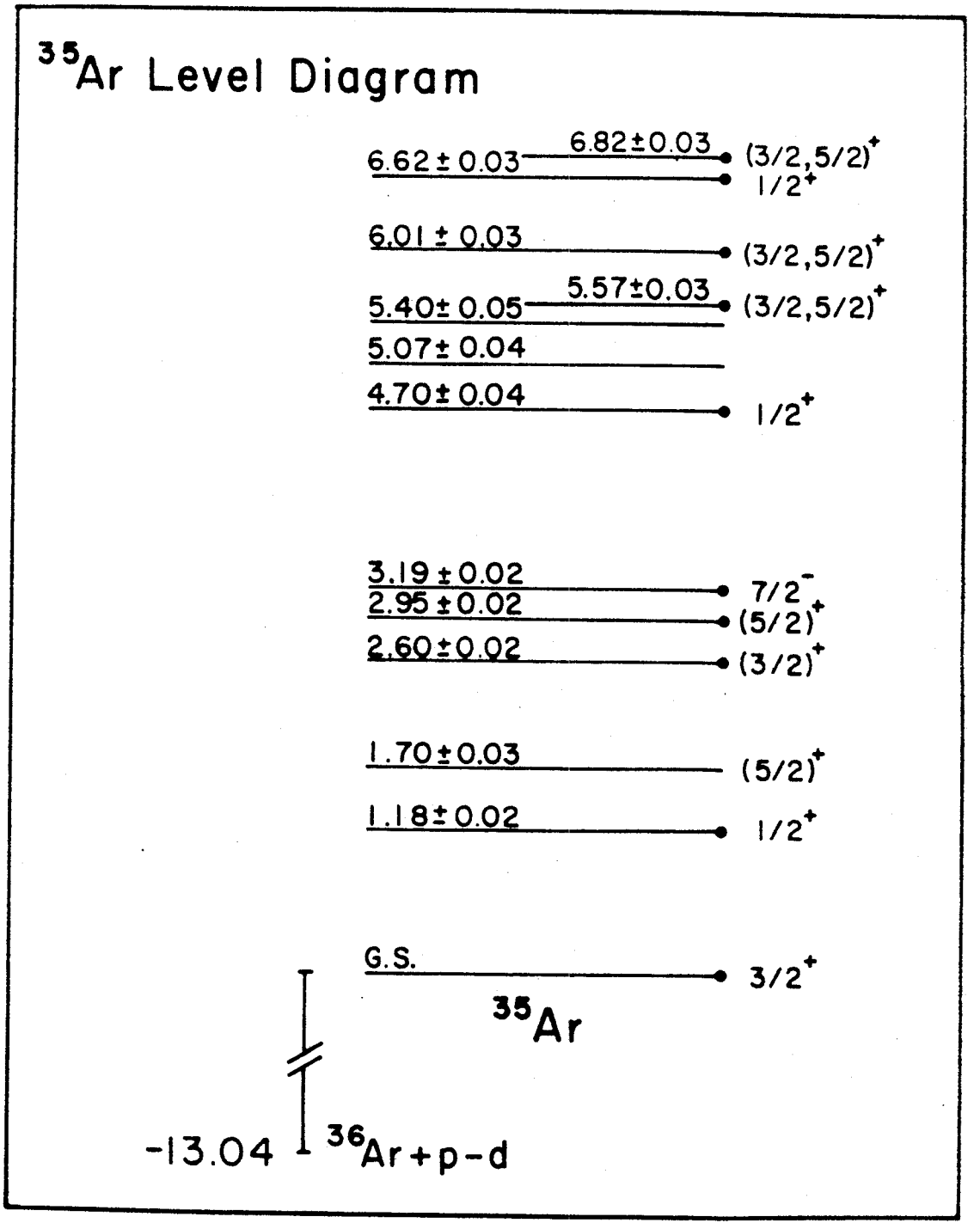

Figure 5.27. ^{35}Ar levels observed in the $^{36}Ar(p,d)^{35}Ar$ reaction. The heavy dots indicate levels for which angular distributions were measured.

from the (p,d) reaction. The large deuteron energy losses (~300 keV) in the 10 mg/cm^2 Havar windows of the gas cell partially contributed to the errors in measuring the level energies. The energies of the first five excited levels correspond closely to levels in the ^{35}Cl mirror nucleus.

The ordering of the ^{35}Ar levels appears to be qualitatively consistent with an oblate deformation in the strong coupling rotational model.

5.6 ^{40}Ca(p,d)^{39}Ca

5.6.1 Results and Interpretation

The deuteron spectra shown in Figs. 5.28 and 5.29 are similar to those obtained from the ^{40}Ca (p,d)^{39}Ca reaction by Glashausser, et. al., with 27.3 MeV protons (Gl65 (b)). A natural calcium foil of 1.10 mg/cm^2 was used where a resolution of 100 keV was obtained, and the normalization was checked with 1.67 and 2.27 mg/cm^2 foils. An oxygen contaminant of about 3% is indicated by the ^{15}O ground and 6.16 MeV levels, but this interfered with the data analysis only at the forward angles ($\theta_{LAB} \lesssim 15°$). Although about 12 MeV of excitation in ^{39}Ca is observed, there appears to be no excitation of appreciable strength beyond the 6.15 MeV level.

The angular distributions for the 0.00, 5.13, 5.48 and 6.15 MeV levels shown in Fig. 5.30

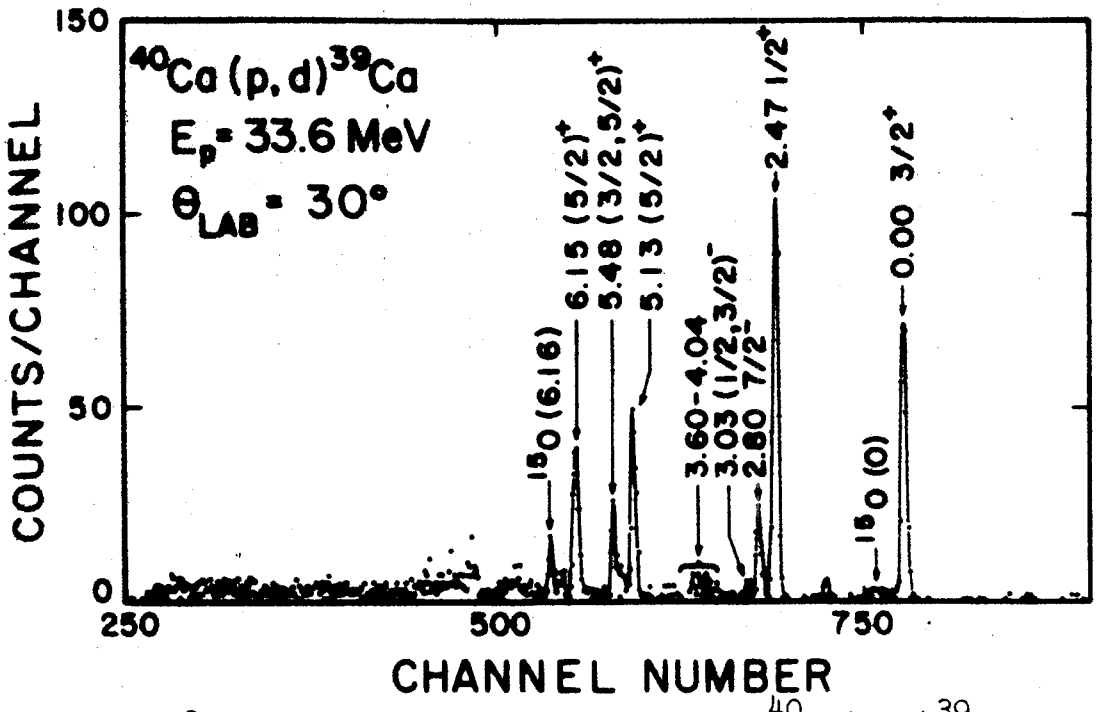

Figure 5.28. Deuteron spectrum from the $^{40}Ca(p,d)^{39}Ca$ reaction taken at $\theta_{LAB}=30^\circ$ (1.10 mg/cm^2 natural calcium target). It is apparent that all of the 2s-1d shell hole strength is observed.

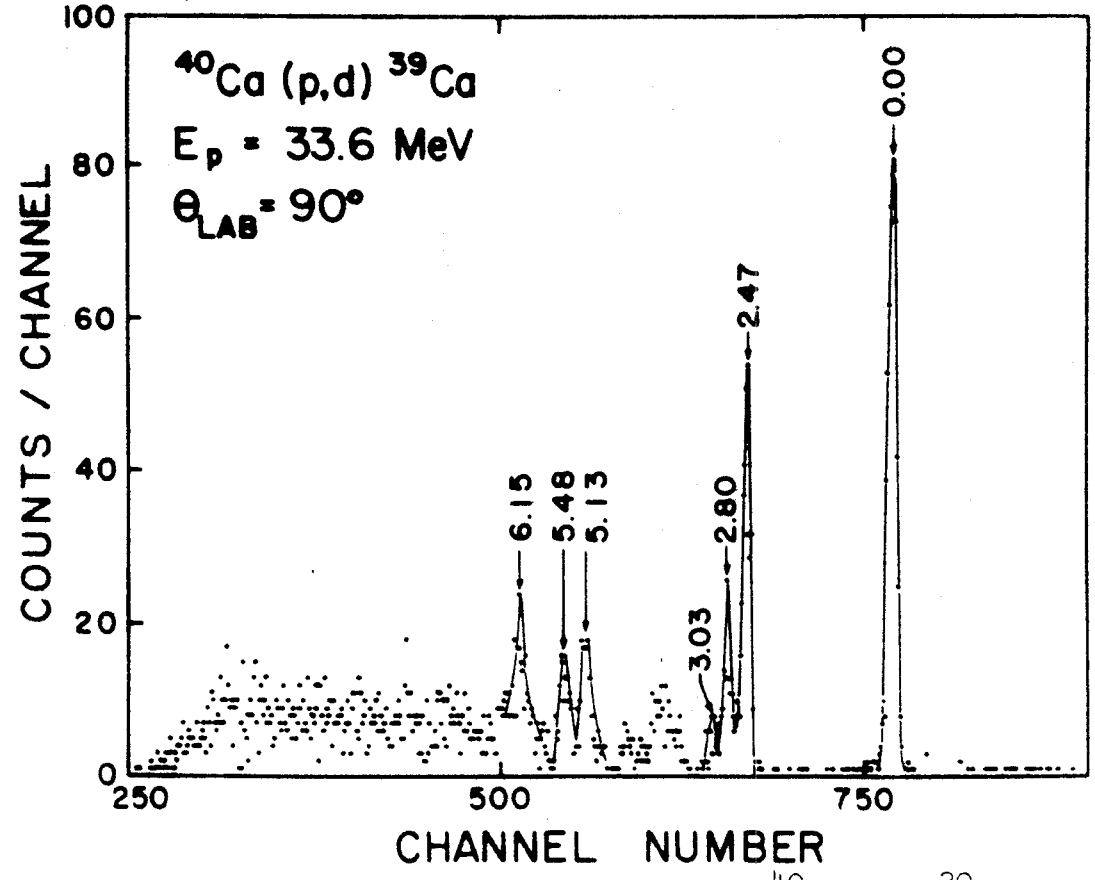

Figure 5.29. Deuteron spectrum from the $^{40}Ca(p,d)^{39}Ca$ reaction at $\theta_{LAB}=90^\circ$ (2.27 mg/cm^2 natural Ca target).

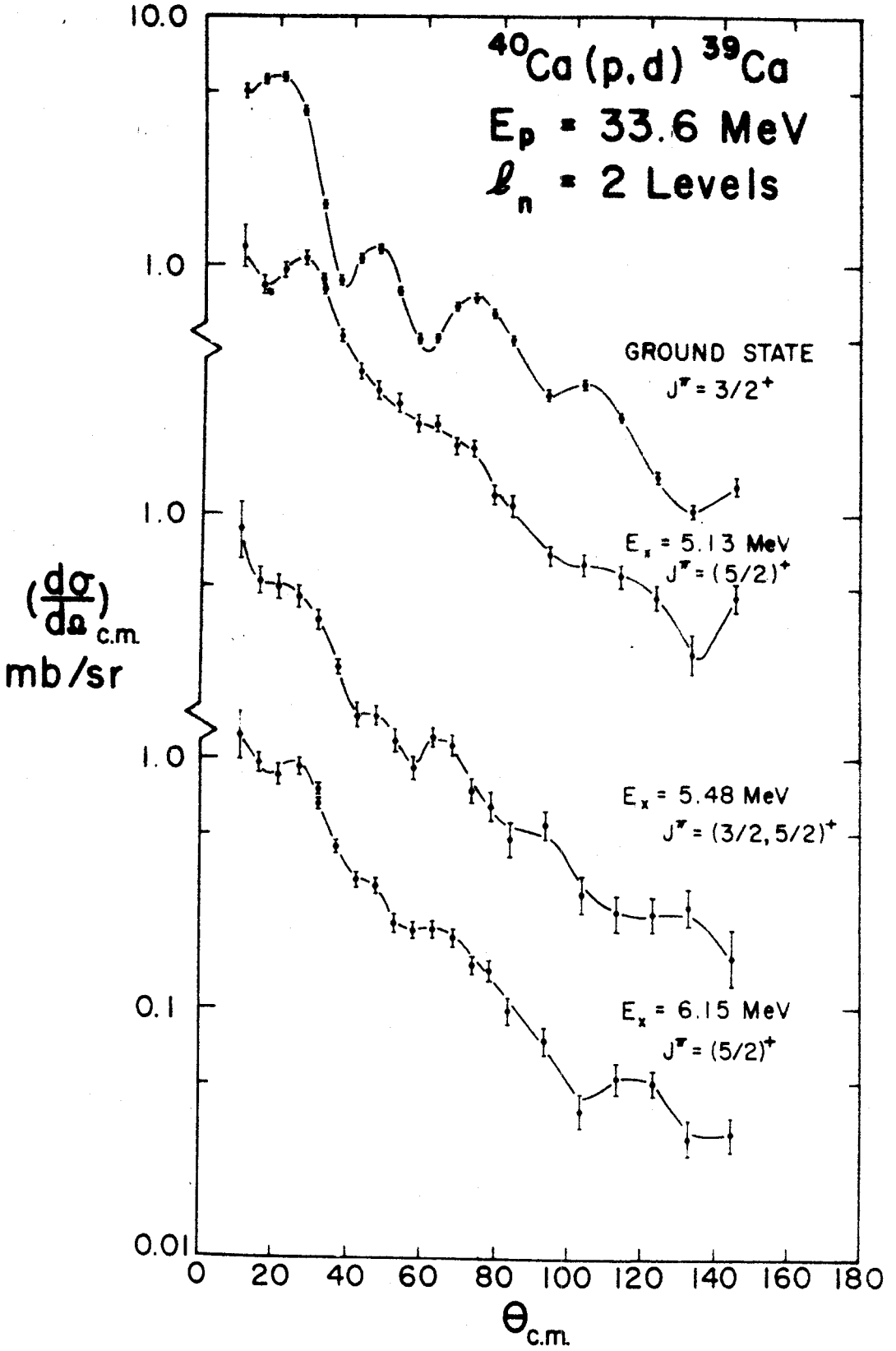

Figure 5.30. Deuteron angular distributions for the 0.00, 5.13, 5.48 and 6.15 MeV levels of ^{39}Ca from the ^{40}Ca(p,d)^{39}Ca reaction. The 5.13 MeV level is assigned $J^\pi=(5/2)^+$ on the basis of L- [illegible]

all correspond to an ℓ_n=2 pick-up. The ground state has J^π=3/2$^+$, which corresponds to the spin and parity of the mirror nucleus ^{39}K. The peak differential cross-section obtained at 33.6 MeV bombarding energy was about 6.0 mb/sr, and all three normalization checks agree within the statistical error. Glashausser et. al. (Gl65 (b)) obtained a value of ~3.0 mb/sr at 27.3 MeV bombarding energy, while Cavanagh et. al. (Ca04) measured ~4.5 mb/sr for the peak cross-section with 30 MeV protons. This indicates that the absolute differential cross-section may be quite sensitive to the bombarding energy.

The 5.13 MeV level is assigned J^π=(5/2)$^+$ on the basis of the J-dependence observed in the angular distributions (See Sec. 5.6.2). Although the angular distribution for the 5.48 MeV level has the basic ℓ_n=2 shape, which results in the (3/2, 5/2)$^+$ assignment, it also appears to contain contributions from unresolved levels corresponding to different ℓ_n values (e.g., ℓ_n=0). The angular distribution for the 6.15 MeV level is very similar to that for the 5.13 MeV (5/2$^+$) level and, from shell model considerations, a strongly excited 3/2$^+$ hole state of this excitation energy is not expected. The 6.15 MeV level is therefore given the tentative assignment J^π=(5/2)$^+$.

Figure 5.31 shows the angular distributions from ^{39}Ca levels at 2.47, 2.80 and 3.03 MeV. The

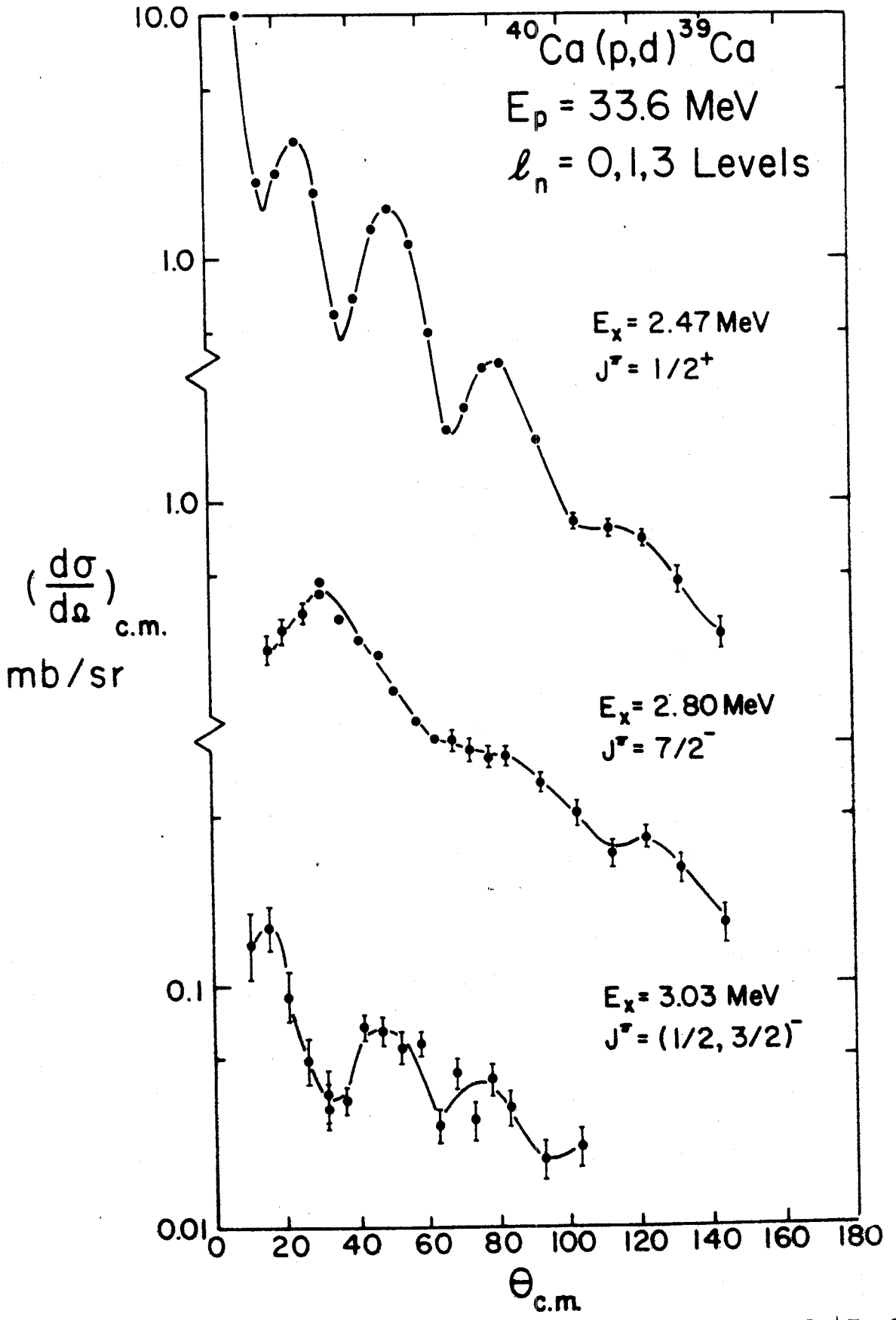

Figure. 5.31. Deuteron angular distributions for the 2.47, 2.80 and 3.03 MeV levels of ^{39}Ca from the ^{40}Ca(p,d)^{39}Ca reaction.

2.47 MeV level corresponds to a neutron pick-up from the $2s_{1/2}$ shell and thus has $J^{\pi}=1/2^{+}$. The shape of the distribution for the 2.80 MeV level is very similar to that for the transition to the 3.19 MeV level in ^{35}Ar (Sec. 5.5.1), which corresponds to an $\ell_n=3$ pick-up. Therefore, configuration mixing of the form $[d_{3/2}]^{-2}\,[f_{7/2}]^{2}$ is apparent in the ^{40}Ca ground state, in qualitative agreement with the results of Ref. G165 (b).

The 3.03 MeV level has been variously quoted as corresponding to $\ell_n=1$ and $\ell_n=2$ neutron pick-ups in $^{40}Ca(^{3}He,\alpha)^{39}Ca$ reactions (C165, B065), while the mirror level appears to be excited by an $\ell_p=1$ pick-up in the $^{40}Ca(d,\,^{3}He)^{39}K$ reaction (Hi67). The present results indicate thatthis level corresponds to an $\ell_n=1$ pick-up and has $J^{\pi}=(1/2,\,3/2)^{-}$, in agreement with Refs. C165 and Hi67. Even though the statistics are poor, the angular distribution seems to be peaked at $\theta_{c.m.}\approx 15^{\circ}$, while the forward maxima of the $\ell_n=2$ distributions are peaked at 20° to 25° at this bombarding energy. These results indicate that there is some configuration mixing with the 2p shell as well as the $f_{7/2}$ shell in the ^{40}Ca ground state. The strengths of these admixtures are given in Chapter 6.

Since there is no apparent evidence for rotational bands at low excitation energies in the ^{39}Ca

level structure, an interpretation of these levels in terms of the Nilsson model seems meaningless. The strong excitation of the $3/2^+$(g.s.) and $1/2^+$ (2.47 MeV) levels is in accordance with spherical shell model predictions.

5.6.2 J-dependence

The J-dependence in the angular distributions for the 0.00 ($3/2^+$), 5.13 ($5/2^+$) and 6.15 MeV ($5/2^+$) levels in ^{39}Ca (Fig. 5.30) is very similar to that observed in the ^{36}Ar(p,d)^{35}Ar and ^{32}S(p,d)^{31}S reactions (Secs. 5.4.2, 5.5.2). The spin assignment $J^\pi=(5/2)^+$ to the 5.13 and 6.15 MeV levels was partially based on this similarity.

5.6.3 Summary

A summary of the excitation energies, spins and parities of the ^{39}Ca levels observed in the ^{40}Ca(p,d)^{39}Ca reaction is shown in Fig. 5.32. The energy measurements are in agreement with those of Refs. Gl65 (b) and En62, with an experimental error of about $\pm$20 keV.

The level order and strengths of the levels excited in the (p,d) reaction indicate that the ^{40}Ca ground state is probably less deformed than the other nuclei studied. However, the presence of 1f and 2p shell admixtures is also evident.

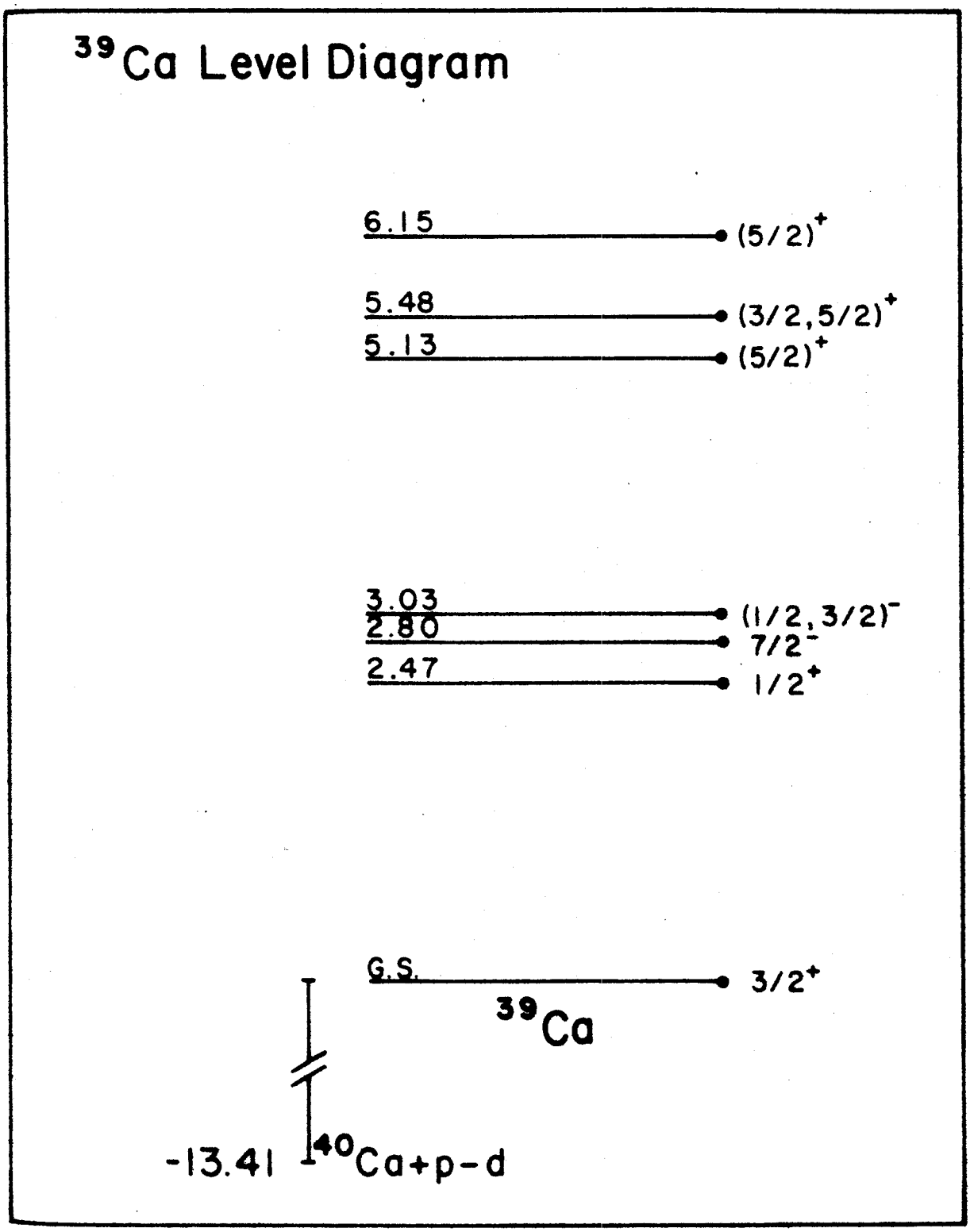

Figure 5.32. ^{39}Ca levels observed in the $^{40}Ca(p,d)^{39}Ca$ reaction. Angular distributions were measured for all levels shown.

5.7 Summary of Experimental Results

The excitation of hole states in 2s-1d shell nuclei via the (p,d) reaction has shown that the configuration mixing of shell model states is appreciable in the ground state wave functions of all the target nuclei investigated. The strong coupling rotational model seems to qualitatively explain some of the level structure of ^{23}Mg, ^{31}S and ^{35}Ar. An interpretation of the level order of ^{27}Si in terms of rotational bands is not obvious. The doubly magic ^{40}Ca nucleus, although apparently more spherical than the others, contains admixtures with both the 1f and 2p shells.

The J-dependence observed in the forward angles of the ℓ_n=2 angular distributions seems to follow a systematic trend through the 2s-1d shell. The forward maxima of the $3/2^+$ angular distributions occur at smaller angles than the maxima of the $5/2^+$ distributions for (p,d) reactions on ^{40}Ca, ^{36}Ar and ^{32}S, while the opposite effect is observed in the ^{24}Mg(p,d)^{23}Mg reaction. The J-dependence is slight in the ^{28}Si(p,d)^{27}Si reaction. Since the quadrupole deformation changes sign in the mass region A≈28 (Mu67, Cr66), it appears there may be some correlation between J-dependence and the nature of the nuclear deformation. The effects for A>28 are similar to those observed in other pick-up and stripping

reactions in the 1f and 2p shells (Wh66, Sh65, Le64, G165 (a)). The J-dependence at large angles appears to follow no definite pattern. For $\theta_{c.m.} \lesssim 90°$, all of the $5/2^+$ distributions are very similar in shape, while the $3/2^+$ distributions sometimes undergo very distinct changes from nucleus to nucleus. The usefulness of J-dependence as a spectroscopic tool has been demonstrated by the assignment of spins to levels in ^{31}S, ^{35}Ar and ^{39}Ca.

The experimental results for J-dependence have been summarized by plotting the difference in positions of the forward maxima of 3/2 and 5/2 distributions versus mass number (Fig. 5.33). The vertical axis is in terms of the momentum transferred to the residual nucleus, which reduces whatever phase differences that may arise from the two levels of a given pair having different reaction Q-values. (The differential cross-section for each of these levels is plotted versus momentum transfer in Chapter 6.) The $3/2^+$ and $5/2^+$ distributions represented correspond to the level of each respective spin having the lowest excitation energy. A DWBA analysis of J-dependence and the extraction of spectroscopic factors to provide quantitative information on configuration mixing is carried out in Chapter 6.

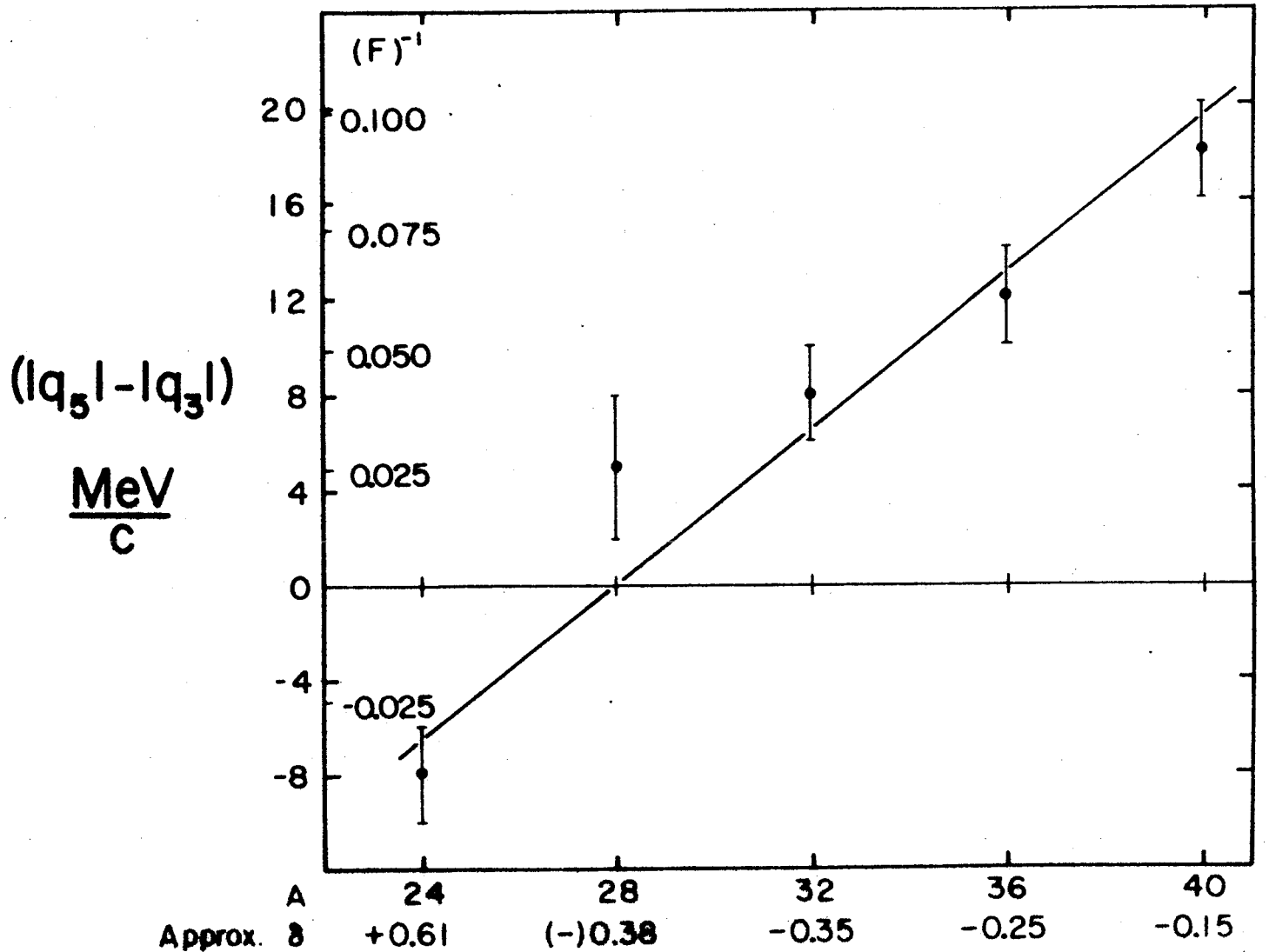

gure 5.33. Summary of experimental results for forward angle J-dependence. $|q_5|$ ($|q_3|$) is the momentum ansfer for the forward maximum of a $5/2^+$ ($3/2^+$) distribution. Values for the nuclear deformation δ e obtained from Refs. St65 and Sn67. An estimate of error is shown, and a straight line is drawn for

Chapter 6

Analysis with the Distorted Wave Born Approximation and Comparison to Theory

The experimental (p,d) angular distributions discussed in Chapter 5 were analyzed in the distorted wave Born approximation (DWBA) with respect to J-dependence and the calculation of spectroscopic factors. The calculations were performed with the Macefield computer code in the zero range approximation. The optical model parameters used in this analysis are discussed in Sec. 6.1; the results are presented in Secs. 6.2 and 6.3.

6.1 Optical Model Parameters

The optical model parameters used to generate the incident channel wave functions for the DWBA calculations were obtained from $^{26}Mg(p,p)^{26}Mg$ and $^{36}Ar(p,p)^{36}Ar$ elastic scattering experiments at 33.6 MeV bombarding energy. A best fit to the angular distributions was obtained by varying the parameters in an optical potential with surface absorption,

$$V(r) = -V_0 f(x) - i 4 a_I \frac{W}{r} \left| \frac{d}{dr} f(x') \right| - V_{coul}(r)$$

Eq. 6.1

where f(x) is the Woods-Saxon form factor:

$$f(x) = 1/(1+e^{x})$$

$$x = (r - r_0 A^{1/3})/a_0, \quad x' = (r - r_I A^{1/3})/a_I$$

Eq. 6.2

The optical model search program ABACUS (Au62) was used to obtain the fits to the data shown in Figs. 6.1 and 6.2. No spin-orbit interaction was included, since the DWBA code was not equipped to perform a spin-orbit calculation. It is seen that the fits are still quite good, especially for the ^{36}Ar data (Fig. 6.1). The fit to the ^{26}Mg data with the ^{36}Ar parameters and the fit obtained in the search on ^{26}Mg are shown in Fig. 6.2. As can be seen from Table 1, the parameters are very similar for the two nuclei. It was therefore assumed that the basic optical parameters are reasonably constant with mass number in the 2s-1d shell, and the ^{26}Mg parameters were used in the DWBA calculations for the (p,d) reaction ^{24}Mg and ^{28}Si while the ^{36}Ar parameters were used for ^{32}S, ^{36}Ar and ^{40}Ca.

Deuteron optical parameters have been obtained by Perey and Perey (Pe63, Pe66) for Ca and Mg nuclei at various bombarding energies, and by Cowley, et. al. (Co66) for ^{27}Al and ^{32}S targets at 15.8 MeV bombarding energy. An attempt to fit a (p,d) angular distribution was made with each set of parameters but only those obtained by Ref. Co66 for ^{32}S resulted in reasonable

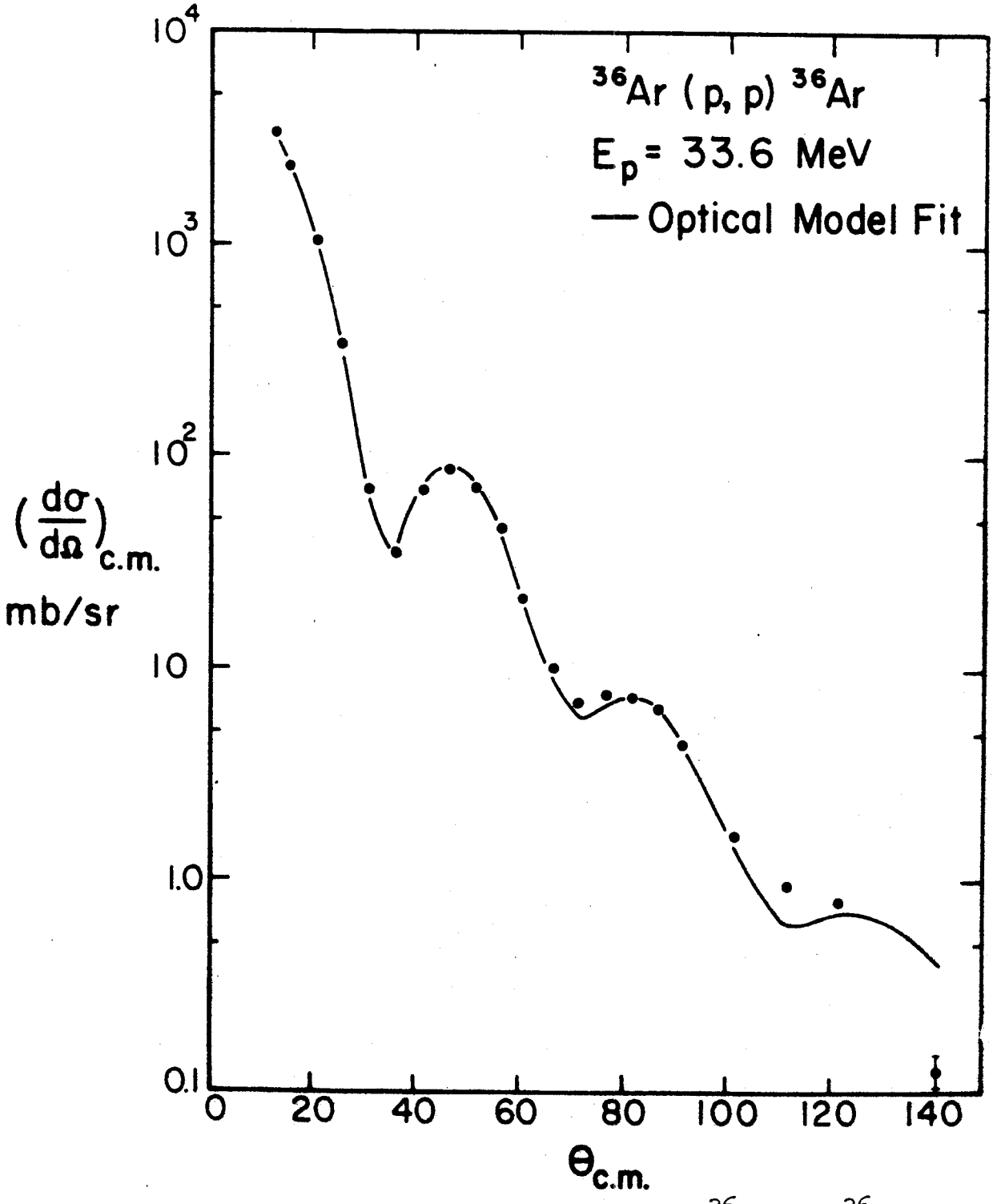

Figure 6.1. Optical model fit to $^{36}Ar(p,p)^{36}Ar$ elastic scattering data. The parameters are listed in Table 1.

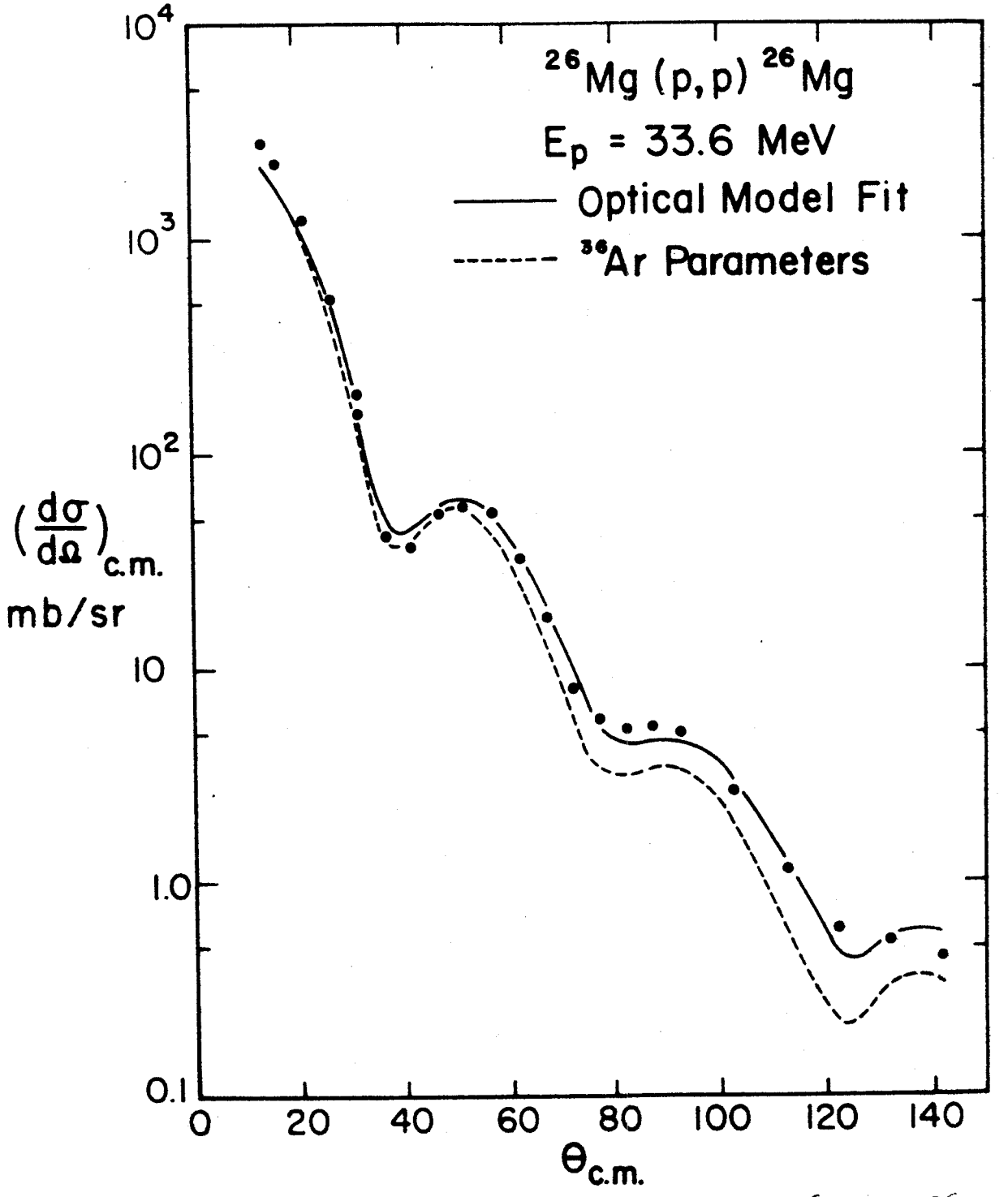

Figure 6.2. Optical model fits to the ^{26}Mg(p,p)^{26}Mg elastic scattering data with ^{36}Ar and ^{26}Mg parameters. The parameters are listed in Table 1.

Table 1: Optical Model Parameters for DWBA Analysis

	V_o(MeV)	W(MeV)	r_o(F.)	r_I(F.)	r_c(F.)	a_o(F.)	a_I(F.)	Target A	Source
Protons	49.8	6.50	1.16	1.16	1.16	0.64	0.64	24,28	^{26}Mg(p,p)
	47.1	6.87	1.18	1.18	1.18	0.66	0.66	32,36,40	^{36}Ar(p,p)
Deuterons	90.0	25.0[a]	1.25	1.30	1.30	0.62	0.58	24-40	Ref. Co66

a) For A=24, W=35 MeV.

DWBA fits to the data. These parameters are also listed in Table 1 and were used for all the targets in this work. An imaginary surface well depth (W) of 25 MeV resulted in slightly better fits than the depth of 20 MeV obtained from the elastic scattering. It was necessary to further increase this depth to 35 MeV in order to obtain reasonable fits to the data from the ^{24}Mg $(p,d)^{23}Mg$ reaction.

6.2 DWBA Analysis of J-dependence

It was observed experimentally (Chapter 5) that the J-dependence in the ℓ_n=2 angular distributions is quite pronounced in many cases. An attempt is made here to obtain DWBA fits to the forward maxima of the $3/2^+$ and $5/2^+$ angular distributions by using different radii for the neutron well. This procedure has been suggested by Pinkston and Satchler (Pi65). The Woods-Saxon potential

$$V(r) = -V_0 / \left[1 + \exp\left(\frac{r - r_{0_n} A^{1/3}}{a_n} \right) \right]$$

Eq. 6.3

was used, where the depth V_0 is determined by the neutron binding energy. As was mentioned earlier, we were unable to include spin-orbit effects. Also, it was seen in Chapter 3 that a spin-orbit potential in the neutron well predicts an effect that is generally opposite to the observed J-dependence at the forward angles.

The radius corresponding to the pick-up of a $d_{5/2}$

neutron was kept constant at 3.79 F. $=1.25(28)^{1/3}$ F. for all targets having A≥28. This effectively assumes a ^{28}Si core that does not change in physical size. The radius parameter r_{o_n} was then varied in an attempt to obtain a DWBA fit to the positions of the forward maximum in a $J^{\pi} = 3/2^+$ angular distribution for each nucleus, and to simultaneously fit the slope following the forward maximum. The diffuseness (a_n) was kept constant at 0.65 F. for all cases shown here, except for the fit to the $3/2^+$ distribution in ^{31}S (See Sec. 6.2.3). It was observed during this analysis that changes in diffuseness produce effects similar to changes in radius in the DWBA calculation.

A pair of levels from each nucleus, one having $J^{\pi} = 3/2^+$ and one $5/2^+$, was selected for this analysis. The experimentally observed effects are discussed in more detail in Chapter 5. The strongly excited level corresponding to the lowest excitation energy was chosen for each spin, and the differential cross-sections of these levels are plotted versus the momentum transfer $|\underline{q}|$ in Figs. 6.3 - 6.7. The $5/2^+$ distributions always appear at the top of the figure, and are renormalized as indicated. A momentum transfer of 300 MeV/c≈1.5 F^{-1} corresponds to a center of mass angle of approximately 70°, while the forward maxima occur at $\theta_{c.m.} \approx 20° - 25°$. DWBA fits to the data, which are also shown, are discussed below.

6.2.1 $^{40}Ca(p,d)^{39}Ca$

Figure 6.3 shows DWBA fits to the distributions from the ground ($3/2^+$) and 5.13 MeV ($5/2^+$) levels of ^{39}Ca. The neutron well radius parameter of 1.11 F. for the J= 5/2 calculation arises from the assumption of a constant $d_{5/2}$ radius ($R_{5/2}$=3.79 F.), and seems to give a reasonable fit to the data. As is shown by the dashed curve, this same radius does not result in a good fit to the forward maximum of the ground state ($3/2^+$) distribution. A larger radius (r_{o_n} =1.35 F.) predicts the oscillatory structure of the J=3/2 distribution more accurately for $|q| \lesssim 1.2$ F.$^{-1}$ but it appears that the general flattening of the $3/2^+$ distribution for larger values of $|q|$ cannot be accounted for by a simple change in radius.

6.2.2 $^{36}Ar(p,d)^{35}Ar$

The J-dependence observed in the distributions for the ground ($3/2^+$) and 2.95 MeV ($5/2^+$) levels of ^{35}Ar (Fig. 6.4) is very similar to that from the $^{40}Ca(p,d)^{39}Ca$ reaction, and similar neutron parameters were used in the DWBA calculation with about the same degree of success. The assumed $d_{5/2}$ radius of 3.79 F. corresponds to an r_{o_n} of 1.15 F., while the r_{o_n} for J=3/2 (1.35 F.) is the same as that used to fit the ^{39}Ca ground state distribution.

6.2.3 $^{32}S(p,d)^{31}S$

As was described earlier (Chapter 5), the J-depend-

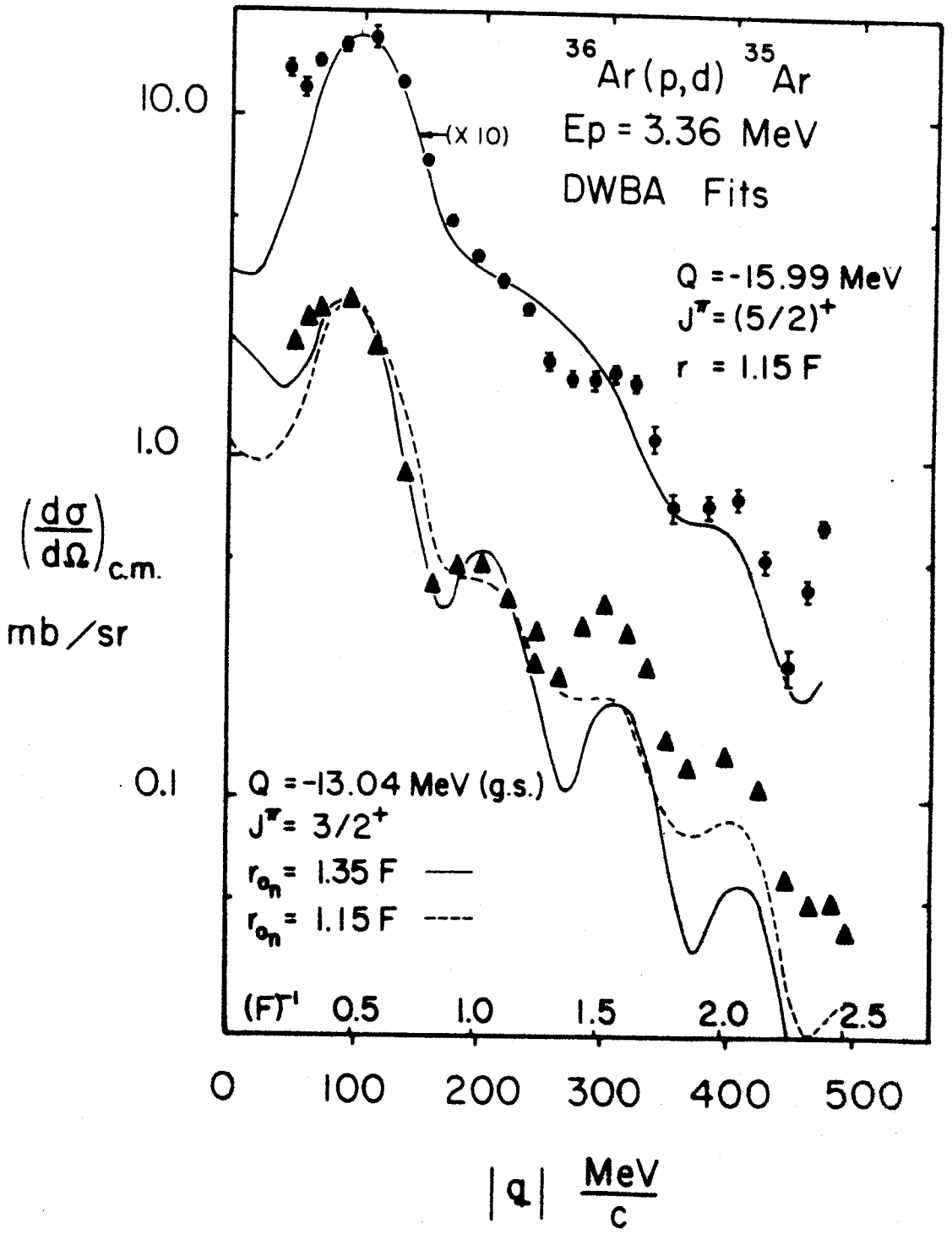

Figure 6.4. DWBA fits to the ℓ_n=2 J-dependence for the 2.95 ($5/2^+$) and 0.00 MeV ($3/2^+$) levels of ^{35}Ar excited in the ^{36}Ar(p,d)^{35}Ar reaction.

ence for the 2.23 MeV ($5/2^+$) and 1.24 MeV ($3/2^+$) levels of ^{31}S is very pronounced. The DWBA fits to the data for these levels are shown in Fig. 6.5, where it is seen that the fit to the $J^\pi=5/2^+$ distribution is quite good. The $3/2^+$ distribution drops much more rapidly from the forward maximum than the $5/2^+$ data, and this is not reproduced by using the assumed $d_{5/2}$ neutron well radius (r_{o_n}=1.20 F.) in the DWBA calculation. The radius parameter was increased to 1.65 F. and the diffuseness to 0.75 F. in order to fit the data for $|\underline{q}| \lesssim 0.8$ F.$^{-1}$; however, this resulted in a wrong prediction for the position of the second maximum at $|\underline{q}| \sim 0.9$ F.$^{-1}$. A calculation where r_{o_n}=1.75 F. and a_n=0.65 F. (not shown) fits the forward angles equally well but results in an even worse prediction for the second maximum.

6.2.4 $^{28}Si(p,d)^{27}Si$

The distributions for the ground ($5/2^+$) and 0.95 MeV ($3/2^+$) levels of ^{27}Si are shown in Fig. 6.6 where it is observed that the J-dependence is relatively weak. The position of the forward maximum of the $3/2^+$ distribution appears to occur at a slightly smaller $|\underline{q}|$ than the $5/2^+$ maximum. However, the slope following the maximum is, if anything, less steep for J=3/2 than for J=5/2. These two effects compete when the neutron radius or diffuseness is varied in the distorted wave calculation, so no variations were made in this case. The DWBA prediction

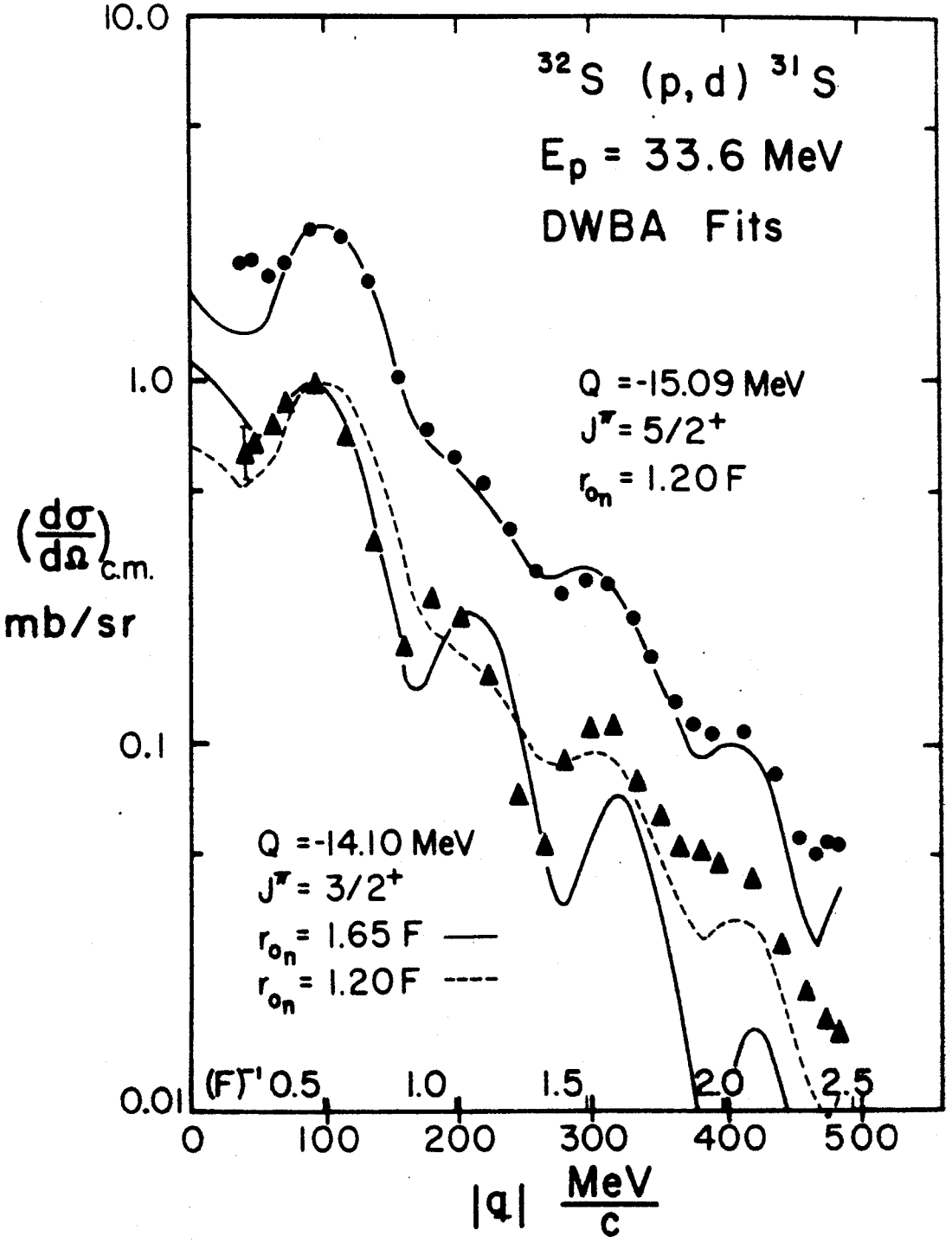

Figure 6.5. DWBA fits to the ℓ_n=2 J-dependence for the 2.23 ($5/2^+$) and 1.24 MeV ($3/2^+$) levels of ^{31}S excited in the $^{32}S(p,d)^{31}S$ reaction.

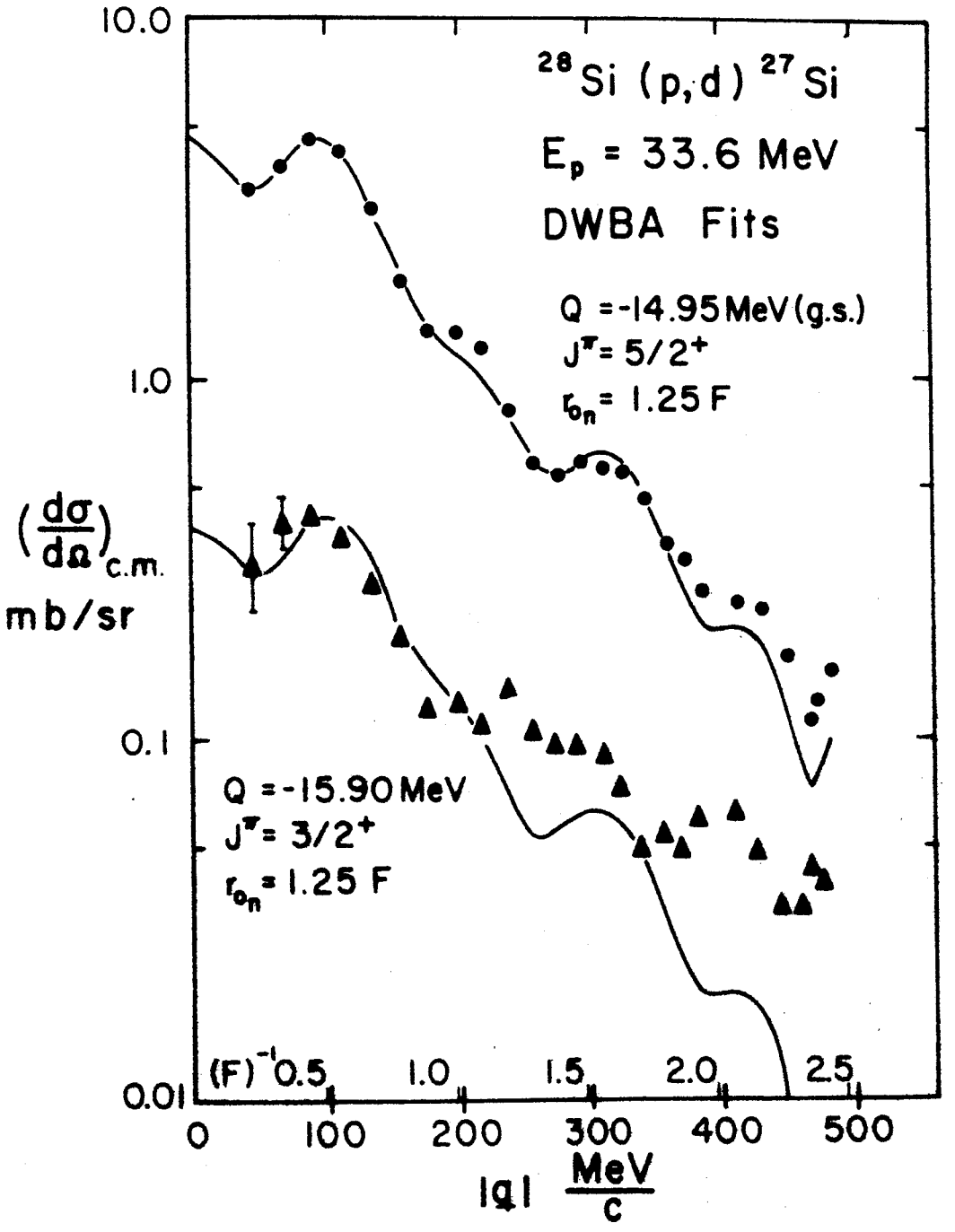

Figure 6.6. DWBA fits to the ℓ_n=2 J-dependence for the 0.00 ($5/2^+$) and 0.952 ($3/2^+$) MeV levels of ^{27}Si excited in the ^{28}Si(p,d)^{27}Si reaction.

is shown normalized to the data for both levels, and is in excellent agreement with the ground state ($5/2^+$) distribution.

6.2.5 $^{24}Mg(p,d)^{23}Mg$

As was seen in Chapter 5, the experimentally observed J-dependence effects in the distributions for the ground ($3/2^+$) and 0.45 MeV ($5/2^+$) levels of ^{23}Mg is generally opposite to that observed in the (p,d) reaction on most of the other nuclei studied. The DWBA fits to these distributions are shown in Fig. 6.7, and the calculations were made with an imaginary deuteron well depth of 35 MeV. A depth of 25 MeV, which was used for all of the other nuclei, resulted in a curve having much less structure and no relative minimum for small $|\frac{Q}{b}|$. Also, the $d_{5/2}$ radius used here is $1.15\ (24)^{1/3}=3.32$ F. instead of the 3.79 F. used for all the other nuclei. It is seen that the value for r_{o_n} of 1.15 F. is too large to yield an acceptable DWBA fit to the $3/2^+$ distribution. This was decreased to 0.75 F. to obtain a reasonable approximation to the forward maximum and overall slope of the data.

6.2.6 Summary of J-dependence Analysis

The use of different radii in the neutron form factor for $d_{3/2}$ and $d_{5/2}$ pick-ups was at least partially successful in predicting the $\ell_n=2$ J-dependence at the forward angles. It must be emphasized however, that this analysis serves only to illustrate the extent to which the radius

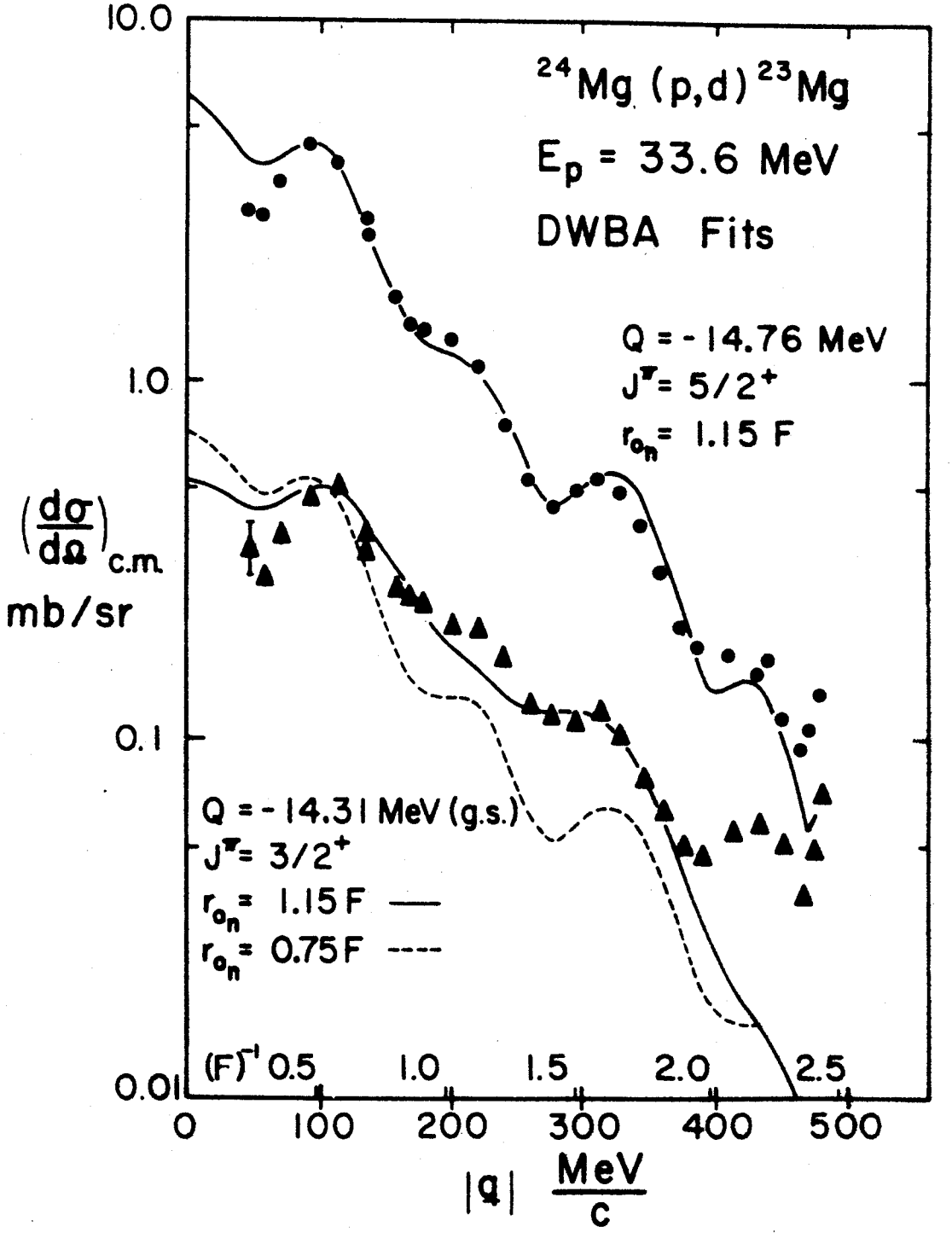

Figure 6.7. DWBA fits to the ℓ_n=2 J-dependence for the 0.45 (5/2$^+$) and 0.00 (3/2$^+$) MeV levels of ^{23}Mg excited in the ^{24}Mg(p,d)^{23}Mg reaction.

must be changed. The results are summarized in Table 2, where $R_{3/2}$ and $R_{5/2}$ correspond to $r_{o_n} A^{1/3}$ for $d_{3/2}$ and $d_{5/2}$ pick-ups respectively. The radial change is quite large for most of the targets studied and, as can be seen from the ratio $\sigma(R_{3/2})/\sigma(R_{5/2})$ in Table 2, a large change in radius results in a large change in the magnitude of the calculated DWBA cross-section. This gives rise to problems in extracting absolute spectroscopic factors, as will be seen in Sec. 6.3.

It is interesting to note however, that the ratio of the $d_{3/2}$ radius to the $d_{5/2}$ radius ($R_{3/2}/R_{5/2}$) is in general closer to unity than the ratio of the semi-axes of the nuclear ellipsoid ($R(\pi/2,\delta)/R(0,\delta)$) if one assumes reasonable values for the deformation parameter δ (Table 2)*. The only exception to this is the case of ^{40}Ca.

The effect of using a constant radius for a $d_{5/2}$ neutron is summarized in Figure 6.8, which shows a comparison of the DWBA fits to the $5/2^+$ angular distributions for $R_{5/2}$=3.79 F. and $1.25A^{1/3}$ F. The fits to the distributions for all the levels are reasonable at forward angles with the smaller radius (3.79 F.), while the predictions for a radius of $1.25A^{1/3}$ F. is in less agreement with the data as A increases. The effect is not large however, and the quality of the DWBA fits for $R_{5/2}$=3.79 F.

---

*The radii $R(\theta,\delta)$ in Table 2 were calculated from the nuclear surface formula given in Chapter 2 (Eqs. 2.15, 2.48 and 2.51).

Table 2: Summary of Neutron Parameters for DWBA Analysis of J-dependence

Target	a_{o_n}(F.)	$R_{3/2}$(F.)	$R_{5/2}$(F.)	$R_{3/2}/R_{5/2}$	δ[a]	$\frac{R(\frac{3}{2},\delta)}{R(0,\delta)}$	$\frac{\sigma(R_{3/2})}{\sigma(R_{5/2})}$
^{24}Mg	0.65	2.16	3.32	0.65	+0.61	0.55	0.5
^{28}Si	0.65	3.79	3.79	1.00	-0.38	1.51	1.0
^{32}S	0.65	5.55	3.79	1.46	-0.35	1.46	5.0
	0.75	5.23	(3.79)	(1.37)			
^{36}Ar	0.65	4.46	3.79	1.17	-0.25[b]	1.30	1.7
^{40}Ca	0.65	4.62	3.79	1.22	-0.15[c]	1.17	1.9

---

a) Values of δ are from Ref. St65 unless otherwise noted.

b) Ref. Sn67

c) Assumed Value

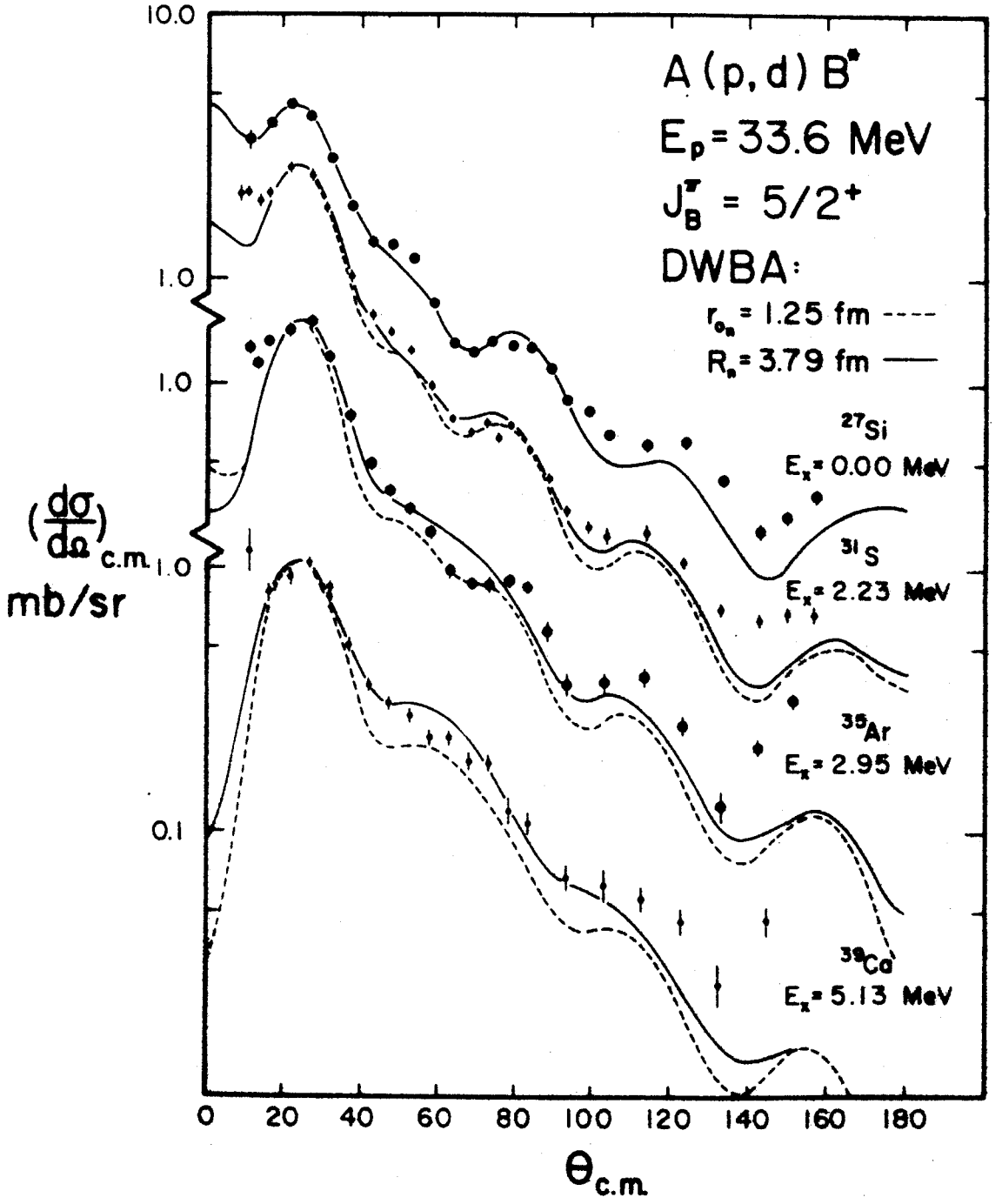

Figure 6.8. DWBA fits to $J^{\pi}=5/2^{+}$ angular distributions for levels excited in the (p,d) reaction on ^{28}Si, ^{32}S, ^{36}Ar and ^{40}Ca. The DWBA predictions for a constant total neutron well radius (3.79 F.) and a constant well radius parameter (1.25 F.) are represented by solid and dashed curves, respectively.

is not the same for the distributions of all the nuclei at large angles. It appears that more experimental information and more sophisticated DWBA techniques are needed before a definite conclusion can be drawn about the validity of a constant radius for closed shells. A similar situation exists for the theoretical explanation of J-dependence.

6.3 DWBA Spectroscopic Factors

The (p,d) spectroscopic factors were calculated using the optical model parameters mentioned earlier (Sec. 6.1). A zero range parameter of 1.5 was used to give approximately the same results as a finite range calculation (Sa64 and Chapter 3). The neutron parameters were chosen from those used for the J-dependence analysis (Table 2), and DWBA results for both neutron well radii are presented for some of the levels in ^{31}S, ^{35}Ar and ^{39}Ca.

Although the DWBA calculations resulted in quite satisfactory fits to the ℓ_n=2 data (especially the $5/2^+$ distributions), the predictions for the other ℓ_n values were less appealing. Figure 6.9 shows DWBA fits to the data corresponding to 1d, 2s, 1p and 2p neutron transfers in the $^{28}Si(p,d)^{27}Si$ reaction and the fit to the ℓ_n=3 distribution in the $^{40}Ca(p,d)^{39}Ca$ reaction. The spectroscopic factors (S_E) were obtained from the ratio of the experimental angular distribution to the calcu-

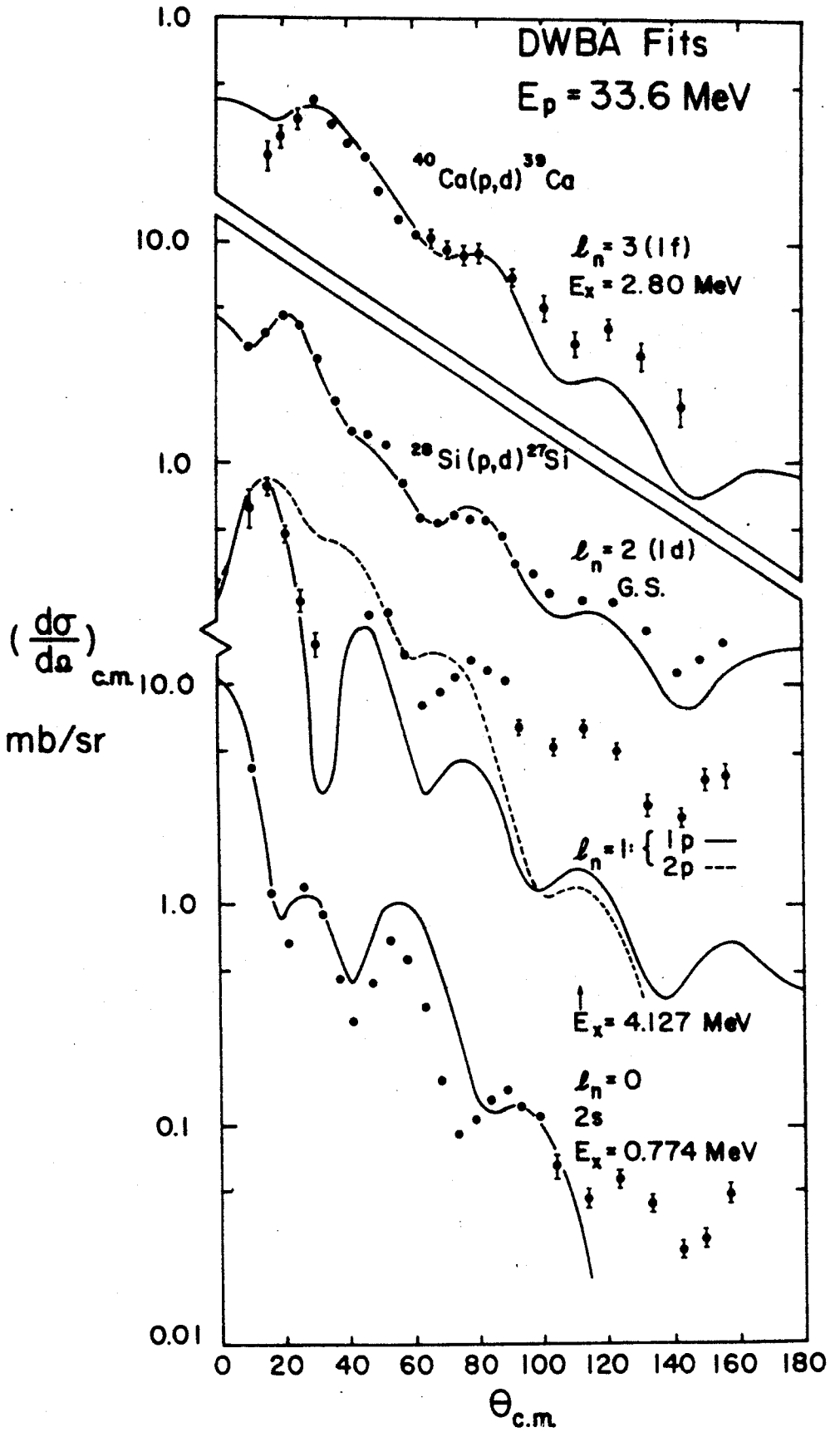

Figure 6.9. DWBA fits to deuteron angular distributions for different values of ℓ_n. Fits for the 2.80 MeV level of ^{39}Ca (ℓ_n=3) and the 0.00 (ℓ_n=2), 4.127 (ℓ_n=1) and 0.774 MeV (ℓ_n=0) levels of ^{27}Si are shown.

lated cross-section at the forward maximum for ℓ_n=1, 2 and 3. This could not be done with the ℓ_n=0 distributions since the forward maxima occur at zero degrees. The values of S_E at some of the forward angle data points and at the first relative maximum ($\theta_{c.m.} \approx 25^\circ$) were averaged to obtain the value for each ℓ_n=0 pick-up. The error is estimated to be 20% - 30% for the ℓ_n=2 spectroscopic factors obtained from the (p,d) reactions on ^{28}Si, ^{32}S, ^{36}Ar and ^{40}Ca, and is probably larger for the other ℓ_n values. The errors in the results from the $^{24}Mg(p,d)^{23}Mg$ reaction are probably very large for all values of ℓ_n.

The results for each nucleus are presented in Tables 3 through 7 where comparisons are made to the predictions of the Nilsson model in some cases. A Nilsson diagram is given in Fig. 5.1 for reference. The theoretical spectroscopic factors were obtained from the wave functions of Chi (Ch66), who has listed the coefficients of fractional parentage for various deformations ($-0.3 < \delta < +0.3$). The value of δ that appeared to be most consistant with the observed level order and experimental spectroscopic factors was chosen in each case.

6.3.1 $^{24}Mg(p,d)^{23}Mg$

In terms of the Nilsson model (Fig. 5.1) the ^{24}Mg ground state should have two neutrons and two protons in each orbit through orbit 7 if the deformation is prolate. The experimental spectroscopic factors for levels

excited in the ^{24}Mg (p,d)^{23}Mg reaction are listed in Table 3 along with the calculations from Chi's wave functions. The results of shell model calculations by Wildenthal (Wi67 (a)) are also shown.

An unusually deep imaginary well (35 MeV) was required in the deuteron channel in order to obtain reasonable DWBA fits to the data (Sec. 6.1). This caused a decrease in magnitude of the calculated ℓ_n=2 cross-sections, which resulted in values for the spectroscopic factors that are unreasonably large if one assumes a closed ^{16}O core. The values of S_E for the ℓ_n=2 levels were thus renormalized such that the sum of the S_E's for the ground and 0.45 MeV levels was equal to 2. Similarly, the spectroscopic factors for the ℓ_n=1 levels were renormalized such that S_E (2.71) + S_E (3.79) = 2. Agreement with the Nilsson model is then found for the ground state rotational band (orbit 7) if one extropolates the coefficients of the fractional parentage to a value for δ of about +0.5. This is to be compared with the value of 0.61 obtained from electric quadrupole transition rates (St65). The agreement is also reasonable for the 2.71 and 3.79 MeV levels if it is assumed that these levels are excited by the removal of a K=1/2 neutron from orbit 4.

Since the experimentally obtained spectroscopic factors are to be trusted only on a relative basis, the S_E values for the two $1/2^+$ levels cannot be compared

Table 3: Spectroscopic Factors for the $^{24}Mg(p,d)^{23}Mg$ Reaction

	S_E (r_{o_n} = 1.15 F.)			Theory[b] (δ = + 0.5)				Theory[c]	
E_x (MeV)	J^π	(1)	(2)[a]	J^π	K	Orbit No.	S_T	J^π	S_T
0.00	$3/2^+$	0.72	0.22	$3/2^+$	3/2	7	0.22		
0.45	$5/2^+$	5.66	1.78	$5/2^+$	3/2	7	1.78	$5/2^+$	3.2
2.35	$1/2^+$	0.20						$1/2^+$	0.3
2.71	$(1/2, 3/2)^-$	3.40 (1p) 0.80 (2p)	1.34	$1/2^-$	1/2	4	1.52		
3.79	$(1/2, 3/2)^-$	1.69 (1p) 0.38 (2p)	0.66	$3/2^-$	1/2	4	0.48		
4.37	$1/2^+$	0.10						$1/2^+$	0.0
5.32	$(3/2, 5/2)^+$	0.54	0.17						
6.02	$(1/2, 3/2)^-$	2.04 (1p) 0.44 (2p)	0.80						
9.63	$(3/2^+, 5/2^+)$	1.05	0.33						

a) Renormalized values; see text for explanation.

b) Calculated from Ref. Ch66.

c) Predictions of Ref. Wi67(a).

to that of the single level predicted by the Nilsson model. The ratio of the spectroscopic factors for the 2.35 and 4.37 MeV levels is in poor agreement with the ratio obtained from Wildenthal's calculation for levels at 1.80 and 4.81 MeV. It is also difficult to deduce the configurations of the levels at 5.32, 6.02 and 9.63 MeV on the basis of a simple rotational model, although the 5.32 MeV $(3/2, 5/2)^+$ level could belong to a K=1/2 rotational band based on the 4.37 MeV level.

Spectroscopic factors corresponding to a pick-up from the 2p shell were also calculated for the ℓ_n=1 levels and, as can be seen from Table 3, these values are smaller than those for a 1p pick-up by more than a factor of four. Therefore, it is possible to obtain reasonable values for S_E by assuming a 1p shell hole state, a 2p admixture in the target ground state, or a combination of the two. The ambiguity discussed in Chapter 5 is therefore difficult to resolve on the basis of spectroscopic strengths.

The spectroscopic factors obtained from the wave functions of Chi are generally in good agreement with the relative experimental values for low excitation energies. This assumes of course that the ℓ_n=1 levels at 2.71 and 3.79 MeV are due to 1p pick-ups. The configuration mixing giving rise to levels of higher excitation is not well explained by a simple Nilsson picture. The excitation of two $1/2^+$ levels of comparable strength

is evidence for configuration mixing of Nilsson orbits, which could be due to some of the strength of orbit 7 being shared with orbit 9 ($K^{\pi}=1/2^{+}$).

6.3.2 $^{28}Si(p,d)^{27}Si$

As was seen from the experimental data (Chapter 5) the level structure of ^{27}Si is not easily explainable in terms of a conventional rotational model. The s-d shell strength should all be contained in Nilsson orbits 5, 6 and 7 if $\delta \lesssim +0.15$ (Fig. 5.1). The spin of 5/2 for the ^{27}Si ground state indicates a prolate or spherical shape, while the excitation of the low-lying $1/2^{+}$ level (0.952 MeV) suggests an oblate shape.

As can be seen from the spectroscopic factors listed in Table 4, approximately half of the 2s-1d shell strength is contained in ground state ($d_{5/2}$) transition. The S_E of 3.45 agrees to within the estimated error of $\pm$ 20% with values of 3.9 and 3.97 obtained from $^{28}Si(d, ^{3}He)^{27}Al$ proton pick-up reactions (Wi67, Go67). This value is too large to correspond to a pick-up from a single Nilsson orbit, since each orbit can hold only two neutrons. It has been suggested (En62) that the ^{27}Al mirror nucleus has a prolate deformation where the first few excited levels correspond to a rotational band based on the K=1/2 [211] Nilsson orbit (Fig. 5.1). The excitation of the corresponding levels in ^{27}Si by a direct pick-up process (such as the (p,d) reaction)

Table 4: Spectroscopic Factors for the $^{28}Si(p,d)^{27}Si$ Reaction

E_x (MeV)	J^π	S_E (r_{o_n} = 1.25 F.)
0.00	$5/2^+$	3.45
0.774	$1/2^+$	0.64
0.952	$3/2^+$	0.34
2.647	$5/2^+$	0.47
2.90	$(3/2, 5/2)^+$	(0.81)
4.127	$(1/2, 3/2)^-$	1.20 (1p) 0.21 (2p)
4.275	$(3/2, 5/2)^+$	0.34
5.233	$(1/2, 3/2)^-$	1.67 (1p) 0.28 (2p)
6.343	$(3/2, 5/2)^+$	0.45

would then indicate configuration mixing with Nilsson orbit 9 in the ^{28}Si ground state. However, there seems to be no prolate value for δ (>0) for which the K=1/2, [211] wave functions of Chi (Cho6) are in reasonable relative agreement with the experimental values for the 0.774 ($1/2^+$), 0.952 ($3/2^+$) and 2.647 ($5/2^+$) levels (Table 4).. Since the $5/2^+$ assignment for the ^{27}Si ground state is inconsistent energy-wise with any other deformation (Fig. 5.1), it appears that no simple form of the strong coupling model can explain the results and no comparisons are made here. The large spectroscopic factor for the ground state transition is some indication that the average deformation is probably small, and that the mixing of rotational bands is extensive. It has been suggested that the ^{28}Si nucleus undergoes shape oscillations since the energy minima for the prolate and oblate solutions are nearly equal in a Hartree-Fock calculation (Mu67).

The spectroscopic factors for ℓ_n=2 levels at 2.647, 2.90 and 6.343 MeV are also shown in Table 4. Since the experimental data showed some indication that both levels are excited in the 2.90 MeV doublet, the meaning of the spectroscopic factor obtained in this case is not clear. DWBA calculations were made for the ℓ_n=1 levels at 4.127 and 5.233 MeV by assuming both 1p and 2p pick-ups. As was mentioned earlier (Sec. 6.3.1), the values of the spectroscopic factors

are of little help in determining the origin of the transferred ℓ_n=1 neutron.

6.3.3 $^{32}S(p,d)^{31}S$

The ^{32}S nucleus should have the last two neutrons in the K=1/2 [211] orbit if the deformation is not large (Fig. 5.1), and the J^π of $1/2^+$ for the ^{31}S ground state is consistent with this assumption. DWBA spectroscopic factors were measured for the transitions to seven levels of ^{31}S and are shown in Table 5. Values of 0.94 and 0.18 were obtained for the 1.24 MeV ($3/2^+$) level with the different neutron well parameters used in the analysis of J-dependence (Sec. 6.2.3). This is an example of the ambiguity involved in extracting ℓ_n=2 spectroscopic factors when the J-dependence is strong. It is doubtful that either of these values can be trusted; in any case the uncertainty in the strength of the $[d_{3/2}]^2$ admixture is large. The error for the other ℓ_n=2 transitions is estimated to be $\pm$ 20%, and is probably larger for the ℓ_n=0 levels.

The interpretation of the level order for the ground and first two excited levels of ^{31}S in terms of a rotational band based on Nilsson orbit 9 would seem reasonable. However, the values of the spectroscopic factors for these levels are too large for all of them to arise from the same Nilsson orbit. The wave functions of Chi are in agreement with experi-

Table 5: Spectroscopic Factors for the $^{32}S(p,d)^{31}S$ Reaction

E_x (MeV)	J^π	$S_E(r_{o_n}=1.20$ F.)	Theory[b] (δ = - 0.11)			
			J^π	K	Orbit No.	S_T
0.00	$1/2^+$	1.04	$1/2^+$	1/2	9	1.00
1.24	$3/2^+$	0.94 0.18[a]	$3/2^+$	1/2	9	0.24
			$3/2^+$	3/2	7	0.09
2.23	$5/2^+$	2.77	$5/2^+$	3/2	7	1.91
3.29	$(5/2)^+$	0.73	$5/2^+$	1/2	9	0.76
			$1/2^+$	1/2	6	0.80
			$3/2^+$	1/2	6	0.02
4.09	$5/2^+$	0.86	$5/2^+$	1/2	6	1.18
4.72	$(1/2^+)$	0.07				
7.05	$(3/2, 5/2)^+$	1.00	$5/2^+$	5/2	5	2.00

a) r_{o_n} = 1.65 F., a_n = 0.75 F.

b) Calculated from Ref. Ch66.

ment for the ground state strength if values for δ of approximately -0.11 or +0.14 are chosen. The spectroscopic factors predicted for δ = -0.11 are listed in Table 5, and the agreement is fair for some of the observed levels if it is assumed that the 3.29 MeV level is the $5/2^+$ member of the ground state rotational band. No conclusion can be drawn about the agreement for the 1.24 MeV $3/2^+$ level due to the pronounced J-dependence in the angular distribution. The large experimental spectroscopic factor for the 2.23 MeV level and the theoretical prediction of a second strongly excited $1/2^+$ level (which is not observed) are indications that the ground state of ^{32}S is not easily explainable in terms of a simple Nilsson picture. Recent Hartree-Fock calculations (Mu67, Ba66) predict that the ^{32}S nucleus is asymmetric.

6.3.4 $^{36}Ar(p,d)^{35}Ar$

The shell model predicts that the ^{36}Ar ground state should have a $[d_{3/2}]^2$ configuration for the last two neutrons. The DWBA spectroscopic factors for levels excited in the $^{36}Ar(p,d)^{35}Ar$ reaction were calculated for both of the neutron well radii used in the analysis of ℓ_n=2 J-dependence (Sec. 6.2.2), and are listed in Table 6. The value corresponding to the best DWBA fit for each level is denoted by an asterisk (*), except that no decision could be made for the ℓ_n=0 fits.

E_x (MeV)	J^π	S_E		Theory[a] (δ =-0.10)			
		r_{o_n}=1.15 F.	r_{o_n}=1.35 F.	J^π	K	Orbit No.	S_T
0.00	$3/2^+$	3.03	1.76*	$3/2^+$	3/2	8	1.92
1.18	$1/2^+$	1.29	1.05	$1/2^+$	1/2	9	1.06
1.70	$(5/2^+)$	<0.1		$5/2^+$	3/2	8	0.08
2.60	$(3/2)^+$	0.42	0.28*	$3/2^+$	1/2	9	0.22
				$3/2^+$	3/2	7	0.08
				$5/2^+$	1/2	9	0.72
2.95	$(5/2)^+$	2.31*	1.53	$5/2^+$	3/2	7	1.92
3.19	$7/2^-$	0.64	0.37*			(10)	
4.70	$1/2^+$	0.46	0.38	$1/2^+$	1/2	6	0.76
				$3/2^+$	1/2	6	<0.01
5.57	$(3/2, 5/2)^+$	1.77*	1.25	$5/2^+$	5/2	5	2.00
6.01	$(3/2, 5/2)^+$	1.18*	0.83	$5/2^+$	1/2	6	1.24
6.62	$1/2^+$	0.24	0.19			(11)	
6.82	$(3/2, 5/2)^+$	0.72	0.51			(11)	

* Value for radius giving best DWBA fit.

a) Calculations from Ref. Ch66.

Although approximately 12 MeV of excitation in ^{35}Ar was observed (Chapter 5), no strongly excited levels were found to exist above the 6.62 MeV level. This indicates that most of the s-d shell hole strength has been observed. It is interesting to note that the "best fit" values for ℓ_n=2 in Table 6 seem to be in best agreement with the total expected ℓ_n=2 strength (~8).

The $3/2^+$ assignment for the ^{35}Ar ground state is consistent with an oblate deformation ($\delta<0$) in the Nilsson model (Fig. 5.1), and the 1.70 MeV level is probably the $5/2^+$ member of the ground state rotational band. As was the case for the ground and first two excited levels in ^{31}S, an assumption that the 1.18 ($1/2^+$), 2.60 ($3/2^+$) and 2.95 ($5/2^+$) levels are all members of the K=1/2, [211] rotational band is inconsistent with the large spectroscopic factors observed for these levels (Table 6). The "best fit" spectroscopic factors for most of ℓ_n=2 levels are in fair agreement with the Nilsson model for δ =-0.10, if one makes the orbit assignments listed in Table 6. The agreement with experiment for the 1.18 MeV $1/2^+$ level is also quite reasonable. The missing $5/2^+$ level from orbit 7 suggests that the $d_{5/2}$ strength from orbits 7 and 9 may be combined in the 2.95 MeV level.

6.3.5 ^{40}Ca(p,d)^{39}Ca

The DWBA spectroscopic factors for levels excited

in the (p,d) reaction on the doubly magic ^{40}Ca nucleus were calculated for both of the neutron well radii used in the analysis of J-dependence (Sec. 6.2.1) and are shown in Table 7. As was the case for the $^{36}Ar(p,d)^{35}Ar$ reaction, the radius corresponding to the best DWBA fit seems to result in the most reasonable spectroscopic factor (on the basis of total strength) for $\ell_n=2$ and $\ell_n=3$. Again, the $\ell_n=0$ fit is inconclusive.

The excitation of the 2.80 MeV level ($\ell_n=3$) is an indication of configuration mixing with the $f_{7/2}$ shell. The spectroscopic factor of 0.58 is in good agreement with the value of 0.53 obtained by Bock, et. al. (Bo65) from the $^{40}Ca(^3He,\alpha)^{39}Ca$ reaction and with the result of 0.5 obtained for the excitation of the mirror level in the $^{40}Ca(d, ^3He)^{39}K$ reaction (Hi67). Glashausser, et. al. (Gl65(b)) extracted values of 0.14 and 0.28 by assuming different neutron separation energies in the $^{40}Ca(p,d)^{39}Ca$ reaction at 27.5 MeV bombarding energy. The excitation of the $\ell_n=1$ level at 3.03 MeV is assumed to be due to a 2p shell admixture with an estimated spectroscopic factor of ~0.02 as compared to a value of 0.04 - 0.05 obtained by Hiebert, et. al. (Hi67) for the mirror level in the (d, ^3He) reaction mentioned above. Both of these results are considerably smaller than the value 0.11 obtained by Cline, et. al. (Cl65) from the $^{40}Ca(^3He,\alpha)^{39}Ca$ reaction.

The spectroscopic factors for the $\ell_n=2$ levels at

Table 7: Spectroscopic Factors for the $^{40}Ca(p,d)^{39}Ca$ Reaction

E_x	J^π	S_E		S_T [a]
		$r_{o_n}=1.11$	$r_{o_n}=1.35$	
0.00	$3/2^+$	7.11	3.70*	4.00
2.47	$1/2^+$	2.31	1.82	2.00
2.80	$7/2^-$	1.04	0.58*	
3.03	$(1/2, 3/2)^-$		0.02	
5.13	$(5/2)^+$	2.08*	1.43	6.00
5.48	$(3/2, 5/2)^+$	0.97	0.67	
6.15	$(5/2)^+$	2.15*	1.48	

---

a) Shell model predictions

* Values for radius giving best DWBA fit.

5.13, 5.48 and 6.15 MeV indicate that these levels probably represent most of the $d_{5/2}$ strength, especially if the smaller neutron well radius is assumed. However, the strength obtained with a radius parameter of r_{o_n} = 1.35 F. is in agreement with the $d_{5/2}$ proton strength obtained by Ref. Hi67 in the (d, ^{3}He) reaction for the 5 - 7 MeV region of excitation in ^{39}K. It was therefore suggested (Hi67) that other $d_{5/2}$ hole states exist at higher excitation energies ($E_x > 8$ MeV). Although about 12 MeV of excitation is observed in the present work, no other strongly excited levels are found to exist above the 6.15 MeV level in ^{39}Ca (Fig. 5.28 in Chapter 5). In fact, no level structure at all appeared in the deuteron spectra for $E_x \gtrsim 9$ MeV.

As mentioned earlier (Chapter 5), the data from this experiment indicates that most of the configuration mixing occurs with higher shells, and does not lend itself to analysis in terms of the Nilsson model.

6.3.6 Summary

The DWBA spectroscopic factors obtained for the (p,d) reaction on ^{28}Si, ^{32}S, ^{36}Ar and ^{40}Ca appear to be reasonable from a shell model point of view. There is some evidence that the more trustworthy value for the ℓ_n=2 spectroscopic factors may be obtained by using the neutron well radius that was assumed in the J-dependence analysis for each respective spin. The uncertainty in

the DWBA results are still quite large, however, especially if the J-dependence is strong.

Configuration mixing of shell model states was found to exist in the ground states of all the target nuclei studied. The ^{24}Mg and ^{28}Si ground states contain mixing of the $s_{1/2}$ and $d_{3/2}$ shells, with the possibility of 2p shell admixtures as well. The major admixture in the ground state of ^{32}S appears to be a $[d_{3/2}]^2$ configuration, while the $\ell_n=3$ transitions in the (p,d) reaction on ^{36}Ar and ^{40}Ca indicate appreciable mixing with the $f_{7/2}$ shell. There is also evidence for a small $[2p]^2$ admixture in the ground state of ^{40}Ca.

The comparison of the experimentally measured spectroscopic factors with the predictions of the Nilsson model has shown that the description of 2s-1d shell nuclei in general is not so simple as one might expect from considering only the observed level order (Chapter 5). The strong excitation of low-lying $5/2^+$ levels in the (p,d) reaction is evidence for rotational band mixing in the residual nucleus, corresponding to a small deformation in the target. This effect is particularly strong in the $^{28}Si(p,d)^{27}Si$ reaction. The spectroscopic factors obtained from the Nilsson model are in fair agreement with experiment for some of the levels of ^{23}Mg and ^{35}Ar, although it is not obvious that all the Nilsson orbit assignments are meaningful. The situation is even more ambiguous for the levels of ^{31}S. The

nature of the configuration mixing in these nuclei therefore seems to be very complex, although it may still be explainable in terms of a strong coupling rotational model if band mixing is included.

Chapter 7

Summary and Conclusions

The investigation of the (p,d) reaction on N=Z nuclei in the 2s-1d shell has provided new information about the level structures of the ^{23}Mg, ^{27}Si, ^{31}S and ^{35}Ar residual nuclei, while previous results for the A=39 mirror nuclei (Hi67, G165 (b), C165) have been confirmed by the ^{40}Ca(p,d)^{39}Ca reaction. The 33.6 MeV bombarding energy and particle detection techniques have permitted the observation of 10 - 12 MeV of excitation in the residual nuclei with the interesting result that virtually all of the observed 2s-1d shell hole strength exists at excitation energies $<$8 MeV. (A possible exception to this is the 9.63 MeV level in ^{23}Mg.) It is therefore apparent that most of the 2s-1d shell hole states have been excited, the DWBA spectroscopic factors obtained here qualitatively provide an additional confirmation of this fact.

The forward angle J-dependence observed in the ℓ_n=2 angular distributions appears to vary in a systematic way with mass number (for N=Z targets) (Fig. 5.33) and may possibly be correlated with the nature of the nuclear deformation. It was noticed (Chapter 5) that the shapes of all the $5/2^+$ distributions were very similar, while the distributions for J=3/2 had a ten-

dency to vary from nucleus to nucleus. Spin assignments for levels in ^{31}S, ^{35}Ar and ^{39}Ca were suggested on this basis.

The attempts to reproduce J-dependence effects by varying the neutron well radius in distorted-wave calculations (Chapter 6) were partially successful, although very large changes were necessary in most cases. The results obtained by assuming a constant total well radius (3.79 F. = 1.25 $(28)^{1/3}$ F.) for a $d_{5/2}$ neutron pick-up are in slightly better agreement with experiment than those obtained with a constant radius parameter (r_{o_n}=1.25 F.) (Fig. 6.8). Large variations in the neutron radius parameter produce correspondingly large changes in the magnitude of the calculated DWBA cross-section and lead to uncertainties in extracting spectroscopic factors. However, there is some evidence that the radius parameter corresponding to the best DWBA fit to the data also results in the most trustworthy value for the spectroscopic factor. It is apparent from the results of this and other investigations (Le64, Sh64, Sh65, Gl65 (a), Wh66) that additional experimental information and more theoretical work are necessary to obtain an understanding of J-dependence.

Configuration mixing of shell model states in the ground state wave functions was found to be appreciable

for all the target nuclei in this study. The strong excitation of the ℓ_n=3 levels in ^{35}Ar and ^{39}Ca indicate the presence of a large $[f_{7/2}]^2$ admixture in each of these nuclei. There is also evidence for a small amount of mixing with the 2p shell in ground state of ^{40}Ca. The mixing to higher shells in the ^{32}S ground state seems to be concentrated mainly in the excitation of the $3/2^+$ level at 1.24 MeV excitation in ^{31}S. The ground state wave functions of ^{24}Mg and ^{28}Si contain admixtures with both the $2s_{1/2}$ and $1d_{3/2}$ shells.

Of particular interest is the excitation of low-lying (E_x=2.7 - 6.0 MeV) ℓ_n=1 levels in ^{23}Mg and ^{27}Si. Since proton knock-out experiments (Hi65, Ja66) and Hartree-Fock calculations (Da66) predict a 10 - 20 MeV energy separation between the 1p and 2s-1d shells, the possibility of 2p shell admixtures exists (Wi67). However, a plot of (p,d) reaction Q-values for the excitation of the first ℓ_n=1 level versus mass number (Fig. 5.14) seems to be strong evidence that these levels are 1p shell hole states. As was observed in Chapter 6, this ambiguity is not resolved by extracting spectroscopic factors, since the calculated DWBA cross-section is much larger for a 2p pick-up than a 1p pick-up.

The ordering of the first few levels in ^{23}Mg,

^{31}S and ^{35}Ar seems to be qualitatively consistent with rotational bands based on neutron holes in Nilsson orbits (Ni55 and Fig. 5.1). However, the extraction of DWBA spectroscopic factors (Chapter 6) has shown that the explanation is not nearly so simple. The large spectroscopic factors measured for the excitation of low-lying $5/2^+$ levels in ^{31}S and ^{35}Ar is an indication of considerable rotational band mixing. This effect is even more pronounced in the excitation of the ^{27}Si ground state (also $5/2^+$), where a spectroscopic factor of 3.45 was measured for that transition. The nuclear deformation is expected to be small for nuclei near closed shells, and the results from the (p,d) reaction on the doubly magic ^{40}Ca nucleus indicate that this is the case for the 2s-1d shell.

Appendix A

Calculation of (p,t) Spectroscopic Factors from the Nilsson Model*

In Chapter 2 it was seen that the Nilsson wave function for a single neutron could be expanded in terms of shell model states:

$$\psi_{\alpha_i K_n} = \sum_{j_n = K_n}^{j_{max.}} C_{j_n K_n}(\alpha_i) \, | N \ell_n j_n K_n \rangle$$

Eq. A.1

Here α_i determines the Nilsson orbit when K_n and N are given. Restricting ourselves to one value of N, we define

$$| N \ell j K \rangle \equiv a_K^{\ell j} (int.)$$

Eq. A.2

in the body-fixed (intrinsic) system.

If the symmetry requirements of the wave function are neglected, the total wave function of the target nucleus is

$$\Psi^{J_i}_{M_i K_i} = \sqrt{\frac{2J_i+1}{8\pi^2}} \, \mathcal{D}^{J_i}_{M_i K_i} \, \chi_{K_i}$$

Eq. A.3

where the total particle wave function can be written as

$$\chi_{K_i} = \prod_{p=1}^{8} \psi_{\alpha_p K_p} \, | \, Core \rangle_{intrinsic}$$

Eq. A.4

---

* The author is indebted to L. Zamick for his helpful explanation of this subject.

The wave function for the residual nucleus for a given final J is then

$$\Psi^{J}_{MK} = \sqrt{\frac{2J+1}{8\pi^2}}\, \mathcal{L}^{J}_{MK} \left[\Psi^{\dagger}_{\alpha_n K_n} \chi_{K_i} \right]_K$$

Eq. A.5

where $\Psi^{\dagger}_{\alpha_n K_n}$ is the Nilsson wave function of the neutron hole and acts as a destruction operator.

For the pick-up of a neutron having quantum numbers (ℓ_n, j_n, M_n) in the laboratory system, the observed spectroscopic factor is defined as

$$S^{J}_{K}(\alpha_n) \equiv \frac{\eta}{2J_i+1} \left| \langle \Psi^{J}_{MK} \| a^{\ell_n j_n}_{M_n}(LAB) \| \Psi^{J_i}_{M_i K_i} \rangle \right|^2$$

$$\equiv \frac{\eta(2J+1)}{2J_i+1} \left| \langle \Psi^{J}_{MK} \left| \left[a^{\ell_n j_n}_{M_n}(LAB)\, \Psi^{J_i}_{M_i K_i} \right]^{J}_{MK} \right\rangle \right|^2$$

Eq. A.6

where $\eta = 2$ for a filled Nilsson orbit. The neutron wave function in the laboratory system is related to the $a^{\ell_j}_{K}$(int.) in Eq. A.2 by

$$a^{\ell_n j_n}_{M_n}(LAB) = \sum_{\nu} \mathcal{D}^{j_n}_{M_n \nu}\, a^{\ell_n j_n}_{\nu}(int.)$$

Eq. A.7

Substituting Eqs. A.7, A.3 and A.5 in Eq. A.6 gives the result

$$S^{J}_{K}(\alpha_n) = \frac{2(2J+1)^2(2J_i+1)}{(2J_i+1)(8\pi^2)^2} \left| \sum_{\nu} \left\langle \left[\Psi^{\dagger}_{\alpha_n K_n} \chi_{K_i} \right]_K \left[a^{\ell_n j_n}_{\nu}(int) \right]_{K_i} \right\rangle \right.$$

$$\left. \times \int \mathcal{D}^{J*}_{MK}(R)\, \mathcal{L}^{j_n}_{M_n \nu}(R)\, \mathcal{D}^{J_i}_{M_i K_i}(R)\, dR \right|^2$$

Eq. A.8

The integral is (de Sh63)

$$\int \mathcal{D}^{J^*}_{MK} \mathcal{D}^{j_n}_{m_n \nu} \mathcal{D}^{J_i}_{M_i K_i} d\mathcal{R} = \frac{8\pi^2}{2J+1} (j_n J_i m_n M_i | JM)(j_n J_i \nu K_i | JK)$$

Eq. A.9

and the $a^{l_i j_n}_{\nu}$(int.) are given by the inverse of the expansion A.1:

$$a^{l_n j_n}_{\nu}(\text{int.}) = \sum_i C^{-1}_{j_n \nu}(\alpha_i) \psi_{\alpha_i \nu}$$

Eq. A.10

By orthogonality of the $\psi_{\alpha_i \nu}$ then, we see that only the term with $\nu = K$ (and $\alpha_i = \alpha_n$) is retained in the summation in Eq. A.8. Therefore, the substitution of Eqs. A.9 and A.10 in Eq. A.8 gives the result

$$S^J_K(\alpha_n) = 2 (j_n J_i M_n M_i | JM)^2 (j_n J_i K_n K_i | JK)^2 / |C^{-1}_{j\nu}(\alpha_n)|^2$$

Eq. A.11

This gives the spectroscopic factors in terms the (normalized) inverse expansion coefficients $C^{-1}_{j\nu}(\alpha_i)$, which are obtained from the given coefficients (Ch66) of Eq. A.1 by a simple relation for real, unitary matrices:

$$C^{-1} = C^T = \tilde{C}^* = \tilde{C}$$

Eq. A.12

i.e., it is just the transpose of the original matrix. If $J_i = 0$, i.e., if the target is an even-even nucleus, Eq. A.11 reduces to

$$S^J_K(\alpha_n) = 2 / |C^{-1}_{j\nu}(\alpha_n)|^2$$

Eq. A.13

This equation, together with the wave functions of Chi (Ch66), was used to calculate the theoretical spectroscopic factors given in Chapter 6.

Appendix B

Transition Amplitude for the (d,p) and (p,d) Reactions

The transition amplitude used in Chapter 3 is derived here according to the procedure of Satchler (Sa64), with notation similar to that of Glashausser (Gl65(a)). The zero range approximation is used for the direct reaction mechanism, and effects due to isospin, Coulomb phases and the Exclusion Principle are ignored for simplicity. Since the (d,p) and (p,d) reactions are time reversals of each other, the final results are simply related (To61), so the A(d,p)B stripping reaction is assumed throughout the calculation.

The expression for the transition amplitude given in Chapter 3 (Eq. 3.10) can be rewritten in the form

$$T_{dp} = J\int d\vec{r}_d \int d\vec{r}_p \, \chi_p^{-*}(\vec{k}_p, \vec{r}_p)\left[\int d\xi \, \psi_B^*(\xi, \vec{r}_{An}) V_{pn} \psi_d(\vec{r}_{np}) \psi_A(\xi)\right] \chi_d^{+}(\vec{k}_d, \vec{r}_d)$$

Eq. B.1

where J is the Jacobian of the transformation to the relative coordinates $\vec{r}_p$ and $\vec{r}_d$. The quantity in brackets, which will be referred to as $Q(\vec{r}_{pn})$, is of particular interest. It represents the matrix element of the direct interaction between the initial and final internal states, and contains all the nuclear structure information and angular momentum selection rules. ξ represents all coordinates independent of the relative displacements $\vec{r}_p$

and $\vec{r}_d$. Thus $Q(\vec{r}_{pn})$ is a function of $\vec{r}_p$ and $\vec{r}_d$ and represents an effective interaction between the elastic scattering states. This factorization property separates out the dynamics of the reaction and permits one to consider only the rotational properties of $Q(\vec{r}_{pn})$.

Introducing spins for all nuclei we have

$$Q(\vec{r}_{np}) = \int d\xi \, \psi_B^{J_B M_B^*}(\xi, \vec{r}_{nA}) \sum_p^{s_p m_p} V_{pn}(\vec{r}_{np}) \psi_d(\vec{r}_{np}) \Sigma_d^{s_d m_d} \psi_A^{J_A M_A}(\xi)$$

Eq. B.2

To evaluate this matrix element, $Q(\vec{r}_{pn})$ is expanded into terms corresponding to the transfer of a definite angular momentum $\vec{j}$ to the residual nucleus, where

$$\vec{j} = \vec{J}_B - \vec{J}_A = \vec{\ell} + \vec{s}, \quad \vec{s} = \vec{s}_d - \vec{s}_p$$

Eq. B.3

Then, using Clebsch-Gordan coefficients corresponding to this coupling, we can write

$$J Q(\vec{r}_{np}) = \sum_{\ell s_n j} i^{-\ell} G_{\ell s_n j m}(\vec{r}_d, \vec{r}_p)(-)^{s_p - m_p}(J_A j M_A, M_B - M_A | J_B M_B)$$
$$\times (s_d s_p m_d, -m_p | s_n, m_d - m_p)(\ell s_n m, m_d - m_p | j, M_B - M_A)$$

Eq. B.4

where $m = M_B - M_A + m_p - m_d$.

$G_{\ell s_n j m}(\vec{r}_d, \vec{r}_p)$ depends on the various nuclear quantum numbers, and is defined by the inverted form of this expansion. It transforms under rotation like the spher-

ical harmonic Y_ℓ^{m*} and contains the parity change of the nuclear transition which, if the deuteron D state is neglected, is $(-)^\ell$.

The value of G is determined by the reaction being considered and the interaction $V(\vec{r}_{np})$. An explicit form will be derived later, but for now it is convenient to write

$$G_{\ell s_n j, m}(\vec{r}_d, \vec{r}_p) \equiv A_{\ell s_n j} f_{\ell s_n j, m}(\vec{r}_d, \vec{r}_p)$$

Eq. B.5

where $A_{\ell s_n j}$ is a spectroscopic coefficient and $f_{\ell s_n j, m}(\vec{r}_d, \vec{r}_p)$ is an interaction form factor. The zero-range approximation assumes that the neutron and proton coordinates coincide at the point of interaction. In this case $f_{\ell s_n j, m}(\vec{r}_d, \vec{r}_p)$ can be written

$$f^{\circ}_{\ell s_n j, m}(\vec{r}_d, \vec{r}_p) = \delta\left(\vec{r}_p - \frac{A}{B}\vec{r}_d\right) \int f_{\ell s_n j, m}\left(\vec{s} + \frac{A}{B}\vec{r}_d, \vec{r}_d\right) d\vec{s}$$

$$\equiv F_{\ell s_n j}(r_d)\, Y_\ell^{m*}(\theta_d, \phi_d)\, \delta\left(\vec{r}_p - \frac{A}{B}\vec{r}_d\right)$$

Eq. B.6

where $F_{\ell s_n j}(r_d)$ is a scalar radial form factor, and A and B refer to the respective nuclear masses. This makes G (and thus $Q(\vec{r}_{np})$) proportional to a delta function, so that the six-dimensional integral for T_{dp} (Eq. B.1) is reduced to three dimensions, and is much easier to evaluate. Using Equations B.6, B.5 and B.4 in Eq. B.1 and ignoring spin-orbit coupling in the elastic scattering wave functions χ_i, we obtain

$$T_{dp}^{m_d M_A}{}_{m_p M_B} = \sum_{\ell s_n j} \sqrt{2j+1}\, A_{\ell s_n j}\, (J_A\, j\, M_A, M_B - M_A \,|\, J_B\, M_B)\, \beta_{s_n j}^{\ell m m_d m_p}$$

Eq. B.7

where

$$\beta_{s_n j}^{\ell m m_d m_p} = (-)^{s_p - m_p} \sqrt{\frac{2\ell+1}{2j+1}}\, (\ell s_n m, m_d - m_p \,|\, j, m - m_p + m_d)\, (s_d s_p\, m_d, -m_p \,|\, s_n, m_d - m_p)\, \beta_{s_n j}^{\ell m}$$

Eq. B.8

and

$$\beta_{s_n j}^{\ell m} = \frac{i^{-\ell}}{\sqrt{2\ell+1}} \int d\vec{r}_d\, \chi_p^{-*}\!\left(\vec{k}_p, \tfrac{A}{B}\vec{r}_d\right) F_{\ell s_n j}(\vec{r}_d)\, Y_\ell^{m*}(\theta_d, \phi_d)\, \chi_d^{+}(\vec{k}_d, \vec{r}_d)$$

Eq. B.9

Equations B.8 and B.9 have the property

$$\sum_{m_p m_d} \left| \beta_{s_n j}^{\ell m m_p m_d} \right|^2 = \left| \beta_{s_n j}^{\ell m} \right|^2$$

Eq. B.10

The differential cross-section is then given by

$$\frac{d\sigma}{d\Omega} = \frac{\mu_p \mu_d}{(2\pi\hbar^2)^2} \frac{k_p}{k_d} \frac{1}{(2J_A+1)(2s_d+1)} \sum_{\substack{M_A m_d \\ M_B m_p}} \left| T_{dp}^{m_d M_A}{}_{m_p M_B} \right|^2$$

Eq. B.11

In terms of the spectroscopic coefficient $A_{\ell s_n j}$,

$$\frac{d\sigma(\theta)}{d\Omega} = \frac{2J_B+1}{2J_A+1} \sum_{\ell s_n j} \frac{|A_{\ell s_n j}|^2}{2s_d+1}\, \sigma_{\ell s_n j}(\theta)_{dp}$$

Eq. B.12

where, making use of Eq. B.10, the "reduced" cross-section is

$$\sigma_{\ell s_n j}(\theta)_{d_p} = \frac{\mu_d \mu_p}{(2\pi\hbar^2)^2} \frac{k_p}{k_d} \sum_m |\beta_{s_n j}^{\ell m}|^2$$

Eq. B.13

Before these cross-sections can be calculated, an explicit expression for the reduced amplitude β is needed. This is done by expanding the distorted waves χ into partial waves, and is discussed in Ref. Sa64.

An explicit (d,p) form for the $G_{\ell s_n j m}(\vec{r}_d, \vec{r}_p)$ in Eq. B.4 will now be derived. Consider first an expansion of the wave function of the residual nucleus in terms of the eigenstates of the target:

$$\psi_B^{J_B M_B}(\xi, \vec{r}_{nA}) = \sum_{\substack{j\mu \\ J_A' M_A'}} \alpha_{\ell j} \psi_A^{J_A' M_A'}(\xi_A) \psi_n^{\ell j \mu}(\vec{r}_{nA}, \xi) (J_A' j M_A' \mu | J_B M_B)$$

Eq. B.14

Here, $\alpha_{\ell j}$ is a fractional parentage coefficient and is the wave function for a neutron in an (ℓ, j) orbit. This wave function can be expanded in terms of the spherical harmonics of the $\vec{r}_{nA}$ system:

$$\psi_n^{\ell j \mu}(\vec{r}_{nA}, \xi_n) = \sum_{m_n} i^{\ell} Y_\ell^m(\theta_{nA}, \phi_{nA}) \mathcal{U}_{\ell j}(r_{nA}) \Sigma_n^{s_n m_n}(\xi_n) (\ell s_n m m_n | j \mu)$$

Eq. B.15

where $m_n = \mu - m$ is the neutron spin projection, and ξ_n involves only the neutron spin coordinates. Since the internal coordinates of nucleus B and the neutron have

been separated from r_{nA} in Equations B.14 and B.15, the integral for $Q(\vec{r}_{np})$ (Eq. B.2) may be evaluated. Rewriting Eq. B.2 explicitly and assuming V_{np} is a central potential we have

$$Q(\vec{r}_{np}) = \int d\xi_A d\xi_p d\xi_n \psi_B^{J_B M_B *}(\vec{r}_{nA}, \xi_n, \xi_A) \Sigma_p^{s_p m_p *} V_{np}(r_{np}, \xi_p, \xi_n) \times \psi_A^{J_A M_A}(\xi_A) \Sigma_d^{s_d m_d}(\xi_p, \xi_n) \psi_d(\vec{r}_{np})$$

Eq. B.16

The integration is performed by first substituting Eq. B.15 into Eq. B.14, and then Eq. B.14 into Eq. B.16. Due to the orthogonality of the internal wave functions of nucleus A, only the terms with $J'_A = J_A$ and $M'_A = M_A$ in Eq. B.14 will contribute to the integral. Again, ξ_p and ξ_n involve only the proton and neutron spins, respectively, so the "integration" over these variables is just a sum over spins. The result is

$$Q(\vec{r}_{np}) = \sum_{\ell s_n j} i^{-\ell} \alpha_{\ell j} Y_\ell^{m *}(\theta_{nA}, \phi_{nA}) \mathcal{U}_{\ell j}^*(r_{nA}) D(\vec{r}_{np}) \times (s_p s_n m_p m_n | s_d m_d)(\ell s_n m m_n | j \mu)(J_A j M_A \mu | J_B M_B)$$

Eq. B.17

where $\mu = M_B - M_A = m_n + m$ and

$$D(\vec{r}_{np}) = V_{np}(r_{np}) \psi_d(\vec{r}_{np})$$

Eq. B.18

From the symmetry relations for the Clebsch-Gordan coefficients we have

$$(s_p s_n m_p m_n | s_d m_d) = (-)^{s_p - m_p} \sqrt{\frac{2s_d+1}{2s_n+1}} (s_d s_p m_d, -m_p | s_n m_n)$$

B.19

Then B.17 becomes

$$Q(\vec{r}_{np}) = \sum_{l s_n j} i^{-l} \left[\alpha_{lj} \sqrt{\frac{2s_d+1}{2s_n+1}} Y_l^{m*}(\theta_{nA}, \phi_{nA}) \mathcal{U}_{lj}^*(r_{nA}) D(\vec{r}_{np}) \right]$$
$$\times (-)^{s_p - m_p} (J_A j\, M_A, M_B - M_A | J_B M_B)$$
$$\times (s_d s_p m_d, -m_p | s_n m_n)(l s_n m_B m_p - m_d | j, M_B - M_A)$$

Eq. B.20

Now, a direct comparison of this with Eq. B.4 shows that the quantity in brackets in Eq. B.20 is just $J^{-1} G_{l s_n j m}(\vec{r}_d, \vec{r}_p)$, or

$$G_{l s_n j m}(\vec{r}_d, \vec{r}_p) = J \alpha_{lj} \sqrt{\frac{2s_d+1}{2s_n+1}} Y_l^{m*}(\theta_{nA}, \phi_{nA}) \mathcal{U}_{lj}^*(r_{nA}) D(\vec{r}_{np})$$

Eq. B.21

In the zero range approximation, $D(\vec{r}_{np})$ is proportional to a delta function:

$$D(\vec{r}_{np}) = D_0 \delta(\vec{r}_{np}) = D_0 J^{-1} \delta\left(\vec{r}_p - \frac{A}{B} \vec{r}_d\right)$$

Eq. B.22

Using Eq. B.6 in Eq. B.5 and Eq. B.22 in Eq. B.21 indentifies the spectroscopic coefficient as

$$A_{l s_n j} = \sqrt{\frac{2s_d+1}{2s_n+1}} \alpha_{lj} D_0$$

Eq. B.23

so that Eq. B.12 becomes (s_n=1/2 only)

$$\frac{d\sigma(\theta)}{d\Omega}_{dp} = \frac{2(2J_B+1)}{(2J_A+1)(2s_n+1)} \sum_{\ell,j} n_{\ell j} [\alpha_{\ell j}]^2 D_0^2 \sigma_{\ell j}(\theta)_{dp}$$

Eq. B.24

D_0 is related to the asymptotic ($r_{pn} \to \infty$) normalization of the deuteron wave function and can be obtained from the effective range analysis of n - p scattering. For the (d,p) reaction, then, $D_0^2 \approx 1.5 \times 10^4$ MeV^2 fm^3 (Sa64).

The number of nucleons in an orbit, $n_{\ell j}$, has been included in Eq. B.24. This factor arises when the nucleon wave functions are anti-symmetrized. The spectroscopic factor is then given by

$$S_{\ell j} = n_{\ell j} [\alpha_{\ell j}]^2$$

Eq. B.25

So that Eq. B.24 becomes

$$\left(\frac{d\sigma}{d\Omega}\right)_{dp} = \frac{2(2J_B+1)}{(2J_A+1)(2s_n+1)} \sum_{\ell,j} D_0^2 S_{\ell j} \sigma_{\ell j}(\theta)_{dp}$$

Eq. B.26

Recalling Eq. B.5,

$$G_{\ell s_n j,m}(\vec{r}_d, \vec{r}_p) = A_{\ell s_n j} f_{\ell s_n j,m}(\vec{r}_d, \vec{r}_p)$$

Eq. B.27

Equations B.23 and B.21 imply that the portion of Eq. B.21 associated with the form factor is

$$f^{o}_{l s_n j m} = Y^{m*}_{l}(\theta_{nA}, \phi_{nA})\, \mathcal{U}^{*}_{lj}(r_{nA})\, \delta\left(\vec{r}_p - \frac{A}{B}\vec{r}_d\right)$$

Eq. B.28

Here, $\mathcal{U}_{lj}(r_{nA})$ is the radial wave function for a neutron bound to nucleus A in an $(n\ell_j)$ orbit, and is referred to as the neutron "form factor". This is determined in an actual calculation by specifying the radius and shape of the neutron well and the neutron binding energy.

The essentials of the DWBA calculation for stripping and pick-up reactions in the zero range approximation have now been outlined. The method by which this theory is compared to experiment (Chapter 6) is outlined in Chapter 3.

References

Aj66 F. Ajzenberg-Selove and J. L. Wiza, Phys. Rev. 143, 853 (1966).

Au62 E. H. Auerbach, BNL Report No. 6562 (1962).

Ba64 B. M. Bardin and M. E. Rickey, Rev. Sci. Instr. 35, 902 (1964).

Ba66 J. Bar-Touv and I. Kelson, Phys. Rev. 142, 599 (1966).

Ba67 J. Bar-Touv and C. A. Levinson, Phys. Rev. 153, 1099 (1967).

Bo52 A. Bohr, K. Danske Vidensk. Selsk. Mat.-Fys. Medd. 26, No.14 (1952).

Bo53 A. Bohr and B. R. Mottelson, K. Danske Vidensk. Selsk. Mat.-Fys. Medd. 27, No.16 (1953).

Bo65 R. Bock, H. H. Duhm, and R. Stock, Phys. Lett. 18, 61 (1965).

Bl66 H. G. Blosser and A. I. Galonsky, The Michigan State University 55 MeV Cyclotron: Progress and Status, February, 1966 (Preprint).

Br62 D. W. Braben, L. L. Green, and J. C. Willmott, Nucl. Phys. 32, 584 (1962).

Br64 G. E. Brown, Unified Theory of Nuclear Models, North Holland Pub. Co., Inc., 1964

Bu51 S. T. Butler, Proc. Roy. Soc., A208, 559 (1951).

Ca64 P. E. Cavanagh, C. F. Coleman, G. A. Gard, B. W. Ridley, and J. F. Turner, Nucl. Phys. 50, 49 (1964).

Ch66 B. E. Chi, Nucl. Phys. 83, 97 (1966).

Cl65 D. Cline, W. Parker Alford, and L. M. Blau, Nucl. Phys. 73, 33 (1965).

Co65 S. Cohen and D. Kurath, Nucl. Phys. 73, 1 (1965).

Co66 A. A. Cowley, G. Heymann, and R. L. Keizer, Nucl. Phys. 86, 363 (1966).

Cr66 G. M. Crawley and G. T. Garvey (to be published).

Da58 A. S. Davydov and G. F. Filippov, Nucl. Phys. 8, 237 (1958).

Da66 K.T.R. Davies, S. J. Krieger, and M. Baranger, Nucl. Phys. 84, 545 (1966).

de Sh63 A. de-Shalit and I. Talmi, Nuclear Shell Theory, Academic Press, Inc., 1963.

Du66 J. Dubois and L. G. Earwaker, Bull. Am. Phys. Soc. 11, 908 (1966).

Du67 J. Dubois and L. G. Earwaker (to be published in Phys. Rev.).

En62 P. M. Endt and C. Van der Leun, Nucl. Phys. 34, 1 (1962).

Fr60 J. B. French and M. H. Macfarlane Revs. Mod. Phys. 32, 567 (1960).

Ga64 C. J. Gallagher, Selected Topics in Nuclear Spectroscopy (B. J. Verhaar, Editor). North-Holland Pub. Co. Inc., 1964.

Gl65 (a) C. M. Glashausser, Doctoral Thesis, Princeton University (1965).

Gl65 (b) C. Glashausser, M. Kondo, M. E. Rickey, and E. Rost, Phys. Lett. 14, 113 (1965).

Go64 F. S. Goulding, D. A. Landis, J. Cerny, and R. H. Pehl, Nucl. Instr. Meth. 31, 1 (1964).

Go65 M. M. Gordon, Lecture notes (1965).

Go67 H. E. Gove, et. al., Bull. Am. Phys. Soc. 12, 665 (1967); H. E. Gove, private communication.

Gr66 C. R. Gruhn and E. Kashy, Bull. Am. Phys. Soc. 11, 471 (1966).

Ha64 O. Hansen, E. Koltay, N. Lund, and B. S. Madsen, Nucl. Phys. 51, 307 (1964).

Ha67 H. J. Hay and D. C. Kean, Nucl. Phys. A98, 330 (1967).

He64 K. T. Hecht, Selected Topics in Nuclear Spectroscopy (B. J. Verhaar, Editor). North-Holland

Hi67 J. C. Hiebert, E. Newman, and R. H. Bassel, Phys. Rev. 154, 898 (1967).

Ja66 Gerhard Jacob and Th. A. J. Maris, Revs. Mod. Phys. 38, 121 (1966).

Jo66 J. M. Joyce, R. W. Zurmuhle, and C. M. Fou, Bull. Am. Phys. Soc. 11, 908 (1966).

Ko67 R. L. Kozub and E. Kashy, Bull. Am. Phys. Soc. 12, 664 (1967).

Ku56 D. Kurath, Phys. Rev. 101, 216 (1956).

La61 T. Lauritsen and F. Ajzenberg-Selove, Energy Levels of Light Nuclei, NRC, 1961.

La65 H. Lancman, A. Jasinski, J. Kownacki, and J. Ludziejewski, Nucl. Phys. 69, 384 (1965).

Le64 L. L. Lee, Jr. and J. P. Schiffer, Phys. Rev. Lett. 12, 108 (1964).

Ma55 M. G. Mayer and J. H. D. Jensen, Elementary Theory of Nuclear Shell Structure. John Wiley & Sons, Inc., 1955.

Mu67 R. Muthukrishnan, Nucl. Phys. A93, 417 (1967).

Ne60 T. D. Newton, Can. J. Phys. 38, 700 (1960).

Ne63 J. W. Nelson, E. B. Carter, G. E. Mitchell, and R. H. Davis, Phys. Rev. 129, 1723 (1963).

Ni55 S. G. Nilsson, K. Danske Videnske. Selsk. Mat.-Fys. Medd. 29, No. 16 (1955).

Pe63 C. M. Perey and F. G. Perey, Phys. Rev. 132, 755 (1963).

Pe66 C. M. Perey and F. G. Perey, ORNL-TM-1529 (1966).

Pi65 W. T. Pinkston and G. R. Satchler, Nucl. Phys. 72, 641 (1965).

Pr62 M. A. Preston, Physics of the Nucleus. Addison-Wesley Pub. Co., Inc., 1962.

Ri65 M. Riou, Revs. Mod. Phys. 37, 375 (1965).

Sa64 G. R. Satchler, Nucl. Phys. 55, 1 (1964).

Sh64 R. Sherr, E. Rost, and M. E. Rickey, Phys. Rev. Lett. 12, 420 (1964).

Sh65 R. Sherr, B. Bayman, E. Rost, M. E. Rickey, and C. Hoot, Phys. Rev. 139, B1272 (1965).

Si59 E. A. Silverstein, Nucl. Instr. Meth. 4, 53 (1959).

Sn67 J. L. Snelgrove and E. Kashy, Bull. Am. Phys. Soc. 12, 681 (1967).

St54 K. G. Standing, Phys. Rev. 94, 731 (1954).

St65 P. H. Stelson and Lee Grodzins, Nucl. Data (Sec. A) 1, 21 (1965).

To61 W. Tobocman, Theory of Direct Nuclear Reactions, Oxford University Press, 1961.

We65 J. J. Wesolowski, J. D. Anderson, L. F. Hansen, C. Wong, and J. W. McClure, Nucl. Phys. 71, 586 (1965).

Wh66 C. A. Whitten, Jr., E. Kashy, and J. P. Schiffer, Nucl. Phys. 86, 307 (1966).

Wi67 B. H. Wildenthal and E. Newman (preprint).

Wi67 (a) H. Wildenthal, private communication.